Design and Applications of Gold Nanoparticle/Hydrogel Composites with Stimuli-Responsive Polymers

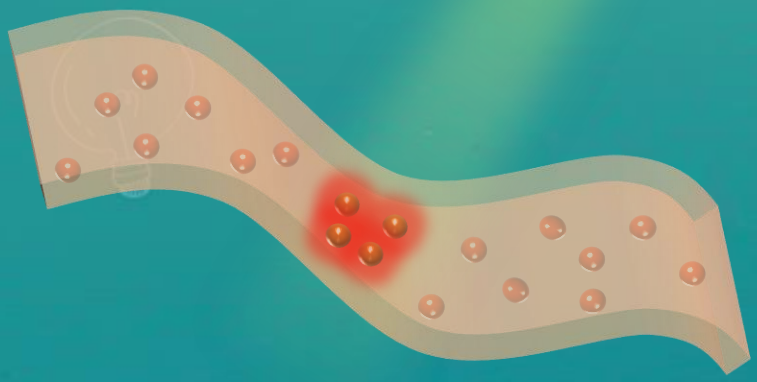

Jinmeng Hao

DESIGN AND APPLICATIONS OF GOLD NANOPARTICLE/HYDROGEL COMPOSITES WITH STIMULI-RESPONSIVE POLYMERS

Jinmeng Hao

Graduation Committee:

Chairman:	Prof. dr. J. L. Herek	University of Twente
Promotor:	Prof. dr. G. J. Vancso	University of Twente
Assistant-promotor:	Dr. M. A. Hempenius	University of Twente
Committee Members:	Prof. dr. J. J. L. M. Cornelissen	University of Twente
	Prof. dr. ir. E. van der Heide	University of Twente
	Prof. dr. X. Sui	Donghua University
	Prof. dr. I. Dekany	University of Szeged
	Prof. dr. W. Knoll	Austrian Institute of Technology

The research described in this Thesis was carried out in the groups of Materials Science and Technology of Polymers and Sustainable Polymer Chemistry, MESA+ Institute for Nanotechnology, Faculty of Science and Technology, University of Twente, the Netherlands.

This research was financially supported by the MESA+ Institute for Nanotechnology, University of Twente, and China Scholarship Council.

Cover design: Jinmeng Hao
Printed by: Ipskamp Printing
Lay-out: Jinmeng Hao
ISBN: 978-90-365-5346-9
DOI: 10.3990/1.9789036553469

DESIGN AND APPLICATIONS OF GOLD NANOPARTICLE/HYDROGEL COMPOSITES WITH STIMULI-RESPONSIVE POLYMERS

DISSERTATION

to obtain
the degree of doctor at the Universiteit Twente,
on the authority of the rector magnificus,
prof. dr. ir. A. Veldkamp,
on account of the decision of the Doctorate Board
to be publicly defended
on Thursday 17 March 2022 at 12.45 hours

by

Jinmeng Hao

born on the 15th of December, 1991
in Jilin, China

This dissertation has been approved by:

Promotor:
Prof. dr. ir. G.J. Vancso

Assistant-promotor:
Dr. M.A. Hempenius

Contents

Chapter 1

General Introduction

1.1 Introduction

Nanocomposite hydrogels were developed by incorporating different types of nanoparticles or nanostructures into hydrogel networks. The innovative combination of these two entirely different types of materials leads to advanced materials with synergistic property enhancement such as structural diversity, decreased aggregation of the nanoparticles and improved mechanical strength and stimuli response.[1–3]

Metal nanoparticles (NPs) have specific electronic structures with unique physical and chemical properties different from those in the bulk state or of atoms, based on the quantum size effect. AuNPs, as an extraordinary member of metal NP groups[4] have attracted intense scientific and technological interest due to the special optical, electronic, and thermal properties;[5] the facile synthesis and surface bioconjugation;[6–9] and exciting applications in catalysis,[10] biology,[5] and optics.[11] Specifically, AuNPs as typical plasmonic NPs can absorb light at their localized surface plasmon resonance (LSPR) and convert light into thermal energy at high efficiency.

Stimuli-responsive hydrogels, or “smart”, “intelligent” hydrogels, exhibit rapid and significant physical and chemical changes in response to variations in environmental factors such as temperature, light, pH, ionic strength, electric or magnetic field. Among all the smart hydrogels, thermo-responsive poly(*N*-isopropylacrylamide) (PNIPAM) hydrogels are one of the most extensively investigated stimuli-responsive hydrogels to date, due to their unique volume phase transition from a hydrated, expanded state to a collapsed state at its lower critical solution temperature (LCST ≈ 32 ℃) in water.[12–15]

Poly(ferrocenylsilane)s (PFS)s are organometallic polymers with a backbone consisting of alternating ferrocene and organosilane units.[16] The presence of the redox-active ferrocene centers provides PFSs with redox-responsive properties while the silane groups offer opportunities for future functionalization. PFS-based redox-responsive hydrogels have been reported as foundry for metal particles synthesis.[17–19]

1.2 Concept of this Thesis

In this Thesis, a dual-responsive hydrogel based on redox-responsive PFS and temperature-responsive PNIPAM was prepared. Taking advantage of its inherent redox-responsive properties, the hydrogels were employed as a reducing environment for the in-situ fabrication of AuNPs. Using the plasmonic photothermal effect of the formed AuNPs, AuNP-temperature responsive hydrogel composites can be remotely controlled by this efficient heat source activated by light irradiation. Based on the AuNP-stimuli responsive hydrogel synergies, we aimed at designing anisotropic structures to realize complex deformations and surface morphology changes controlled by both temperature and light and discovering the mechanism of deformation and the reaction stoichiometry of AuNP formation. The following topics will be presented and discussed in detail in this Thesis.

In **Chapter 2**, the background related to the major topics studied in this Thesis on AuNPs, stimuli-responsive hydrogels, nanocomposite hydrogels and anisotropic hydrogels are briefly reviewed from the perspective of structure design and applications.

In **Chapter 3**, a bilayer hydrogel with switchable surface morphologies is discussed featuring a compliant poly(acrylamide) bottom layer and a poly(*N*-isopropylacrylamide) top layer that contains in-situ fabricated AuNPs. Taking advantage of the plasmonic heating properties of the AuNPs, the appearance of wrinkles on the top layer can be induced by exposure to water and the disappearance can be switched by light irradiation or thermal heating.

In **Chapter 4**, to understand how the stress state impacts the development of patterns in the bilayer hydrogels described in **Chapter** 3, a series of bilayer hydrogels with different stress states are presented that exhibit elaborate patterns. By swelling the bottom layers in water for different periods of time, a dynamic evolution of surface patterns and patterns with complex features can be achieved through a decrease of the compressive strain to different degrees, which induced the decompression of the patterns to different extents.

In Chapter 5, an anisotropic PNIPAM/PVA hydrogel with PVA-reduced and -stabilized gold nanoparticles is discussed using a mechanical strain induced method. The synthesized AuNP/hydrogel nanocomposites showed anisotropic actuating behavior, triggered by the stimuli of temperature and light.

In **Chapter 6**, investigations of the stoichiometry reaction process of the PFS hydrogels in AuNP formation are presented. These materials are introduced in **Chapter 3** and **4**. Supersingly, about ten times more than the stoichiometric amount of AuNPs was formed in the reaction system with respect to employed ferrocene repeat units and the possible reasons for this are discussed.

References

[1] Chen, T.; Hou, K.; Ren, Q.; Chen, G.; Wei, P.; Zhu, M. Nanoparticle–Polymer Synergies in Nanocomposite Hydrogels: From Design to Application. *Macromol. Rapid Commun.* **2018**, *39*, 1–26.

[2] Thoniyot, P.; Tan, M. J.; Karim, A. A.; Young, D. J.; Loh, X. J. Nanoparticle–Hydrogel Composites: Concept, Design, and Applications of These Promising, Multi-Functional Materials. *Adv. Sci.* **2015**, *2*, 1–13.

[3] Zhao, X.; Ding, X.; Deng, Z.; Zheng, Z.; Peng, Y.; Tian, C.; Long, X. A Kind of Smart Gold Nanoparticle-Hydrogel Composite with Tunable Thermo-Switchable Electrical Properties. *New J. Chem.* **2006**, *30*, 915–920.

[4] Häkkinen, H. The Gold-Sulfur Interface at the Nanoscale. *Nat. Chem.* **2012**, *4*, 443–455.

[5] Daniel, M. C. M.; Astruc, D. Gold Nanoparticles: Assembly, Supramolecular Chemistry, Quantum-Size Related Properties and Applications toward Biology, Catalysis and Nanotechnology. *Chem. Rev.* **2004**, *104*, 293–346.

[6] Brust, M.; Walker, M.; Bethell, D.; Schiffrin, D. J.; Whyman, R. Synthesis of Thiol-Derivatised Gold Nanoparticles in a Two-Phase Liquid–Liquid System. *Chem. Commun.* **2000**, 7, 801–802.

[7] Boal, A. K.; Ilhan, F.; Derouchey, J. E.; Thurn-Albrecht, T.; Russell, T. P.; Rotello, V. M. Self-Assembly of Nanoparticles into Structured Spherical and Network Aggregates. *Nature* **2000**, *404*, 746–748.

[8] Li, D.; Zhang, Y.; Jiang, J.; Li, J. Electroactive Gold Nanoparticles Protected by 4-Ferrocene Thiophenol Monolayer. *J. Colloid Interface Sci.* **2003**, *264*, 109–113.

[9] Yeh, Y.-C.; Creran, B.; Rotello, V. M. Gold Nanoparticles: Preparation, Properties, and Applications in Bionanotechnology. *Nanoscale* **2012**, *4*, 1871–1880.

[10] Ciganda, R.; Gu, H.; Hernandez, R.; Escobar, A.; Martínez, A.; Yates, L.; Moya, S.; Ruiz, J.; Astruc, D. Electrostatic Assembly of Functional and Macromolecular Ferricinium Chloride-Stabilized Gold Nanoparticles. *Inorg. Chem.* **2017**, *56*, 2784–2791.

[11] Vaklev, N. L.; Vasileva, P.; Dushkin, C. Synthesis of Gold Nanoparticles via Hydrogen Peroxide Reduction Enhanced by Sonication. *Nanosci. Nanotechnol.* **2007**, *7*, 70–73.

[12] Hauser, A. W.; Evans, A. A.; Na, J. H.; Hayward, R. C. Photothermally Reprogrammable Buckling of Nanocomposite Gel Sheets. *Angew. Chemie - Int. Ed.* **2015**, *54*, 5434–5437.

[13] Zhu, C. H.; Lu, Y.; Peng, J.; Chen, J. F.; Yu, S. H. Photothermally Sensitive Poly(N-Isopropylacrylamide)/Graphene Oxide Nanocomposite Hydrogels as Remote Light-Controlled Liquid Microvalves. *Adv. Funct. Mater.* **2012**, *22*, 4017–4022.

[14] Shi, K.; Liu, Z.; Wei, Y. Y.; Wang, W.; Ju, X. J.; Xie, R.; Chu, L. Y. Near-Infrared Light-Responsive Poly(N-Isopropylacrylamide)/Graphene Oxide Nanocomposite Hydrogels with Ultrahigh Tensibility. *ACS Appl. Mater. Interfaces* **2015**, *7*, 27289–27298.

[15] Wei, W.; Hu, X.; Qi, X.; Yu, H.; Liu, Y.; Li, J.; Zhang, J.; Dong, W. A Novel Thermo-Responsive Hydrogel Based on Salecan and Poly(N-Isopropylacrylamide): Synthesis and Characterization. *Colloids Surfaces B: Biointerfaces* **2015**, *125*, 1–11.

[16] Hailes, R. L. N.; Oliver, A. M.; Gwyther, J.; Whittell, G. R.; Manners, I. Polyferrocenylsilanes: Synthesis, Properties, and Applications. *Chem. Soc. Rev.* **2016**, *45*, 5358–5407.

[17] Song, J.; Tan, Y. N.; Jańczewski, D.; Hempenius, M. A.; Xu, J. W.; Tan, H. R.; Vancso, G. J. Poly(Ferrocenylsilane) Electrolytes as a Gold Nanoparticle Foundry: "Two-in-One" Redox Synthesis and Electrosteric Stabilization, and Sensing Applications. *Nanoscale* **2017**, *9*, 19255–19262.

[18] Sui, X.; Feng, X.; Di Luca, A.; Van Blitterswijk, C. A.; Moroni, L.; Hempenius, M. A.; Vancso, G. J. Poly(N-Isopropylacrylamide)-Poly(Ferrocenylsilane) Dual-Responsive Hydrogels: Synthesis, Characterization and Antimicrobial Applications. *Polym. Chem.* **2013**, *4*, 337–342.

[19] Feng, X.; Hempenius, M. A.; Vancso, G. J. Metal Nanoparticle Foundry with Redox Responsive Hydrogels. *Macromol. Chem. Phys.* **2018**, *219*, 1–7.

Chapter 2

Gold Nanoparticles and Nanocomposite Hydrogels

In order to introduce new properties of hydrogels for multiple applications, nanocomposite hydrogels have been developed by incorporating different types of nanoparticles or nanostructures in the hydrogel network. This chapter reviews the unique features of gold nanoparticles as nanofillers including synthesis, properties and applications. Stimuli-responsive hydrogels, especially temperature-responsive, light-responsive and redox-responsive hydrogels, are introduced as matrix for nanocomposite hydrogels. Finally, an overview of the structure design principles is provided, and diverse anisotropic hydrogel structures for different types of shape transformations are summarized.

2.1 Introduction

Hydrogels are three-dimensional (3D) crosslinked networks of hydrophilic polymers, which are able to swell up to several times their original volume and absorb large quantities of water or biological fluids without losing their structure. Hydrogels possess a flexibility that is similar to natural tissue due to their significant water content. Due to their flexibility, biocompatibility, fabrication versatility, composition variety, high shape moldability and high properties tunability, hydrogels as an important class of promising soft materials that have been extensively studied in academic and industrial research,[1–8] especially in the fields of biomaterials,[1,2,4,6] soft machines,[3,4,7] and artificial tissue.[1,6]

Furthermore, stimuli-responsive hydrogels undergo reversible and significant changes in structure, shape, and/or property after being exposed to external stimuli, such as chemicals, redox potential, temperature, pH, light, electric field, magnetic field, solvent composition or the combinations of multiple stimuli.[3,9–16] The development of stimuli-responsive hydrogels allows for unprecedented levels of control over material properties in response to external stimuli and contributes to the intelligence of the various applications such as soft actuating systems,[3,7,10,13,14] drug delivery systems[9] and specialized separation systems.[11]

However, typical hydrogels usually have low mechanical properties and exhibit a sluggish mechanical change in response to external stimuli. Generally, stimuli are applied externally, which may induce the formation of hydrogel skin layers that may interfere with the permeation of solvent molecules, causing a delay in shrinking or swelling of the hydrogel.[17] Reducing the size of the gel or introducing nanoparticles (NPs) in the hydrogel network have been shown to accelerate the response rate.[18,19] Moreover, NPs can also reinforce structural stability, mechanical properties of the hydrogels and endow the hydrogels with unique properties absent in the individual components. This behavior expands their functionality and further broadens the scope of their application.

Various types of NPs have been introduced into nanocomposite (NC) hydrogels by in-situ polymerization, in-situ formation of the NPs, or by physical mixing.[20] Specifically, AuNPs as typical plasmonic NPs can absorb light at their localized surface plasmon resonance (LSPR) and convert light into thermal energy with high

efficiency. Taking advantage of its plasmonic photothermal effect, AuNP-temperature responsive hydrogel composites can be remotely controlled by this efficient heat source activated by light irradiation. AuNPs synthesized in hydrogel matrices are usually fabricated in two steps. First loading an AuNP precursor solution into the hydrogel network and then reducing the AuNP precursor to AuNPs by adding reducing agents. Alternatively, profiting from the reductive properties of redox responsive hydrogels, AuNPs can be formed in-situ in a hydrogel matrix in a cost-effective, environmental-friendly one pot process avoiding additional reductants.[21]

Additionally, inspired by biological systems which employ anisotropic structures in hierarchically integrated building units, NC hydrogels with anisotropic structures such as bilayer, gradient, patterned and oriented polymer-chain structures have been developed with unique mechanical and optical properties that are comparable to those of natural biological systems and able to adapt to complex and dynamic environments.

Based on the AuNP-stimuli responsive hydrogel synergies, in this Chapter, we summarize the background related to the major topics studied in this Thesis on AuNP synthesis, stimuli responsive hydrogels, and structural design and properties of NC hydrogels. We first review approaches to synthesizing AuNPs and the properties of AuNPs. Then we identify and discuss the multitude of response modalities for responsive hydrogels that have been developed, including temperature, light, and redox. Finally, the structural design and properties of NC hydrogels are summarized.

2.2 Gold nanoparticles

Metal NPs are particles of any shape with dimensions between 1 nm and 100 nm, according to a definition given by IUPAC in 1997.[22] Due to the quantum size effect, metal NPs have specific electronic structures with unique physical and chemical properties different from those of the bulk state or atoms.[23–25] AuNPs, as an extraordinary member of metal NP groups[26] have attracted intense scientific and technological interest due to the special optical, electronic, and thermal properties;[27] the facile synthesis and surface bioconjugation;[28–31] and exciting applications in catalysis,[32] biology,[27] and optics.[33]

2.2.1 The synthesis of AuNPs

In 1857, Faraday reported the formation of AuNPs by reduction of an aqueous solution of chloroaurate ($AuCl_4^-$) by phosphorus in carbon disulfide in a biphasic system for the first time, after which the preparation of AuNPs with controlled sizes and shapes started getting attention.[34] Colloidal suspensions can be stabilized by two processes: the first one is by introducing steric stabilization through grafting long alkyl chains to the AuNP surface, and the second is by introducing electrostatic repulsions with charged ligands. During synthesis processes, steric stabilization hinders the free movement of AuNPs. A protective layer forms by assimilation effects at the outer surface of NPs which stabilizes the AuNPs. Charged ligands can also be attached to the AuNP surface, forming a charged layer. As a result, an equal number of oppositely charged ions will border AuNPs forming an electro-neutral double layer. The electric double layer stabilizes particles by offering repulsive and attractive forces between the NPs which can be regulated by changing pH, concentration, temperature etc.[35]

The AuNPs were generally formed from the reduction of gold(III) salt ($AuCl_4^-$) with a reducing agent in the presence of a stabilizing agent. Many AuNP stabilizers are reductants by nature, therefore an additional reductant is often not necessary. The reductants that can be used are numerous such as borohydrides, aminoboranes, hydrazine, formaldehyde, hydroxylamine, oxalic acid, ascorbic acid, polyols, sugars, hydrogen peroxide, sulfites, dihydrogen, acetylene, and monoelectronic reducing agents including electron-rich transition-metal sandwich complexes;[36–39] The stabilizing agent can be trisodium citrate dihydrate, sulfur ligands (in particular thiolates), phosphorus ligands, nitrogen-based ligands (including heterocycles), oxygen-based ligands, dendrimers, polymers and surfactants.

The synthesis of AuNPs with a diameter around 20 nm was introduced by Turkevitch in 1951, using citrate reduction of $HAuCl_4$ in boiled solution.[40] With this method, citrate works both as stabilizing and reducing agent and the AuNPs prepared are loosely capped with the citrate ligand and are not stable in air. Citrate can be used for $HAuCl_4$ reduction only at high temperatures due to its weak reducibility. Natan's group further improved the method by using $NaBH_4$ as a reducing agent[41] and citrate as a stabilizing agent only. The AuNPs were obtained at room temperature with diameters around 6 nm. $NaBH_4$ is a much stronger reductant than citrate which leads

to a higher reaction rate in AuNP synthesis according to the Marcus theory.[37] As a consequence, using $NaBH_4$ as reductant leads to smaller AuNPs than using citrate.

The most convenient method for fabricating stable AuNPs was reported in 1994 by the Schiffrin group.[42] The Brust-Schiffrin method is inspired by Faraday's two-phase system (toluene/water) and $NaBH_4$ is used as a reducing agent with thiol ligands as stabilizer. $AuCl_4^-$ can be transferred to the toluene phase using tetraoctylammonium bromide as a phase-transfer reagent and reduced by $NaBH_4$ in the presence of dodecanethiol. The synthesized AuNPs are thermally stable and air-stable and can be repeatedly isolated and dispersed in common organic solvents without irreversible aggregation or decomposition. The AuNP diameters are well controlled between 1.5 and 5.2 nm. Based on the Brust-Schiffrin method, Brust et al. developed the Brust-Schiffrin procedure with the synthesis of *p*-mercaptophenol-stabilized AuNPs in a one phase system.[43] Various other stable AuNPs with different alkylthiol or arylthiol ligands were reported since then.[44] The size of the AuNPs can be controlled by adjusting the ratio between $AuCl_4^-$ and the stabilizing agent.[45]

Ferrocene and its derivatives, as electron-rich transition-metal sandwich complexes, have been used as reducing agents and/or stabilizers to synthesize AuNPs with controlled sizes. In the reported literature, ferrocene and its derivatives were used as single-electron transfer reductants. Didier Astruc's group reported using a large variety of ferrocenes including dendritic and polymeric ferrocenes,[32,46–51] and ferrocenes containing electron-withdrawing or electron-releasing substituents as reductants and/or stabilizers for the formation of AuNPs in one phase or biphasic systems as shown in Figure 2.1 (a-c). Poly(ferrocenylsilane)s (PFSs) were also reported for the synthesis of stable and redox-responsive AuNPs by Julius Vancso's group (Figure 2.1d).[13,52–55] Song et al.[56] described the spontaneous formation of AuNPs using positively or negatively charged PFS (PFS^+/PFS^-) electrolytes as reducing agents and stabilizing polymer. A polyelectrolyte works as a polymeric surfactant which offers combined effects of electrostatic and steric stabilization thus preventing agglomeration and generating a dual stabilization system.

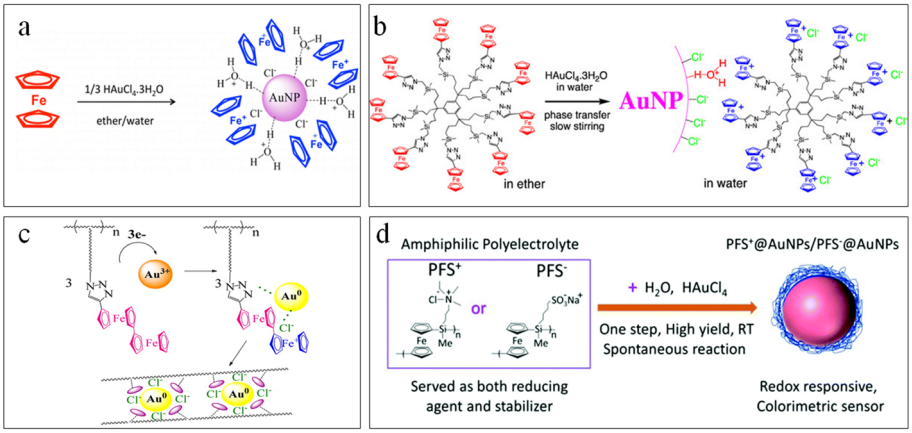

Figure 2.1 Preparation of AuNPs using **a**) ferrocene,[49] **b**) dendritic ferrocene,[32] **c**, **d**) polymeric ferrocenes[51,56] as both reducing agents and stabilizers.

2.2.2 Properties of AuNPs

Considerable research has been focused on AuNPs for their fascinating LSPR properties. LSP is the collective oscillations of free electrons in metal NPs (6s electrons of the conduction band for AuNPs).[57] LSPR occurs through resonant excitation of an AuNP conduction band by the electromagnetic field of the incident light.[57] At this resonant frequency, the incident light is absorbed by AuNPs and the strong absorption of the incident light can be measured with a UV–Vis spectrometer. Some of these light photons will be released with the same frequency in all directions and this process is known as scattering.[58] AuNPs can absorb and scatter light with high efficiency.[59,60]

Spherical AuNPs dispersed in aqueous solution show different colors from red to purple as the diameter increases. For monodispersed small spherical AuNP solutions, the SPR causes a strong scattering and absorption in the blue-green region of the spectrum with red light reflected, showing a rich ruby color. With AuNP particle size increasing, the absorption shifts to longer, more red wavelengths. When the red light is absorbed, blue light is then reflected yielding AuNP solutions with a blue or purple color. As particle size continues to increase toward the bulk limit, LSPR absorption shifts to the infrared spectrum with visible light reflected, leading to a translucent color. In addition, aggregation of AuNPs of will cause a significant red-shifting of

the LSPR frequency and broadening of the surface plasmon band which results in a color transition from red to blue due to interparticle plasmon coupling. The intensity and position of the absorption peak of the LSPR band depend on the electron charge density (dielectric constant) on the particle surface. Therefore, the LSPR properties can be tuned by controlling particle size, shape, capping agent, temperature and solvent as theoretically described by the Mie theory.[35,61,62] It should be noted that the SPR band is absent in both small NPs (d < 2 nm) and the bulk material.

2.2.3 Applications of AuNPs

Photothermal effects It was already mentioned that AuNPs absorb light. The absorbed photons are mostly converted to phonons, leading to a temperature increase of the surrounding lattice. Heat dissipation from the hot particles will also heat up their surroundings. The light to heat conversion is extremely efficient in AuNPs due to the following features[57,63]: 1) high absorption in the visible and NIR regions; 2) excellent photostability; 3) low luminescence yield; 4) rapid relaxation of the LSPR. Particularly, compared with the strongest light absorbing organic chromophores, the absorption intensity in AuNPs is several orders of magnitude larger.[63–65] Besides, the LSPR can be tuned to specific regions, such as 700–950 nm and 1000–1350 nm where body tissues are more optically transparent, which makes it possible to heat AuNPs in vitro.[60] Taking advantage of its photothermal effects, AuNPs have been used for photothermal therapy,[63] light-triggered drug release,[66] photothermal contrast imaging,[64] photothermal phase transformations etc.[57]

Sensing The aggregation of AuNPs of appropriate size (d > 3.5 nm) induces interparticle surface plasmon coupling, resulting in a visible color change from red to blue at nanomolar concentrations.[58] The color change during AuNP aggregation (or redispersion of an aggregate) provides a practical platform for absorption-based colorimetric sensing of any target analyte that directly or indirectly triggers the AuNP aggregation or redispersion.[58]

AuNP-based colorimetric sensors have been used for the detection of metal ions, anions, small organic molecules, oligonucleotides, proteins etc..[58,67–70] Besides colorimetric sensors, fluorescence-based sensors,[71] electrical and electrochemical sensors[72] and surface enhanced Raman scattering based sensors[73] etc. were also developed due to the distinct physical and chemical properties of AuNPs.

Imaging AuNPs can be used to improve resolution and sensitivity in biological imaging in vitro and in vivo because of the unique plasmonic properties. AuNPs are powerful contrast agents in light scattering imaging, due to their much stronger scattering signal than the scattering background from cells and tissues, together with their excellent photostability and biocompatibility.[74] It was introduced by Yguerabide etc. that AuNPs are used as ultrasensitive labels for analyte detection in immunoassays, cells, and tissues with an angled dark-field illuminator coupled with a conventional microscope.[75] Later, true-color Au-NP-enhanced cancer cell imaging was achieved with commercial dark-field microscopy.[73]

Dark-field microscopy is one of the most commonly used techniques in the resonance light scattering imaging of AuNPs due to its simplicity, low cost, and availability. Besides, AuNPs have also been employed for cell imaging using other techniques, such as differential interference contrast (DIC) microscopy, optical coherence tomography (OCT),[80] and Raman spectroscopy.[64] In addition, due to the photothermal effects, AuNPs can be used for photothermal imaging.[57]

2.3 Stimuli-responsive hydrogels

An important feature of hydrogels is their environmental sensitivity, allowing them to respond to external physical (temperature, mechanical effect, electromagnetic radiation, electric or magnetic field) / chemical (solvent conditions: composition, dissolved species, pH, ionic strength) / mechanical stimuli with changes in their swelling behavior, sol-gel transition, network structure, permeability, or mechanical strength. These hydrogels are often named “smart”, “intelligent” or “stimuli-responsive” hydrogels. They were among the first biomaterials designed for clinical use in contact lenses in the early 1960s by Otto Wichterle and Drahoslav Lím.[76] They have attracted extensive attention due to their potential applications in various fields during the past two decades.[9,10,14,16,77] Different from conventional hydrogels, which exhibit swelling/deswelling properties based on the surrounding environment and water availability, stimuli-responsive hydrogels’ unique properties can be associated with environmental factors controlled by external stimuli which makes these hydrogels the very promising materials. The response of hydrogels to external stimuli is mainly determined by the nature of the stimuli-responsive co-monomers which constitute the stimuli-responsive polymer, including charge density,

pendant chains, and the degree of crosslinking. The magnitude of the response also correlates with the employed external stimuli.

Hydrogels can be classified as homopolymer, copolymer, or semi-interpenetrating networks (semi-IPN) based on the methods of preparation. Homopolymeric hydrogels are polymer networks derived from a single species of monomers and copolymeric hydrogels generally contain two or more monomeric species. Semi-IPN forms when a linear polymer penetrates into another crosslinked network with no covalent interactions between the two polymers. Mechanical properties and salt resistance of hydrogels can be improved by introducing semi-IPN structures.[78,79] Especially, semi-IPNs can be used to increase the response rates to pH or temperature changes.[80,81] Compared with full-IPNs, semi-IPNs can preserve rapid kinetic response rates to stimuli more effectively due to the absence of a restricting interpenetrating elastic network. To build a multi-responsive hydrogel system, copolymeric and semi-IPN methods can be suitable approaches. Interestingly, the incorporation of stimuli-responsive monomers, either into the backbone of the network or as pendant groups, leads to responsive properties of the hydrogels. A fast response rate is important for applications involving smart hydrogels, especially since most conventional hydrogels show rather low response rates. Stimuli-responsive hydrogels have shown great potential in various fields including biomedical, biotechnology, pharmaceutical, separation science and especially in non-invasive, remote-controlled therapies, including targeted drug delivery, regenerative medicine, tissue engineering, and implanting artificial organs.[82] Continuous research and development aimed at improving the properties of these smart hydrogels by modifying their structural components and synthesis methods have resulted in more innovative materials like supramolecular, micro-engineered, nanocomposite, anisotropic and nanofiber infused hydrogels.

Based on the types of stimuli, smart hydrogels can be mainly classified as temperature, pH, light, redox, magnetic, chemical and multi-responsive hydrogels. The responses varied from a small change in swelling ratio to a complete collapse and even an inversion of properties. Several different types of responsive hydrogels and their specific properties will be discussed below.

2.3.1 Temperature-responsive hydrogels

Temperature-responsive hydrogels have been the most investigated among all the stimuli-responsive hydrogels, because temperature can be easily controlled and applied in vivo and in vitro conditions. Based on the solution temperature behavior of the polymers, temperature-responsive hydrogels can be classified as negatively thermosensitive lower critical solution temperature (LCST) and positively thermosensitive upper critical solution temperature (UCST) hydrogels.

For the LCST hydrogels at lower temperatures, water is absorbed and the gel is swollen due to hydrogen bond formation between water molecules and the hydrophilic groups in the polymer network. However, when the temperature exceeds the LCST, water is expelled and the gel is deswelling because hydrogen bonding interactions between the hydrophilic groups and water molecules are broken which causes the polymer chains to collapse and then precipitate in the media with a phase separation.[83–85] Typical LCST hydrogels contain polymer chains that either possess moderately hydrophobic segments or comprise a mixture of hydrophilic and hydrophobic groups. The LCST of temperature-responsive hydrogels is based on the ratio of hydrophilic (e.g., amide and carboxyl) and hydrophobic (e.g., methyl, ethyl, and propyl groups) segments in the polymer chains or a single monomer. Besides, molecular weight of the polymer and hydrogel crosslink density also influence the LCST.[83] The structures of some of the temperature-responsive polymers are shown in Figure 2.2.

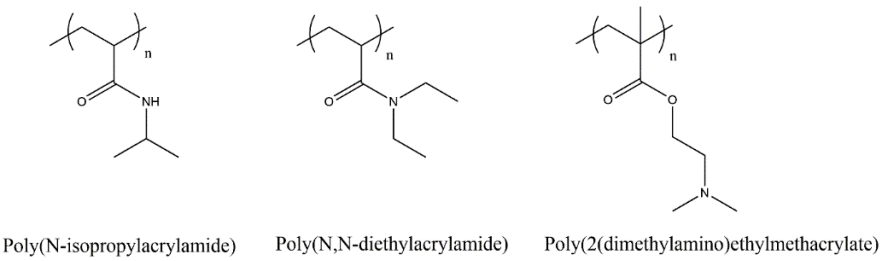

Figure 2.2 Structures of some temperature-responsive polymers.

The LCST of hydrogels can be tuned by adding a hydrophilic component to increase, or a hydrophobic component to decrease the transition temperature.[85] Among all the temperature-responsive hydrogels, poly(*N*-isopropylacrylamide)

(PNIPAM) is one of the most studied in tissue engineering investigations due to its LCST (around 32 °C) falling in the physiological regime, which makes it ideally suited for drug delivery and allows for controlled interactions with biomolecules.[83]

2.3.2 Light-responsive hydrogels

Light-responsive hydrogels change their physical and/or chemical properties when irradiated with light of a certain wavelength. Light as an environmentally friendly, noninvasive stimulus, can be applied instantly and delivered in specific light intensity and irradiation time, which allows a precise control of irradiation dosage and allows one to tune the degree of conversion in photo reactions. By light irradiation, a precise spatiotemporal control over the expression of light-responsive groups within hydrogel networks in both 2D and 3D, and temporal control by simply turning the light source on or off can be realized.[86] Besides, light-responsive hydrogels can be remotely manipulated without producing byproducts, which further makes light-responsive hydrogels advantageous over other smart hydrogels.[86–89] The light source for the light-responsive systems can be visible, near infrared (NIR) or ultraviolet (UV) light based on the wavelength of the light absorbed by photo-receptive moieties in the hydrogels. During the photo irradiation process, the light will first be captured by the photo-receptive moieties which then convert the photo energy to a chemical signal by photoreactions including isomerization (cis-trans, open-close), cleavage, and dimerization. The hydrogel will then change its properties accordingly. Light-responsive hydrogels can be achieved by incorporating photochromic moieties into hydrogels such as derivatives of *o*-nitrobenzyl compounds, triphenylmethane, *p*-hydroxylphenacyl, family of boron-dipyrromethene, azobenzene, disulfide and spiropyran etc.[90] Azobenzene (and its derivatives) is a well-known example that undergoes photoisomerization transformation in ultraviolet light (365 nm) from the *trans*-configuration to the *cis*-configuration via a π–π* transition and can relax back to the more stable *trans* state by visible light irradiation (445 nm) or heating.[9] This photo-isomerization changes both the molecular polarity and spatial structure, which has a big impact on host–guest interaction behavior. Azobenzene forms host–guest complexes with cyclodextrin and the stabilities depend on the *cis* or *trans* state of the azobenzene moiety.[91] Based on this, many light-responsive hydrogels were designed with azobenzene–CD host–guest interaction.[91,92]

Different from most of the conventional light responses which come from photo-receptive groups incorporated in the system, combining photothermal effects and LCST hydrogels is a novel approach to light-responsive systems. By incorporating photothermal agents which generate local heating through light irradiation, reversible phase transitions of temperature-responsive hydrogels can also be realized which makes the hydrogels multi stimuli-responsive. Many photo-responsive hydrogels were designed based on this method.[14,18,19,59,60,93–96] Common photothermal agents can be inorganic nanomaterials such as noble metals (e.g., Au, Ag, and Pt) or oxide NPs, carbon nanomaterials, and organic compounds including cyanines, croconaines, diketopyrrolopyrroles, porphyrins, and conjugated polymers. Commonly used temperature-responsive materials include PNIPAM and PEG analogs etc.[97] This strategy is versatile and allows one to design hydrogels responsive to biocompatible NIR light; however, damage to surrounding tissues by overheating needs to be considered in biological and biomedical applications. As remote-tunable materials, light-responsive hydrogels strongly contribute to the field of smart hydrogels.

2.3.3 Redox-responsive hydrogels

Redox-responsive hydrogels incorporating redox-active species which can undergo reversible oxidation–reduction reactions, change their physical and/or chemical properties when redox stimuli are applied chemically or electrochemically. For the design of redox-responsive hydrogels, redox-active moieties can be introduced as polymer main chain, side groups or as crosslinking agents. Compared with other stimuli investigated, a change in redox state is one of the most relevant triggers targeted in the biomedical research field. As a representative cellular redox couple, glutathione/glutathione disulfide (GSH/GSSG) works constantly to buffer the level of reactive oxygen species to keep the redox environment well regulated.[15] Besides, in the medical field, redox-responsive materials are also well known as actuators. Typical redox-active species include ferrocene (Fc), transition metal ions (e.g., iron, cobalt, copper, ruthenium, osmium), disulfide, tetrathiafulvalene etc.[98–100]

Ferrocene is the most frequently utilized molecule in redox-responsive systems. Ferrocene as a typical redox-active organometallic compound, possesses a d6 Fe(II) 18-electron neutral sandwich-like molecular structure (orange) which undergoes oxidation at a moderate potential of around +0.4 V (vs. saturated calomel electrode, SCE) or by using oxidizing agents such as H_2O_2 and Fe^{3+} to a green d5 Fe(III) 17-

electron cationic form, known as ferrocenium. With the redox state changes from Fc to Fc^+, ferrocenium containing materials become more hydrophilic, rendering a higher degree of swelling along with a color change from orange to green. For polymers bearing Fc groups in the side chains, various redox-responsive supramolecular hydrogels were developed by exploiting this hydrophilicity change behavior, which is based on host-guest interaction between reduced ferrocene and β-cyclodextrin.[15] As Fc is oxidized and becomes positively charged and therefore more hydrophilic in its oxidized state, the host-guest interaction breaks. The redox-sensing properties of ferrocene and reaction as hydrophobic guest with β-cyclodextrin is reversible. The ferrocene/ferrocenium redox system is widely used in biomedical, electrochemistry, material science and chemical science applications.

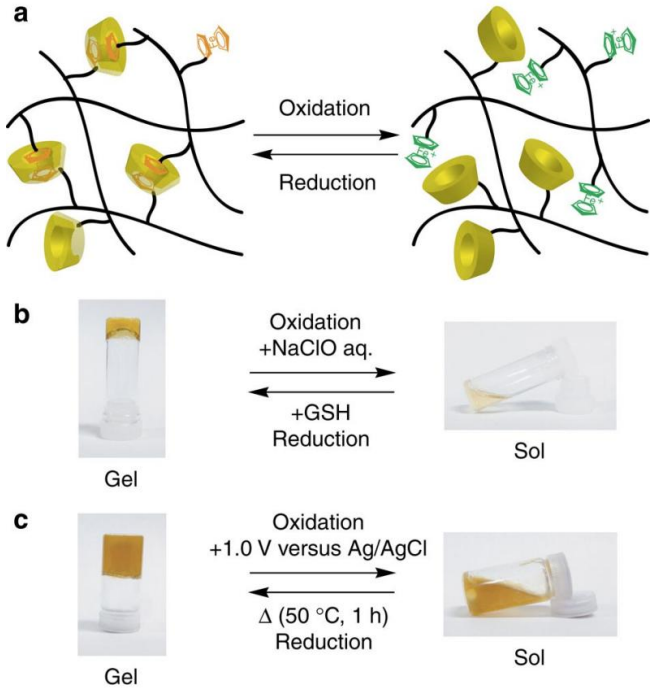

Figure 2.3 Sol–gel transition experiment using chemical reagents and electrochemical stimuli. **a**) β-cyclodextrin forms an inclusion complex with ferrocene, while upon oxidation to ferrocenium the complex is disrupted. **b**) Sol−gel transition experiment using chemical reagents. **c**) Sol−gel transition experiment using electrochemical reactions.[15]

Supramolecular hydrogels of poly(acrylic acid) (PAA) modified with β-CD as a host polymer and PAA with ferrocene pendant groups as a guest polymer show a sol–gel transition upon host–guest interaction as shown in Figure 2.3.[15] The reversible sol–gel phase transition in this system could be controlled by the presence of an oxidant or reductant. Addition of aqueous $NaClO_4$ to the hydrogel induced a phase transition to the sol state, and constant addition of GSH to the sol reformed the hydrogel again and restored its elasticity. Besides chemical oxidation and reduction, applying a redox potential to the hydrogels can also induce a reversible sol–gel phase transition in this system. The hydrogel was transformed into a sol state by electrochemical oxidation and could be turned back to the hydrogel state by electrochemical reduction.

In addition to introducing Fc groups into the polymer side chains, Fc based hydrogels can also be are obtained by the incorporation of ferrocene derivatives in the polymer main chain. A particularly interesting class of polymers featuring skeletal redox-active moieties are PFSs, which are one of the most well-developed classes of metallopolymers with a main chain consisting of alternating silane and ferrocene units.[101,102] These materials possess a high density of redox centers and can be reversibly oxidized and reduced by chemical and electrochemical means. The synthesis of PFSs with a variety of substituents at the skeletal silicon atoms can be realized by the use of the ring-opening polymerization (ROP) of strained silicon-bridged ferrocenophane precursors as was first described in 1992 (Figure 2.4).[103] PFSs can be amorphous or crystalline, soluble in water or organic solvents, depending on the features of the substituents. Redox-responsive hydrogels can be obtained by including water soluble PFS with ionic side groups, or by linking the organophilic PFS chains with water-soluble polymers such as poly(ethylene glycol) (PEG) chains. For example, two distinct types of PFS polyelectrolyte networks with either permanently positively or negatively charged side groups have been prepared (Figure 2.5).[13]

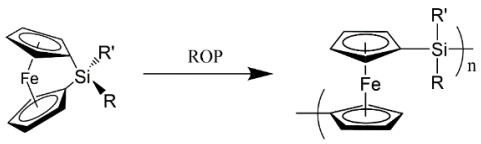

Figure 2.4 Synthesis of PFSs by ROP of strained silicon-bridged ferrocenophane.[103]

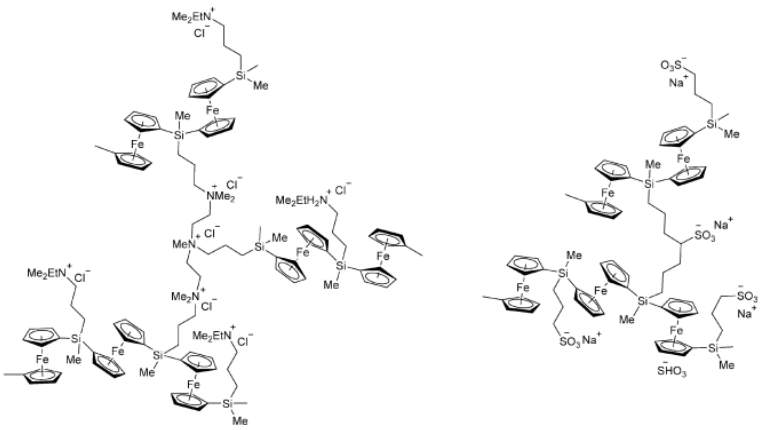

Figure 2.5 Permanently charged cationic and anionic PFS networks.[13]

Redox-responsive PFS-based poly(ionic liquids) (PILs) have been reported to form water swellable, redox-active gels.[53,104,105] Poly[ferrocenyl(3-iodopropyl)methylsilane] was reacted with 1-vinylimidazole, then the iodide counterions were exchanged for chloride to improve water solubility. This PFS PIL self-cross-linked into nanogels at low concentrations and macroscopic hydrogel networks were formed at higher concentrations. The iron centers in PFS can be chemically oxidized by H_2O_2 accompanied by a very distinct color change from amber to blue/green.[13,54]

2.4 Nanocomposite hydrogels

NC hydrogels are hydrogels that are reinforced with nanomaterials such as nano-clay,[106] fumed silica,[107] carbon-based nanostructures including carbon nanotubes,[20,89] graphene and graphene oxide,[59,108] metal and metal oxide NPs[86,89,91] such as gold, silver, iron oxide, titanium oxide (TiO_2), nanohydroxyapatite, alumina and zirconia, and polymeric NPs such as hyper-branched polyesters, cyclodextrins, peptides, and nanocellulose as shown in Figure 2.5.[109,110] By combining hydrogels and nanomaterials, unique properties absent in the individual components can be achieved. The properties of the materials will be highly enhanced and the limitations of the hydrogel scaffold, such as poor mechanical strength and lack of bioactivity,

can be overcome.[20,111] For example, modified PEG hydrogels incorporated with silica NPs were reported with remarkable improvements in tissue adhesive property, mechanical stiffness and bioactivity compared to hydrogels without NPs.[20] NC redox-responsive hydrogels also demonstrated higher sensitivity to stimuli.[112] NC gels exhibit improved stimulus-sensitivity, elasticity, strength and electrical properties compared with traditional hydrogels, which broadens their applications in drug delivery, actuator, electronics, biosensing, nanomedicine, and environmental remediation.[21,110–114]

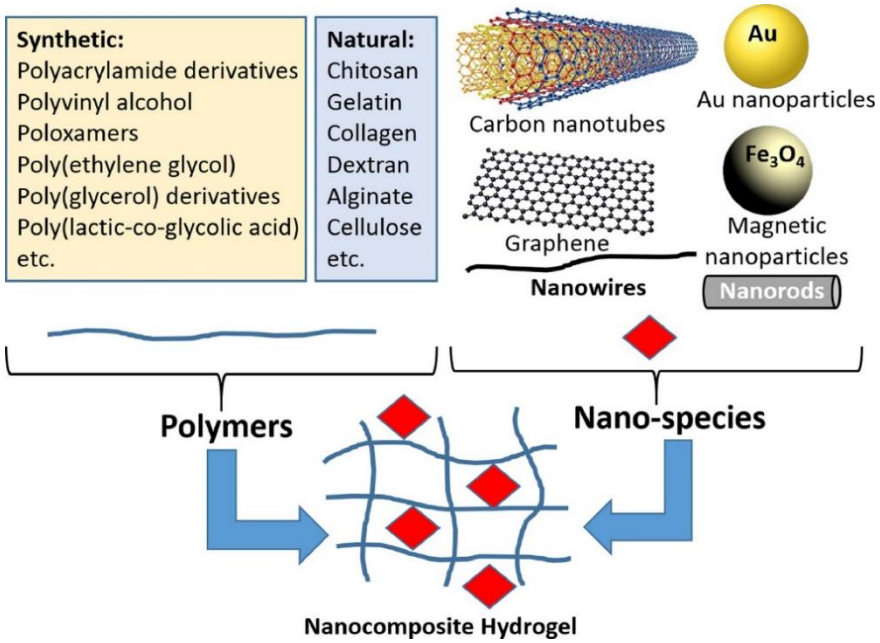

Figure 2.6 Nanocomposite hydrogels composed of various polymer matrices filled with different nano-species.[115]

Various possibilities can be used to embed NPs uniformly into a hydrogel matrix including: 1) in-situ formation of NPs in a hydrogel matrix, 2) formation of hydrogels in nanoparticle suspensions, 3) formation of hydrogels using NPs as crosslinkers, 4) physical introduction of NPs into the prepared hydrogels.

In-situ formation of NPs in a hydrogel matrix With the in-situ formation method, nanoparticle precursors (usually for metal or metal oxide NPs) undergo a reaction which forms NPs in the hydrogel matrix. The hydrogel media inhibit aggregation of

NPs during the reaction, leading to a uniform distribution of NPs. The in-situ reaction (usually a reduction process for metal ions) can be performed in two steps by first adding metal ions to crosslinkable polymer chains. After hydrogel formation, a reducing agent is added, which turns the metal ions into metal nanoparticles. In-situ formation of NPs in hydrogels may also be achieved in one step by employing photo-reducing metal ions followed by irradiation. Alternatively, one may use a redox-responsive hydrogel matrix as reducing agent.

NC hydrogels can be easily fabricated by a two-step method. Firstly, the NP precursor solution is loaded into the crosslinked hydrogel. Then, an in-situ reduction process of the metal ions is commenced by adding additional reducing agents such as sodium borohydride, hydrazine or citrate, resulting in the formation of NPs throughout the hydrogel matrix. For example, Varaprasad et al. reported a poly(acrylamide)/poly(vinyl sulfonic acid sodium salt) (PAAm-PVSA)/AgNP NC hydrogel for anti-bacterial wound dressing. The hydrogel was prepared first, followed by swelling in silver nitrate and sodium borohydride solutions, sequentially.[116]

NC hydrogels can also be prepared by in-situ formation of metal NPs in redox-responsive hydrogels. PFSs possess a high density of redox centers and can be reversibly oxidized and reduced by chemical and electrochemical means[13,117,118]. PFS hydrogels were reported to reduce metal ions to the corresponding metal NPs by Julius Vancso's group.[21,54,56] Silver, gold, platinum, palladium, rhodium, ferroferric oxide and iridium NPs were formed in-situ within a PFS hydrogel network as shown in Figure 2.7. The network structure of the cross-linked PFS chains provides a confined environment for metal salt reduction which may influence size and polydispersity of the NPs produced. This method is cost-effective and environmentally-friendly as the composite hydrogels were fabricated in a one pot process avoiding additional reductants.

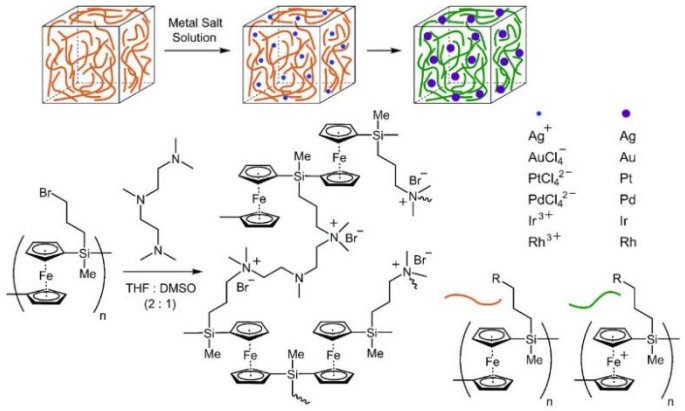

Figure 2.7 Schematic illustration of the "metal nanoparticle foundry". The ferrocene units of the PFS chains (amber color) are oxidized to ferrocenium moieties (dark green) as the added noble metal salts are reduced to noble metal NPs. Also, the one-step synthesis of the PFS hydrogel is shown.[21]

The irradiation method can be used as an alternative to the chemical reducing method. Khampieng et al. have reported the synthesis of a poly(vinyl pyrrolidone) (PVP) hydrogel incorporated with AgNPs by gamma irradiation. PVP gel precursor was first mixed with silver nitrate and then exposed to gamma irradiation. The formation of AgNPs and hydrogel network occurred simultaneously.[119] Similarly, Kumaraswamy et al. have demonstrated the synthesis of AuNP/PVA hydrogel nanocomposites using gamma irradiation.[120] Free radicals including solvated electrons, hydroxyl radicals (OH•), and hydrogen atoms (H•) form when water interacts with gamma radiation. OH• radicals in aqueous medium induced the crosslinking of PVA polymer. The Au^{3+} ions are reduced to zero-valent Au^0 by solvated electrons, corresponding to direct electron transfer ($Au^{3+} \rightarrow Au^{2+} \rightarrow Au^{+} \rightarrow Au^0$ (AuNPs)). With the irradiation method, toxic initiators and crosslinking agents are not needed[119] which makes it a simple, environmentally-friendly approach to NC hydrogels.

Formation of hydrogels in nanoparticle suspensions In this method, the hydrogel precursor is mixed with nanoparticle suspensions with the help of mechanical stirring or sonication first, then polymerized like conventional hydrogels. The NPs used here generally do not interfere with the gelation process. NC hydrogels incorporated with carbon-based NPs are often fabricated using this method.[111,121]

However, the NPs could leach out of the hydrogel matrix due to the weak interaction between particles and polymeric media.

Formation of hydrogels using NPs as crosslinkers NPs with crosslinking groups present on the nanoparticle surface can be used as physical or chemical crosslinkers for the formation of NC hydrogels. NPs cross-linkers can usually form multiple bonds within the gel networks. Yu et al. reported the synthesis of robust and smart NC PNIPAM hydrogels, prepared using multi-vinyl-modified AuNPs through a thiolate-gold coordination interaction, as large crosslinkers.[122] The NC hydrogels exhibit excellent elasticity with increased mechanical strength at high elongation, due to the efficient energy dissipation from dynamic gold crosslinks with enhanced branching. Similarly, Zhao et al. also demonstrated AuNP/PNIPAM hydrogel composites with thermo-switchable electrical properties by using vinyl functionalized AuNPs as crosslinkers.[122] By changing the concentration of AuNPs, the transition temperature of the NC hydrogels could be adjusted from 0 °C to 40 °C. Carbon, silica, laponite, polymer NPs etc. with functional crosslinking groups were also reported serving as chemical/physical crosslinkers for synthesizing hydrogels.

Physical introduction of NPs into the prepared gels Pardo-Yissar et al. explored a “breathing” mechanism to physically introduce NPs into polyacrylamide films by cyclic deswelling and swelling of the polymer networks in a poor and good solvent, acetone and aqueous suspension of NPs, respectively.[122] NPs remain inside the gels during the breathing out cycle due to the collapse and physical entanglements of the polymer chains and hydrogen bonding between the monomers and the citrate surface of the NPs. During the breathing in cycle, the shrunken hydrogel swells up while breathing in the suspended NPs into hydrogel matrix. However, NPs may leach from the hydrogel with time.

2.5 Anisotropic hydrogels

Traditional synthetic hydrogels are typically amorphous in structure with randomly oriented 3D polymer networks. The synthetic hydrogels usually do not possess any dedicated function as living bodies do because synthetic gels typically lack any sophisticated structure. In contrast, for smart functions and movements, most tissues in biological systems usually have an anisotropic morphology and structure from molecular to macroscopic levels as represented by muscle,[123] skin,[124] and

articular cartilage.[125] The anisotropy in biological systems plays an essential role in expressing their particular functions, including mass transport, surface lubrication, force generation, etc. For example, muscle tissues contain unidirectionally oriented collagen fibrils closely packed in parallel arrays which provides muscles with prominent mechanical strength and one-dimensional contraction.[126] Inspired by biological systems, introducing sophisticated anisotropic structures into synthetic hydrogels would enable applications such as soft robots, artificial muscles, valves, artificial organs and tissues.[4,127–131]

2.5.1 Hydrogels with oriented polymer-chain networks

The most common way to synthesize hydrogels with oriented polymer-chain networks is by mechanically stretching or compressing the gel network unidirectionally. With the anisotropic mechanical deformation, the isotropic hydrogel network deforms accordingly, forming an oriented network. Thus induced temporal anisotropy can be fixed with adding another physical network by in-situ polymerization.[127,128,132,133] Gong et al. reported an even more convenient method to fabricate anisotropic hydrogels with perfectly aligned multiscale hierarchical fibrous structures by first drying a diluted physical hydrogel in air to confine its length direction, then reswelling it in water.[134] This method only applies to relatively rigid polymers (such as alginate and cellulose), since a rigid chain is more susceptible to orient in response to a mechanical signal than a flexible chain. The strength and toughness of the hydrogels can be tuned by controlling the degree of alignment with stretching.

2.5.2 Hydrogels with oriented nanofillers

Similarly, oriented nanofillers in hydrogels can be achieved by anisotropic deformation-induced shear-force orientation along with the oriented polymer network chains. In general, when a shear-force is applied to aqueous nanofiller dispersions, the nanofillers orient their long axis parallel to the shear direction. Anisotropic hydrogels can then form by in-situ polymerization of the gel precursor bearing the orientated nanofillers.[135,136] Nanofillers including natural[137] or synthetic[136,138] peptide nanofibers,[139] cellulose nanofibers,[132,134,140] surfactant

bilayers,[141] and inorganic nanofillers have been reported to orient with shear-force, allowing the fabrication of anisotropic hydrogels.

Applied electric fields can orient nanofillers such that their permanent or induced dipole moment is parallel to the electric field. Gel precursors can be crosslinked in-situ in the electrically oriented nanofiller dispersions. To avoid undesired electrochemical decomposition and electrophoresis caused by electric fields, it is necessary to optimize conditions such as voltage, current frequency, and sample thickness. Nanofillers including functionalized carbon nanotubes, clay nanosheets, silver nanowires and silk nanofibers have been reported to orient in electric fields, leading to anisotropic hydrogels.[142–145]

Similarly, applied magnetic fields can orient magnetic nanofillers such as magnetite particles,[146] carbonyl iron,[147] and nickel rods[148] in the direction that their easy magnetization axis is parallel or antiparallel to the magnetic field. Besides all the methods mentioned above, nanofillers with high aspect ratio can also spontaneously align their long axes parallel to solid–liquid interfaces during concentration[149] and filtration[150] of their aqueous dispersion to afford anisotropic hydrogels.

2.5.3 Hydrogels with bilayer structures

Bilayer hydrogels consisting of two hydrogel sheets with different swelling ratios exhibit controllable deformations such as bending and buckling based on the asymmetrical swelling response of the joined sheets. Bilayer hydrogels can be fabricated by means of layer-by-layer polymerization[151] or by assembling two different hydrogels together via glue,[152] host–guest interactions,[153] and hydrogen bonding.[154]

Layer-by-layer polymerization is the most employed method for fabricating bilayer hydrogels. In the preparation process, the first hydrogel layer is formed initially and is subsequently covered with the second layer in the form of a gel precursor. The added gel precursor penetrates the first layer which leads to an interpenetrating network at the interface, connecting the two layers tightly together. Chen et al. developed a thermo-responsive bilayer hydrogel actuator with internal water self-circulation by combining a PNIPAM hydrogel possessing an LCST and poly(acrylic acid-*co*-acrylamide) (P(AAc-*co*-AAm)) hydrogel which has a UCST.[155] Water molecules could migrate between the two layers with temperature stimuli.

Bilayer hydrogels can present various types of deformation including wrinkling, creasing, folding, bending and rolling etc., depending on the thickness of the two layers, their moduli, and sample size as shown in Figure 2.8.[156]

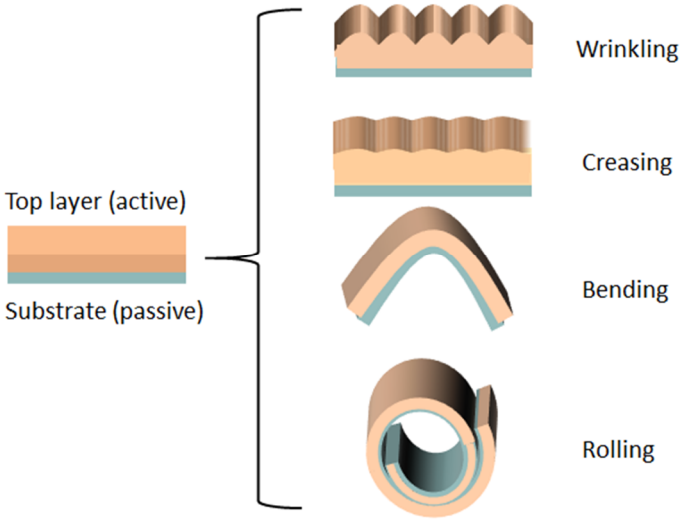

Figure 2.8 Different kinds of deformation in a bilayer film. Green is a substrate or passive layer while orange is the active layer.[156]

For bilayer hydrogels with a homogenous soft layer confined by a rigid substrate layer, a compressive stress can be induced by the constrained swelling, and the induced stress can trigger the surface instability of the soft layer, leading to the formation of creases with sharp self-contact tips as shown in Figure 2.9a.[157] Meanwhile, bilayer hydrogels with a thin rigid top layer and a compliant thick bottom layer can lose stability and form wrinkling or folding patterns by external stimuli as shown in Figure 2.9b. The swelling and in-plane compressive stress are generated within the gel. When the compressive stress reaches its critical value, different surface patterns will form at the gel surface to reduce the system energy.[158–160] With larger swelling degree, the large stress induced at the surface will cause the formation of folding patterns, ridges, local delamination and even collapsing of wrinkles into discrete folds.[161] Morphologies created by surface instability can be controlled by solvent-induced swelling/shrinking and by mechanical force.

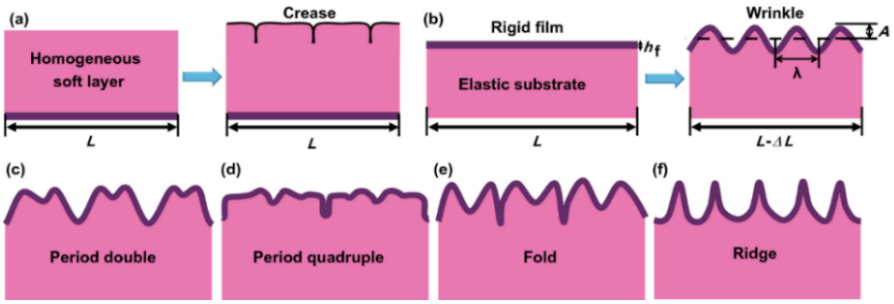

Figure 2.9 a) Schematic of crease formation on the surface of a homogeneous soft layer supported by a rigid substrate. **b**) Schematic of wrinkle formation in a typical bilayer system composed of a rigid film on an elastic substrate. h_f is the film thickness, A and λ represent the amplitude and wavelength of the wrinkle, respectively. **c**–**f**) Schematic of several typical morphological instabilities: **c**) period double, **d**) period quadruple, **e**) fold, and **f**) ridge.[162]

For wrinkling surfaces, the critical buckling point and wavelength of the wrinkles are determined by the material properties and geometry of the bilayer system.[158] However, the wrinkling morphologies are strongly dependent on the nature of the stress applied. For a uniaxial stress state, where compression of the wrinkling system is applied mechanically along a single axis, it will result in the formation of long, straight wrinkles aligned perpendicular to the direction of the applied compression (Figure 2.10a). A much richer diversity of patterns can be achieved through the application of biaxial stresses (Figure 2.10b). Furthermore, with changing the relative strain in the planar directions, the top layer can buckle into various two-dimensional wrinkling patterns such as triangular, herringbone, stripes, checkerboards, hexagonal, and labyrinths structures.[163–165]

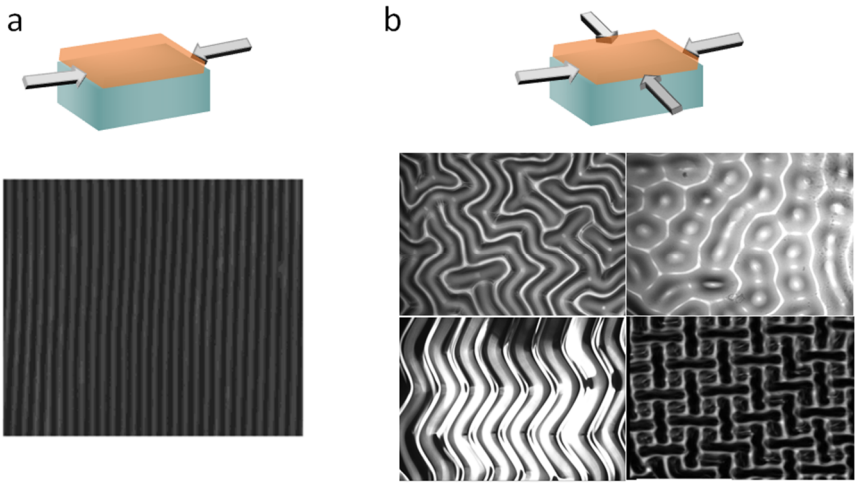

Figure 2.10 Examples of wrinkle morphologies. **a**) Uniaxial stress state. **b**) Biaxial stress states. The optical microscopy images in **a** and in bottom right corner of **b** are taken from ref.[166], the other images are obtained in this Thesis.

2.5.4 Hydrogels with gradient structures

Hydrogels with gradient structures can be achieved by either a gradient distribution of polymer chains or fillers. The gradient structures allow complex shape deformations like folding, bending, curving and also wrinkling. Fan[167] etc. demonstrated a gradient hydrogel taking advantage of graphene oxide absorbing UV light that led to a gradient formation of light intensity along the irradiation axis. Gel precursors which were exposed to higher light intensity crosslinked to a higher degree in comparison with regions subject to lower light intensity, thus leading to a gradient in crosslink density with depth. The synthesized hydrogel sheets exhibited ultrafast inverse snapping deformation and can be programmed to achieve different structures and actuation behaviors.

Guvendiren et al. reported a simple alternative to fabricating gradient hydrogel structures by UV crosslinking gel precursors in air.[168] Due to oxygen inhibition of the radical polymerization at the surface, a gradient in crosslink density with depth was created. The surface that was in contact with air had the lowest crosslink density. The crosslink density increased with depth and remained constant after reaching a critical depth for oxygen diffusion. The modulus gradient, and hence

osmotic pressure generated by swelling, was controlled by the concentrations of initiator, precursor viscosity, exposure time, and UV intensity. Based on the gradient structure, the modulus mismatch in the gel caused the generation of a wide range of surface patterns including random, lamellar, peanut, and hexagonal structures.

2.6 Conclusions

Compared with traditional hydrogels, NC hydrogels attract increasing attention because of their specific mechanical and functional properties. Versatile synthesis techniques (in-situ polymerization, in-situ formation of the NPs, or physical mixing), the variety of NPs (carbon-based, metallic, nanoclay, or polymeric NPs) and different structural designs (isotropic and anisotropic structures) have allowed for the creation of hydrogel nanocomposites with tailored size, shape and composition, suitable for a wide range of applications.

The synthesis, properties and applications of AuNPs, as typical plasmonic particles, are in the focus in this overview. Combined with redox and thermo-responsive hydrogels, AuNPs are able to form in-situ. The AuNP/hydrogel composites are granted with light-responsive properties due to the plasmonic heating behavior. These nanocomposite hydrogels integrate the properties of NPs with stimuli-responsive hydrogels, offering enhanced or new properties compared to the native materials.

From the perspective of structural design, efforts have been made to fabricate NC gels with anisotropic structures. Through constructing oriented, bilayer, gradient as well as other anisotropic structures, various deformations including bending, twisting, rolling, creasing, wrinkling, and complex shape transformations could be achieved, with potential applications as actuators, grippers, walkers, valves etc. which are able to adapt to complex and dynamic environments.

We believe that there will be a vigorous development in AuNP/hydrogel composite hydrogels from design to applications, providing new ideas for the fabrication and applications of a new generation of functional hydrogels.

References

[1] Rose, J. C.; Gehlen, D. B.; Haraszti, T.; Köhler, J.; Licht, C. J.; De Laporte, L. Biofunctionalized Aligned Microgels Provide 3D Cell Guidance to Mimic Complex Tissue Matrices. *Biomaterials* **2018**, *163*, 128–141.

[2] Gaharwar, A. K.; Peppas, N. A.; Khademhosseini, A. Nanocomposite Hydrogels for Biomedical Applications. *Biotechnol. Bioeng.* **2014**, *111*, 441–453.

[3] Xia, L. W.; Xie, R.; Ju, X. J.; Wang, W.; Chen, Q.; Chu, L. Y. Nano-Structured Smart Hydrogels with Rapid Response and High Elasticity. *Nat. Commun.* **2013**, *4*, 1–11.

[4] Le, X.; Lu, W.; Zhang, J.; Chen, T. Recent Progress in Biomimetic Anisotropic Hydrogel Actuators. *Adv. Sci.* **2019**, *6,*1801584

[5] Li, S.; Dong, S.; Xu, W.; Tu, S.; Yan, L.; Zhao, C.; Ding, J.; Chen, X. Antibacterial Hydrogels. *Adv. Sci.* **2018**, *5, 17000527*

[6] Tavakoli, S.; Klar, A. S. Advanced Hydrogels as Wound Dressings. *Biomolecules* **2020**. *10*, 1169.

[7] Liu, X.; Liu, J.; Lin, S.; Zhao, X. Hydrogel Machines. *Materials Today* **2020**, *36*, 102-104

[8] Chimene, D.; Kaunas, R.; Gaharwar, A. K. Hydrogel Bioink Reinforcement for Additive Manufacturing: A Focused Review of Emerging Strategies. *Adv. Mater.***2020**, *32*, 1902026

[9] Zarrintaj, P.; Jouyandeh, M.; Ganjali, M. R.; Hadavand, B. S.; Mozafari, M.; Sheiko, S. S.; Vatankhah-Varnoosfaderani, M.; Gutiérrez, T. J.; Saeb, M. R. Thermo-Sensitive Polymers in Medicine: A Review. *Eur. Polym. J.* **2019**, *117*, 402–423.

[10] Zheng, W. J.; An, N.; Yang, J. H.; Zhou, J.; Chen, Y. M. Tough Al-Alginate/Poly(N -Isopropylacrylamide) Hydrogel with Tunable LCST for Soft Robotics. *ACS Appl. Mater. Interfaces* **2015**, *7*, 1758–1764.

[11] Xu, L.; Liu, N.; Cao, Y.; Lu, F.; Chen, Y.; Zhang, X.; Feng, L.; Wei, Y. Mercury Ion Responsive Wettability and Oil/Water Separation. *ACS Appl. Mater. Interfaces* **2014**, *6*, 13324–13329.

[12] Sui, X.; Feng, X.; Di Luca, A.; Van Blitterswijk, C. A.; Moroni, L.; Hempenius, M. A.; Vancso, G. J. Poly(N-Isopropylacrylamide)-Poly(Ferrocenylsilane) Dual-Responsive Hydrogels: Synthesis, Characterization and Antimicrobial Applications. *Polym. Chem.* **2013**, *4*, 337–342.

[13] Hempenius, M. A.; Cirmi, C.; Lo Savio, F.; Song, J.; Vancso, G. J. Poly(Ferrocenylsilane) Gels and Hydrogels with Redox-Controlled Actuation. *Macromol. Rapid Commun.* **2010**, *31*, 772–783.

[14] He, J.; Shi, M.; Liang, Y.; Guo, B. Conductive Adhesive Self-Healing Nanocomposite Hydrogel Wound Dressing for Photothermal Therapy of Infected Full-Thickness Skin Wounds. *Chem. Eng. J.* **2020**, *394*, 124888.
[15] Nakahata, M.; Takashima, Y.; Yamaguchi, H.; Harada, A. Redox-Responsive Self-Healing Materials Formed from Host Guest Polymers. *Nat. Commun.* **2011**, *2*.
[16] Downs, F. G.; Lunn, D. J.; Booth, M. J.; Sauer, J. B.; Ramsay, W. J.; Klemperer, R. G.; Hawker, C. J.; Bayley, H. Multi-Responsive Hydrogel Structures from Patterned Droplet Networks. *Nat. Chem.* **2020**, *12*, 363–371.
[17] Sakurai, Y.; Okano, T. Influence of Freely Mobile Grafted Chain Length on dynamic properties of comb-type grafted poly (N-isopropylacrylamide) hydrogels. *Macromolecules* **1995**, 28–31.
[18] Zhang, C. L.; Cao, F. H.; Wang, J. L.; Yu, Z. L.; Ge, J.; Lu, Y.; Wang, Z. H.; Yu, S. H. Highly Stimuli-Responsive Au Nanorods/Poly(N-Isopropylacrylamide) (PNIPAM) Composite Hydrogel for Smart Switch. *ACS Appl. Mater. Interfaces* **2017**, *9*, 24857–24863.
[19] Lee, E.; Kim, D.; Kim, H.; Yoon, J. Photothermally Driven Fast Responding Photo-Actuators Fabricated with Comb-Type Hydrogels and Magnetite Nanoparticles. *Sci. Rep.* **2015**, *5*, 1–8.
[20] Thoniyot, P.; Tan, M. J.; Karim, A. A.; Young, D. J.; Loh, X. J. Nanoparticle–Hydrogel Composites: Concept, Design, and Applications of These Promising, Multi-Functional Materials. *Adv. Sci.* **2015**, *2*, 1–13.
[21] Feng, X.; Hempenius, M. A.; Vancso, G. J. Metal Nanoparticle Foundry with Redox Responsive Hydrogels. *Macromol. Chem. Phys.* **2018**, *219*, 1–7.
[22] Dewangan, R.; Sharma, A. K.; Kumar, N.; Maiti, S. K.; Singh, H.; Gangwar, A. K.; Shrivastava, S.; Sonal; Kumar, A. In-Vitro Biocompatibility Determination of Bladder Acellular Matrix Graft. *Trends Biomater. Artif. Organs* **2012**, *25*, 161–171.
[23] Chen, X.; Mao, S. S. Titanium Dioxide Nanomaterials: Synthesis, Properties, Modifications and Applications. *Chem. Rev.* **2007**, *107*, 2891–2959.
[24] Xia, Y.; Xiong, Y.; Lim, B.; Skrabalak, S. E. Shape-Controlled Synthesis of Metal Nanocrystals: Simple Chemistry Meets Complex Physics? *Angew. Chemie - Int. Ed.* **2009**, *48*, 60–103.
[25] Nagarajan, R. Nanoparticles: Building Blocks for Nanotechnology. *ACS Symp. Ser.* **2008**, *996*, 2–14.
[26] Häkkinen, H. The Gold-Sulfur Interface at the Nanoscale. *Nat. Chem.* **2012**, *4*, 443–455.
[27] Daniel, M. C. M.; Astruc, D. Gold Nanoparticles: Assembly, Supramolecular Chemistry, Quantum-Size Related Properties and Applications toward Biology, Catalysis and Nanotechnology. *Chem. Rev.* **2004**, *104*, 293–346.
[28] Brust, M.; Walker, M.; Bethell, D.; Schiffrin, D. J.; Whyman, R. Synthesis of Thiol-Derivatised Gold Nanoparticles in a Two-Phase Liquid–Liquid System. *Chem. Commun.* **2000**, 7, 801–802.

[29] Boal, A. K.; Ilhan, F.; Derouchey, J. E.; Thurn-Albrecht, T.; Russell, T. P.; Rotello, V. M. Self-Assembly of Nanoparticles into Structured Spherical and Network Aggregates. *Nature* **2000**, *404*, 746–748.

[30] Li, D.; Zhang, Y.; Jiang, J.; Li, J. Electroactive Gold Nanoparticles Protected by 4-Ferrocene Thiophenol Monolayer. *J. Colloid Interface Sci.* **2003**, *264*, 109–113.

[31] Yeh, Y.-C.; Creran, B.; Rotello, V. M. Gold Nanoparticles: Preparation, Properties, and Applications in Bionanotechnology. *Nanoscale* **2012**, *4*, 1871–1880.

[32] Ciganda, R.; Gu, H.; Hernandez, R.; Escobar, A.; Martínez, A.; Yates, L.; Moya, S.; Ruiz, J.; Astruc, D. Electrostatic Assembly of Functional and Macromolecular Ferricinium Chloride-Stabilized Gold Nanoparticles. *Inorg. Chem.* **2017**, *56*, 2784–2791.

[33] Vaklev, N. L.; Vasileva, P.; Dushkin, C. Synthesis of Gold Nanoparticles via Hydrogen Peroxide Reduction Enhanced by Sonication. *Nanosci. Nanotechnol.* **2007**, *7*, 70–73.

[34] Faraday, M. Experimental Relations of Gold (and Other Metals) to Light. *Phil. Trans. R. Soc.* **1857**, *147*, 145–181.

[35] Daniel, M. C.; Astruc, D. Gold Nanoparticles: Assembly, Supramolecular Chemistry, Quantum-Size-Related Properties, and Applications Toward Biology, Catalysis, and Nanotechnology. *Chem. Rev.* **2004**, *104*, 293–346.

[36] Song, J. H.; Kim, Y. J.; Kim, J. S. Synthesis of Gold Nanoparticles Using N,N-Dimethylacetoacetamide: Size and Shape Control by the Reaction Temperature. *Curr. Appl. Phys.* **2006**, *6*, 216–218.

[37] Newman, J. D. S.; Blanchard, G. J. Formation of Gold Nanoparticles Using Amine Reducing Agents. *Langmuir* **2006**, *22*, 5882–5887.

[38] Tatarchuk, V. V.; Dobrolyubova, Y. O.; Druzhinina, I. A.; Zaikovskii, V. I.; Gevko, P. N.; Maksimovskii, E. A.; Gromilov, S. A. Facile Synthesis of Gold Nanoparticles in Aqueous Acrylamide Solution. *Russ. J. Inorg. Chem.* **2016**, *61*, 535–543.

[39] Kundu, S.; Pal, A.; Ghosh, S. K.; Nath, S.; Panigrahi, S.; Praharaj, S.; Pal, T. A New Route to Obtain Shape-Controlled Gold Nanoparticles from Au(III)-β-Diketonates. *Inorg. Chem.* **2004**, *43*, 5489–5491.

[40] Turkevich, J.; Stevenson, P.C.; Hillier, J.; A Study of The Nucleation and Growth Processes in The Synthesis of Colloidal Gold. *Discussions of the Faraday Society*, **1951**, *11*, 55-75.

[41] Brown, K. R.; Fox, A. P.; Natan, M. J. Morphology-Dependent Electrochemistry of Cytochromec at Au Colloid-Modified SnO_2 Electrodes. *J. Am. Chem. Soc.* **1996**, *118*, 1154–1157.

[42] Brust, M.; Walker, M.; Bethell, D.; Schiffrin, D. J.; Whyman, R. Synthesis of Thiol-Derivatised Gold Nanoparticles in a Two-Phase Liquid–Liquid System., *Chem. Commun.* **2000**, *7*, 801–802.

[43] Brust, M.; Fink, J.; Bethell, D.; Schiffrin, D. J.; Kiely, C. Synthesis and Reactions of Functionalised Gold Nanoparticles. *J. Chem. Soc. Chem. Commun.* **1995**, *16*, 1655–1656.

[44] Heuer-Jungemann, A.; Feliu, N.; Bakaimi, I.; Hamaly, M.; Alkilany, A.; Chakraborty, I.; Masood, A.; Casula, M. F.; Kostopoulou, A.; Oh, E.; Susumu, K.; Stewart, M. H.; Medintz, I. L.; Stratakis, E.; Parak, W. J.; Kanaras, A. G. The Role of Ligands in the Chemical Synthesis and Applications of Inorganic Nanoparticles. *Chem. Rev.* **2019**, *119*, 4819–4880.

[45] Jana, N. R.; Gearheart, L.; Murphy, C. J. Seeding Growth for Size Control of 5-40 Nm Diameter Gold Nanoparticles. *Langmuir* **2001**, *17*, 6782–6786.

[46] Astruc, D. Why Is Ferrocene so Exceptional? *Eur. J. Inorg. Chem.* **2017**, *2017*, 6–29.

[47] Wang, Q.; Fu, F.; Martinez-Villacorta, A. M.; Moya, S.; Salmon, L.; Vax, A.; Hunel, J.; Ruiz, J.; Astruc, D. Electron Flow in Large Metallomacromolecules and Electronic Switching of Nanoparticle Stabilization: Click Ferrocenyl Dentromers That Reduce Au^{III} to Au Nanoparticles. *Chem. - A Eur. J.* **2018**, *24*, 12686–12694.

[48] Rapakousiou, A.; Deraedt, C.; Irigoyen, J.; Wang, Y.; Pinaud, N.; Salmon, L.; Ruiz, J.; Moya, S.; Astruc, D. Synthesis and Redox Activity of "Clicked" Triazolylbiferrocenyl Polymers, Network Encapsulation of Gold and Silver Nanoparticles and Anion Sensing. *Inorg. Chem.* **2015**, *54*, 2284–2299.

[49] Ciganda, R.; Irigoyen, J.; Gregurec, D.; Hernández, R.; Moya, S.; Wang, C.; Ruiz, J.; Astruc, D. Liquid-Liquid Interfacial Electron Transfer from Ferrocene to Gold(III): An Ultrasimple and Ultrafast Gold Nanoparticle Synthesis in Water under Ambient Conditions. *Inorg. Chem.* **2016**, *55*, 6361–6363.

[50] Liu, X.; Liu, F.; Astruc, D.; Lin, W.; Gu, H. Highly-Branched Amphiphilic Organometallic Dendronized Diblock Copolymer: ROMP Synthesis, Self-Assembly and Long-Term Au and Ag Nanoparticle Stabilizer for High-Efficiency Catalysis. *Polymer* **2019**, *173*, 1–10.

[51] Rapakousiou, A.; Deraedt, C.; Gu, H.; Salmon, L.; Belin, C.; Ruiz, J.; Astruc, D. Mixed-Valent Click Intertwined Polymer Units Containing Biferrocenium Chloride Side Chains Form Nanosnakes That Encapsulate Gold Nanoparticles. *J. Am. Chem. Soc.* **2014**, *136*, 13995–13998.

[52] Zhang, K.; Feng, X.; Ye, C.; Hempenius, M. A.; Vancso, G. J. Hydrogels with a Memory: Dual-Responsive, Organometallic Poly(Ionic Liquid)s with Hysteretic Volume-Phase Transition. *J. Am. Chem. Soc.* **2017**, *139*, 10029–10035.

[53] Sui, X.; Hempenius, M. A.; Vancso, G. J. Redox-Active Cross-Linkable Poly(Ionic Liquid)S. *J. Am. Chem. Soc.* **2012**, *134*, 4023–4025.

[54] Zhang, K.; Feng, X.; Sui, X.; Hempenius, M. A.; Vancso, G. J. Breathing Pores on Command: Redox-Responsive Spongy Membranes from Poly(Ferrocenylsilane)s. *Angew. Chemie - Int. Ed.* **2014**, *53*, 13789–13793.

[55] Feng, X.; Sui, X.; Hempenius, M. A.; Vancso, G. J. Electrografting of Stimuli-Responsive, Redox Active Organometallic Polymers to Gold from Ionic Liquids. *J. Am. Chem. Soc.* **2014**, *136*, 7865–7868.

[56] Song, J.; Tan, Y. N.; Jańczewski, D.; Hempenius, M. A.; Xu, J. W.; Tan, H. R.; Vancso, G. J. Poly(Ferrocenylsilane) Electrolytes as a Gold Nanoparticle Foundry: "Two-in-One" Redox Synthesis and Electrosteric Stabilization, and Sensing Applications. *Nanoscale* **2017**, *9*, 19255–19262.

[57] Amendola, V.; Pilot, R.; Frasconi, M.; Maragò, O. M.; Iatì, M. A. Surface Plasmon Resonance in Gold Nanoparticles: A Review. *J. Phys. Condens. Matter* **2017**, *29*, 203002.

[58] Saha, K.; Agasti, S. S.; Kim, C.; Li, X.; Rotello, V. M. Gold Nanoparticles in Chemical and Biological Sensing. *Chem. Rev.* **2012**, *112*, 2739–2779.

[59] Shi, Q.; Xia, H.; Li, P.; Wang, Y. S.; Wang, L.; Li, S. X.; Wang, G.; Lv, C.; Niu, L. G.; Sun, H. B. Photothermal Surface Plasmon Resonance and Interband Transition-Enhanced Nanocomposite Hydrogel Actuators with Hand-Like Dynamic Manipulation. *Adv. Opt. Mater.* **2017**, *5*, 1–9.

[60] Huang, X.; El-Sayed, M. A. Gold Nanoparticles: Optical Properties and Implementations in Cancer Diagnosis and Photothermal Therapy. *J. Adv. Res.* **2010**, *1*, 13–28.

[61] Templeton, A. C.; Pietron, J. J.; Murray, R. W.; Mulvaney, P. Solvent Refractive Index and Core Charge Influences on the Surface Plasmon Absorbance of Alkanethiolate Monolayer-Protected Gold Clusters. *J. Phys. Chem. B* **2000**, *104*, 564–570.

[62] Link, S.; El-Sayed, M. A. Size and Temperature Dependence of the Plasmon Absorption of Colloidal Gold Nanoparticles. *J. Phys. Chem. B* **1999**, *103*, 4212–4217.

[63] Abadeer, N. S.; Murphy, C. J. Recent Progress in Cancer Thermal Therapy Using Gold Nanoparticles. *J. Phys. Chem. C* **2016**, *120*, 4691–4716.

[64] Wu, Y.; Ali, M. R. K.; Chen, K.; Fang, N.; El-Sayed, M. A. Gold Nanoparticles in Biological Optical Imaging. *Nano Today* **2019**, *24*, 120–140.

[65] Hu, M.; Chen, J.; Li, Z. Y.; Au, L.; Hartland, G. V.; Li, X.; Marquez, M.; Xia, Y. Gold Nanostructures: Engineering Their Plasmonic Properties for Biomedical Applications. *Chem. Soc. Rev.* **2006**, *35*, 1084–1094.

[66] Amina, S. J.; Guo, B. A Review on the Synthesis and Functionalization of Gold Nanoparticles as a Drug Delivery Vehicle. *Int. J. Nanomedicine* **2020**, *15*, 9823–9857.

[67] Obare, S. O.; Hollowell, R. E.; Murphy, C. J. Sensing Strategy for Lithium Ion Based on Gold Nanoparticles. *Langmuir* **2002**, *18*, 10407–10410.

[68] Wang, X.; Ramström, O.; Yan, M. Quantitative Analysis of Multivalent Ligand Presentation on Gold Glyconanoparticles and the Impact on Lectin Binding. *Anal. Chem.* **2010**, *82*, 9082–9089.

[69] Li, X.; Wang, J.; Sun, L.; Wang, Z. Gold Nanoparticle-Based Colorimetric Assay for Selective Detection of Aluminium Cation on Living Cellular Surfaces. *Chem. Commun.* **2010**, *46*, 988–990.

[70] Jiang, C.; Markutsya, S.; Pikus, Y.; Tsukruk, V. V. Freely Suspended Nanocomposite Membranes as Highly Sensitive Sensors. *Nat. Mater.* **2004**, *3*, 721–728.

[71] You, C. C.; Miranda, O. R.; Gider, B.; Ghosh, P. S.; Kim, I. B.; Erdogan, B.; Krovi, S. A.; Bunz, U. H. F.; Rotello, V. M. Detection and Identification of Proteins Using Nanoparticle-Fluorescent Polymer "chemical Nose" Sensors. *Nat. Nanotechnol.* **2007**, *2*, 318–323.

[72] Guo, S.; Wang, E. Synthesis and Electrochemical Applications of Gold Nanoparticles. *Anal. Chim. Acta* **2007**, *598*, 181–192.

[73] El-Sayed, I. H.; Huang, X.; El-Sayed, M. A. Surface Plasmon Resonance Scattering and Absorption of Anti-EGFR Antibody Conjugated Gold Nanoparticles in Cancer Diagnostics: Applications in Oral Cancer. *Nano Lett.* **2005**, *5*, 829–834.

[74] Qian, W.; Huang, X.; Kang, B.; El-Sayed, M. A. Dark-Field Light Scattering Imaging of Living Cancer Cell Component from Birth through Division Using Bioconjugated Gold Nanoprobes. *J. Biomed. Opt.* **2010**, *15*, 046025.

[75] Yguerabide, J.; Yguerabide, E. E. Resonance Light Scattering Particles as Ultrasensitive Labels for Detection of Analytes in a Wide Range of Applications. *J. Cell. Biochem.* **2001**, *84*, 71–81.

[76] Matsumura, S.; Hlil, A. R.; Lepiller, C.; Gaudet, J.; Guay, D.; Shi, Z.; Holdcroft, S.; Hay, A. S. Stability and Utility of Pyridyl Disulfide Functionality in RAFT and Conventional Radical Polymerizations. *J. Polym. Sci. Part A Polym. Chem.* **2008**, *46*, 7207–7224.

[77] Beebe, D. J.; Moore, J. S.; Bauer, J. M.; Yu, Q.; Liu, R. H.; Devadoss, C.; Jo, B. H. Functional Hydrogel Structures for Autonomous Flow Control inside Microfluidic Channels. *Nature* **2000**, *404*, 588–590.

[78] Dragan, E. S. Design and Applications of Interpenetrating Polymer Network Hydrogels. A Review. *Chem. Eng. J.* **2014**, *243*, 572–590.

[79] Matricardi, P.; Di Meo, C.; Coviello, T.; Hennink, W. E.; Alhaique, F. Interpenetrating Polymer Networks Polysaccharide Hydrogels for Drug Delivery and Tissue Engineering. *Adv. Drug Deliv. Rev.* **2013**, *65*, 1172–1187.

[80] Wei, W.; Hu, X.; Qi, X.; Yu, H.; Liu, Y.; Li, J.; Zhang, J.; Dong, W. A Novel Thermo-Responsive Hydrogel Based on Salecan and Poly(N-Isopropylacrylamide): Synthesis and Characterization. *Colloids Surfaces B: Biointerfaces* **2015**, *125*, 1–11.

[81] Zhang, X. Z.; Wu, D. Q.; Chu, C. C. Synthesis, Characterization and Controlled Drug Release of Thermosensitive IPN-PNIPAAm Hydrogels. *Biomaterials* **2004**, *25*, 3793–3805.

[82] Stuart, M. A. C.; Huck, W. T. S.; Genzer, J.; Müller, M.; Ober, C.; Stamm, M.; Sukhorukov, G. B.; Szleifer, I.; Tsukruk, V. V.; Urban, M.; Winnik, F.; Zauscher, S.; Luzinov, I.; Minko, S. Emerging Applications of Stimuli-Responsive Polymer Materials. *Nat. Mater.* **2010**, *9*, 101–113.

[83] Schild, H. G. Poly(N-Isopropylacrylamide): Experiment, Theory and Application. *Prog. Polym. Sci.* **1992**, *17*, 163–249.

[84] Weissman, J. M.; Sunkara, H. B.; Tse, A. S.; Asher, S. A. Thermally Switchable Periodicities and Diffraction from Mesoscopically Ordered Materials. *Science* **2008**, *274*, 959–960.
[85] Heskins, M.; Guillet, J. E. Solution Properties of Poly (N-Isopropylacrylamide). *J. Macromol. Sci. A* 1968, *2*, 1441-55.
[86] Li, L.; Scheiger, J. M.; Levkin, P. A. Design and Applications of Photoresponsive Hydrogels. *Adv. Mater.* **2019**, *31*.
[87] Shi, K.; Liu, Z.; Wei, Y. Y.; Wang, W.; Ju, X. J.; Xie, R.; Chu, L. Y. Near-Infrared Light-Responsive Poly(N-Isopropylacrylamide)/Graphene Oxide Nanocomposite Hydrogels with Ultrahigh Tensibility. *ACS Appl. Mater. Interfaces* **2015**, *7*, 27289–27298.
[88] Deng, Z.; Guo, Y.; Zhao, X.; Ma, P. X.; Guo, B. Multifunctional Stimuli-Responsive Hydrogels with Self-Healing, High Conductivity, and Rapid Recovery through Host-Guest Interactions. *Chem. Mater.* **2018**, *30*, 1729–1742.
[89] Huang, K.; Wu, H.; Jiang, F.; Shen, G.; Wang, L. On the Near-Infrared Light-Responsive and Mechanical Properties of PNIPAM-Based Nanocomposite Hydrogels. *Polym. Degrad. Stab.* **2018**, *156*, 228–233.
[90] Bertrand, O.; Gohy, J. F. Photo-Responsive Polymers: Synthesis and Applications. *Polym. Chem.* **2017**, *8*, 52–73.
[91] Wang, D.; Zhao, W.; Wei, Q.; Zhao, C.; Zheng, Y. Photoswitchable Azobenzene/Cyclodextrin Host-Guest Complexes: From UV- to Visible/Near-IR-Light-Responsive Systems. *ChemPhotoChem* **2018**, *2*, 403–415.
[92] Wang, D.; Wagner, M.; Saydjari, A. K.; Mueller, J.; Winzen, S.; Butt, H. J.; Wu, S. A Photoresponsive Orthogonal Supramolecular Complex Based on Host–Guest Interactions. *Chem. - A Eur. J.* **2017**, *23*, 2628–2634.
[93] Hauser, A. W.; Evans, A. A.; Na, J. H.; Hayward, R. C. Photothermally Reprogrammable Buckling of Nanocomposite Gel Sheets. *Angew. Chemie - Int. Ed.* **2015**, *54*, 5434–5437.
[94] Zhu, C. H.; Lu, Y.; Peng, J.; Chen, J. F.; Yu, S. H. Photothermally Sensitive Poly(N-Isopropylacrylamide)/Graphene Oxide Nanocomposite Hydrogels as Remote Light-Controlled Liquid Microvalves. *Adv. Funct. Mater.* **2012**, *22*, 4017–4022.
[95] Zhang, H.; Koens, L.; Lauga, E.; Mourran, A.; Möller, M. A Light-Driven Microgel Rotor. *Small* **2019**, *1903379*, 1903379.
[96] Hou, H.; Yin, J.; Jiang, X. Smart Patterned Surface with Dynamic Wrinkles. *Acc. Chem. Res.* **2019**, *52*, 1025–1035.
[97] Shao, J.; Ruan, C.; Xie, H.; Li, Z.; Wang, H.; Chu, P. K.; Yu, X. F. Black-Phosphorus-Incorporated Hydrogel as a Sprayable and Biodegradable Photothermal Platform for Postsurgical Treatment of Cancer. *Adv. Sci.* **2018**, *5,* 1700848.

[98] Deng, G.; Li, F.; Yu, H.; Liu, F.; Liu, C.; Sun, W.; Jiang, H.; Chen, Y. Dynamic Hydrogels with an Environmental Adaptive Self-Healing Ability and Dual Responsive Sol-Gel Transitions. *ACS Macro Lett.* **2012**, *1*, 275–279.

[99] Ni, M.; Zhang, N.; Xia, W.; Wu, X.; Yao, C.; Liu, X.; Hu, X. Y.; Lin, C.; Wang, L. Dramatically Promoted Swelling of a Hydrogel by Pillar[6]Arene-Ferrocene Complexation with Multistimuli Responsiveness. *J. Am. Chem. Soc.* **2016**, *138*, 6643–6649.

[100] Sun, Z.; Lv, F.; Cao, L.; Liu, L.; Zhang, Y.; Lu, Z. Multistimuli-Responsive, Moldable Supramolecular Hydrogels Cross-Linked by Ultrafast Complexation of Metal Ions and Biopolymers. *Angew. Chemie - Int. Ed.* **2015**, *54*, 7944–7948.

[101] Gallei, M.; Rüttiger, C. Recent Trends in Metallopolymer Design: Redox-Controlled Surfaces, Porous Membranes, and Switchable Optical Materials Using Ferrocene-Containing Polymers. *Chem. - A Eur. J.* **2018**, *24*, 10006–10021.

[102] Hailes, R. L. N.; Oliver, A. M.; Gwyther, J.; Whittell, G. R.; Manners, I. Polyferrocenylsilanes: Synthesis, Properties, and Applications. *Chem. Soc. Rev.* **2016**, *45*, 5358–5407.

[103] Foucher, D. A.; Tang, B.; Manners, I. Ring-opening polymerization of strained, ring-tilted ferrocenophanes: a route to high-molecular-weight poly (ferrocenylsilanes). *J. Am. Chem. Soc.* **1992**, 6246–6248.

[104] Feng, X.; Zhang, K.; Chen, P.; Sui, X.; Hempenius, M. A.; Liedberg, B.; Vancso, G. J. Highly Swellable, Dual-Responsive Hydrogels Based on PNIPAM and Redox Active Poly(Ferrocenylsilane) Poly(Ionic Liquid)s: Synthesis, Structure, and Properties. *Macromol. Rapid Commun.* **2016**, *37*, 1939–1944.

[105] Sui, X.; Feng, X.; Hempenius, M. A.; Vancso, G. J. Redox Active Gels: Synthesis, Structures and Applications. *J. Mater. Chem. B* **2013**, *1*, 1658–1672.

[106] Jin, Y.; Zhao, D.; Huang, Y. Study of Extrudability and Standoff Distance Effect during Nanoclay-Enabled Direct Printing. *Bio-Design Manuf.* **2018**, *1*, 123–134.

[107] Zhao, T.; Yu, R.; Li, S.; Li, X.; Zhang, Y.; Yang, X.; Zhao, X.; Wang, C.; Liu, Z.; Dou, R.; Huang, W. Superstretchable and Processable Silicone Elastomers by Digital Light Processing 3D Printing. *ACS Appl. Mater. Interfaces* **2019**, *11*, 14391–14398.

[108] Fang, X.; Sun, J. One-Step Synthesis of Healable Weak-Polyelectrolyte-Based Hydrogels with High Mechanical Strength, Toughness and Excellent Self-Recovery. *ACS Macro Lett.* **2019**, *8*, 500–505.

[109] De France, K. J.; Hoare, T.; Cranston, E. D. Review of Hydrogels and Aerogels Containing Nanocellulose. *Chem. Mater.* **2017**, *29,* 4609–4631.

[110] Tan, H. L.; Teow, S. Y.; Pushpamalar, J. Application of Metal Nanoparticle–Hydrogel Composites in Tissue Regeneration. Bioengineering 2019, *6*, 1–17.

[111] Rafieian, S.; Mirzadeh, H.; Mahdavi, H.; Masoumi, M. E. A Review on Nanocomposite Hydrogels and Their Biomedical Applications. *IEEE J. Sel. Top. Quantum Electron.* **2019**, *26*, 154–174.
[112] Song, F.; Li, X.; Wang, Q.; Liao, L.; Zhang, C. Nanocomposite Hydrogels and Their Applications in Drug Delivery and Tissue Engineering. *J. Biomed. Nanotechnol.* **2015**, *11*, 40–52.
[113] Ying, Z.; Wang, Q.; Xie, J.; Li, B.; Lin, X.; Hui, S. Novel Electrically-Conductive Electro-Responsive Hydrogels for Smart Actuators with a Carbon-Nanotube-Enriched Three-Dimensional Conductive Network and a Physical-Phase-Type Three-Dimensional Interpenetrating Network. *J. Mater. Chem. C.* **2020**, *8*, 4192–4205.
[114] Satarkar, N. S.; Biswal, D.; Hilt, J. Z. Hydrogel Nanocomposites: A Review of Applications as Remote Controlled Biomaterials. *Soft Matter.* **2010**, *6*, 2364–2371.
[115] Kaniewska, K.; Karbarz, M.; Katz, E. Nanocomposite Hydrogel Films and Coatings – Features and Applications. *Appl. Mater. Today* **2020**, *20*, 100776.
[116] Tokarev, I.; Minko, S. Stimuli-Responsive Hydrogel Thin Films. *Soft Matter.* **2009**, *5*, 511–524.
[117] Bellas, V.; Rehahn, M. Polyferrocenylsilane-Based Polymer Systems. *Angew. Chemie - Int. Ed*. **2007**, *46*, 5082–5104.
[118] Whittell, G. R.; Hager, M. D.; Schubert, U. S.; Manners, I. Functional Soft Materials from Metallopolymers and Metallosupramolecular Polymers. *Nat. Mater.* **2011**, *10*, 176–188.
[119] Khampieng, T.; Brikshavana, P.; Supaphol, P. Silver Nanoparticle-Embedded Poly(Vinyl Pyrrolidone) Hydrogel Dressing: Gamma-Ray Synthesis and Biological Evaluation. *J. Biomater. Sci. Polym. Ed.* **2014**, *25*, 826–842.
[120] Kumaraswamy, S.; Mallaiah, S. H. Swelling and Mechanical Properties of Radiation Crosslinked Au/PVA Hydrogel Nanocomposites. *Radiat. Eff. Defects Solids.* **2016**, *171*, 869–878.
[121] Ahadian, S.; Ramón-Azcón, J.; Estili, M.; Liang, X.; Ostrovidov, S.; Shiku, H.; Ramalingam, M.; Nakajima, K.; Sakka, Y.; Bae, H.; Matsue, T.; Khademhosseini, A. Hybrid Hydrogels Containing Vertically Aligned Carbon Nanotubes with Anisotropic Electrical Conductivity for Muscle Myofiber Fabrication. *Sci. Rep.* **2014**, *4*, 1–11.
[122] Qin, H.; Zhang, T.; Li, H. N.; Cong, H. P.; Antonietti, M.; Yu, S. H. Dynamic Au-Thiolate Interaction Induced Rapid Self-Healing Nanocomposite Hydrogels with Remarkable Mechanical Behaviors. *Chem* **2017**, *3*, 691–705.
[123] Weber, A.; Murray, J. M. Molecular Control Mechanisms in Muscle Contraction. *Physiol. Rev.* **1973**, *53*, 612–672.
[124] Madison, K. C. Barrier Function of the Skin: "La Raison d'Être" of the Epidermis. *J. Invest. Dermatol*. **2003**, *121*, 231–241.
[125] Sophia Fox, A. J.; Bedi, A.; Rodeo, S. A. The Basic Science of Articular Cartilage: Structure, Composition, and Function. *Sports Health* **2009**, *1*, 461–468.

[126] Matsuda, T.; Kawakami, R.; Namba, R.; Nakajima, T.; Gong, J. P. Mechanoresponsive Self-Growing Hydrogels Inspired by Muscle Training. *Science* **2019**, *363*, 504–508.
[127] Shigekura, Y.; Chen, Y. M.; Furukawa, H.; Kaneko, T.; Kaneko, D.; Osada, Y.; Gong, J. P. Anisotropic Pohyion-Complex Gels via Template Polymerization. *Adv. Mater.* **2005**, *17*, 2695–2699.
[128] Sano, K.; Ishida, Y.; Aida, T. Synthesis of Anisotropic Hydrogels and Their Applications. *Angew. Chemie - Int. Ed.* **2018**, *57*, 2532–2543.
[129] Qin, H.; Zhang, T.; Li, N.; Cong, H. P.; Yu, S. H. Anisotropic and Self-Healing Hydrogels with Multi-Responsive Actuating Capability. *Nat. Commun*. **2019**, *10*, 1–11.
[130] Backman, D. E.; LeSavage, B. L.; Shah, S. B.; Wong, J. Y. A Robust Method to Generate Mechanically Anisotropic Vascular Smooth Muscle Cell Sheets for Vascular Tissue Engineering. *Macromol. Biosci.* **2017**, *17*, 1–13.
[131] Amar, M. Ben; Jia, F. Anisotropic Growth Shapes Intestinal Tissues during Embryogenesis. *Proc. Natl. Acad. Sci. U. S. A*. **2013**, *110*, 10525–10530.
[132] Mredha, M. T. I.; Le, H. H.; Tran, V. T.; Trtik, P.; Cui, J.; Jeon, I. Anisotropic Tough Multilayer Hydrogels with Programmable Orientation. *Mater. Horizons*. **2019**, *6*, 1504–1511.
[133] Tang, Z.; Huang, Q.; Liu, Y.; Chen, Y.; Guo, B.; Zhang, L. Uniaxial Stretching Induced Alignment of Carbon Nanotubes in Cross-Linked Elastomer Enabled by Dynamic Cross-Link Reshuffling. *ACS Macro Lett*. **2019**, *8*, 1575–1581.
[134] Mredha, M. T. I.; Guo, Y. Z.; Nonoyama, T.; Nakajima, T.; Kurokawa, T.; Gong, J. P. A Facile Method to Fabricate Anisotropic Hydrogels with Perfectly Aligned Hierarchical Fibrous Structures. *Adv. Mater.* **2018**, *30*, 1–8.
[135] Zhao, W.; Chen, L.; Hu, S.; Shi, Z.; Gao, X.; Silberschmidt, V. V. Printed Hydrogel Nanocomposites: Fine-Tuning Nanostructure for Anisotropic Mechanical and Conductive Properties. *Adv. Compos. Hybrid Mater.* **2020**, *3*, 315–324.
[136] Zhu, Z.; Li, Y.; Xu, H.; Peng, X.; Chen, Y. N.; Shang, C.; Zhang, Q.; Liu, J.; Wang, H. Tough and Thermosensitive Poly(N-Isopropylacrylamide)/Graphene Oxide Hydrogels with Macroscopically Oriented Liquid Crystalline Structures. *ACS Appl. Mater. Interfaces*. **2016**, *8*, 15637–15644.
[137] Kong, W.; Wang, C.; Jia, C.; Kuang, Y.; Pastel, G.; Chen, C.; Chen, G.; He, S.; Huang, H.; Zhang, J.; Wang, S.; Hu, L. Muscle-Inspired Highly Anisotropic, Strong, Ion-Conductive Hydrogels. *Adv. Mater.* **2018**, *30*, 1–7.
[138] Xiao, S.; Lu, X.; Lu, Q. Photosensitive Polymer from Ionic Self-Assembly of Azobenzene Dye and Poly(Ionic Liquid) and Its Alignment Characteristic toward Liquid Crystal Molecules. *Macromolecules* **2007**, *40*, 7944–7950.
[139] Wallace, M.; Cardoso, A. Z.; Frith, W. J.; Iggo, J. A.; Adams, D. J. Magnetically Aligned Supramolecular Hydrogels. *Chem. - A Eur. J.* **2014**, *20*, 16484–16487.

[140] Ye, D.; Yang, P.; Lei, X.; Zhang, D.; Li, L.; Chang, C.; Sun, P.; Zhang, L. Robust Anisotropic Cellulose Hydrogels Fabricated via Strong Self-Aggregation Forces for Cardiomyocytes Unidirectional Growth. *Chem. Mater.* **2018**, *30*, 5175–5183.

[141] Kleinschmidt, F.; Hickl, M.; Saalwächter, K.; Schmidt, C.; Finkelmann, H. Lamellar Liquid Single Crystal Hydrogels: Synthesis and Investigation of Anisotropic Water Diffusion and Swelling. *Macromolecules* **2005**, *38*, 9772–9782.

[142] Ramón-Azcón, J.; Ahadian, S.; Estili, M.; Liang, X.; Ostrovidov, S.; Kaji, H.; Shiku, H.; Ramalingam, M.; Nakajima, K.; Sakka, Y.; Khademhosseini, A.; Matsue, T. Dielectrophoretically Aligned Carbon Nanotubes to Control Electrical and Mechanical Properties of Hydrogels to Fabricate Contractile Muscle Myofibers. *Adv. Mater.* **2013**, *25*, 4028–4034.

[143] Small, W. R.; Paunov, V. N. Dielectrophoretic Fabrication of Electrically Anisotropic Hydrogels with Bio-Functionalised Silver Nanowires. *J. Mater. Chem. B.* **2013**, *1*, 5798–5805.

[144] Paineau, E.; Dozov, I.; Bihannic, I.; Baravian, C.; Krapf, M. E. M.; Philippe, A. M.; Rouzière, S.; Michot, L. J.; Davidson, P. Tailoring Highly Oriented and Micropatterned Clay/Polymer Nanocomposites by Applying an a.c. Electric Field. *ACS Appl. Mater. Interfaces.* **2012**, *4*, 4296–4301.

[145] Inadomi, T.; Ikeda, S.; Okumura, Y.; Kikuchi, H.; Miyamoto, N. Photo-Induced Anomalous Deformation of Poly(N-Isopropylacrylamide) Gel Hybridized with an Inorganic Nanosheet Liquid Crystal Aligned by Electric Field. *Macromol. Rapid Commun.* **2014**, *35*, 1741–1746.

[146] Liu, K.; Han, L.; Tang, P.; Yang, K.; Gan, D.; Wang, X.; Wang, K.; Ren, F.; Fang, L.; Xu, Y.; Lu, Z.; Lu, X. An Anisotropic Hydrogel Based on Mussel-Inspired Conductive Ferrofluid Composed of Electromagnetic Nanohybrids. *Nano Lett.* **2019**, *19*, 8343–8356.

[147] Wu, J.; Gong, X.; Fan, Y.; Xia, H. Physically Crosslinked Poly(Vinyl Alcohol) Hydrogels with Magnetic Field Controlled Modulus. *Soft Matter.* **2011**, *7*, 6205–6212.

[148] Bender, P.; Günther, A.; Tschöpe, A.; Birringer, R. Synthesis and Characterization of Uniaxial Ferrogels with Ni Nanorods as Magnetic Phase. *J. Magn. Magn. Mater.* **2011**, *323*, 2055–2063.

[149] Ajdary, R.; Tardy, B. L.; Mattos, B. D.; Bai, L.; Rojas, O. J.Plant Nanomaterials and Inspiration from Nature: Water Interactions and Hierarchically Structured Hydrogels. *Adv. Mater.* **2020**, *33*, 2001085.

[150] Yang, X.; Qiu, L.; Cheng, C.; Wu, Y.; Ma, Z. F.; Li, D. Ordered Gelation of Chemically Converted Graphene for Next-Generation Electroconductive Hydrogel Films. *Angew. Chemie - Int. Ed.* **2011**, *50*, 7325–7328.

[151] Shang, J.; Le, X.; Zhang, J.; Chen, T.; Theato, P. Trends in Polymeric Shape Memory Hydrogels and Hydrogel Actuators. *Polym. Chem.* **2019**, *10*, 1036–1055.

[152] Tang, J.; Li, J.; Vlassak, J. J.; Suo, Z. Adhesion between Highly Stretchable Materials. *Soft Matter.* **2016**, *12,* 1093–1099.
[153] Ma, C.; Li, T.; Zhao, Q.; Yang, X.; Wu, J.; Luo, Y.; Xie, T. Supramolecular Lego Assembly towards Three-Dimensional Multi-Responsive Hydrogels. *Adv. Mater.* **2014**, *26*, 5665–5669.
[154] Feldstein, M. M.; Dormidontova, E. E.; Khokhlov, A. R. Pressure Sensitive Adhesives Based on Interpolymer Complexes. *Prog. Polym. Sci*. **2015**, *42*, 79–153.
[155] Zheng, J.; Xiao, P.; Le, X.; Lu, W.; Théato, P.; Ma, C.; Du, B.; Zhang, J.; Huang, Y.; Chen, T. Mimosa Inspired Bilayer Hydrogel Actuator Functioning in Multi-Environments. *J. Mater. Chem. C*. **2018**, *6*, 1320–1327.
[156] Agarwal, S.; Jiang, S.; Chen, Y. Progress in the Field of Water- and/or Temperature-Triggered Polymer Actuators. *Macromol. Mater. Eng.* **2019**, *304*, 1–19.
[157] Chen, D.; Jin, L.; Suo, Z.; Hayward, R. C. Controlled Formation and Disappearance of Creases. *Mater. Horizons.* **2014**, *1*, 207–213.
[158] Xu, F.; Potier-Ferry, M. Quantitative Predictions of Diverse Wrinkling Patterns in Film/Substrate Systems. *Sci. Rep.* **2017**, *7*, 1–10.
[159] Wu, K.; Sun, Y.; Yuan, H.; Zhang, J.; Liu, G.; Sun, J. Harnessing Dynamic Wrinkling Surfaces for Smart Displays. *Nano Lett.* **2020**, *20*, 4129–4135.
[160] Zeng, S.; Li, R.; Freire, S. G.; Garbellotto, V. M. M.; Huang, E. Y.; Smith, A. T.; Hu, C.; Tait, W. R. T.; Bian, Z.; Zheng, G.; Zhang, D.; Sun, L. Moisture-Responsive Wrinkling Surfaces with Tunable Dynamics. *Adv. Mater.* **2017**, *29*, 1700828.
[161] Wang, Q.; Zhao, X. A Three-Dimensional Phase Diagram of Growth-Induced Surface Instabilities. *Sci. Rep.* **2015**, *5*, 1–10.
[162] Tan, Y.; Hu, B.; Song, J.; Chu, Z.; Wu, W. Bioinspired Multiscale Wrinkling Patterns on Curved Substrates: An Overview; *Springer Singapore* **2020**, *12*, 1-42.
[163] Lin, G.; Li, J.; Xu, Z.; Ge, D.; Sun, W.; Chen, P. Hierarchical Surface Patterns via Global Wrinkling on Curved Substrate for Fluid Drag Control. *Adv. Mater. Interfaces*. **2020**, *2001489*, 1–12.
[164] Jin, L.; Suo, Z. Smoothening Creases on Surfaces of Strain-Stiffening Materials. *J. Mech. Phys. Solids.* **2015**, *74*, 68–79.
[165] Huang, Z.; Hong, W.; Suo, Z. Evolution of Wrinkles in Hard Films on Soft Substrates. *Phys. Rev. E.* **2004**, *70*, 4
[166] Breid, D.; Crosby, A. J. Effect of Stress State on Wrinkle Morphology. *Soft Matter.* **2011**, *7*, 4490–4496.
[167] Le, X. X.; Zhang, Y. C.; Lu, W.; Wang, L.; Zheng, J.; Ali, I.; Zhang, J. W.; Huang, Y. J.; Serpe, M. J.; Yang, X. T.; Fan, X. D.; Chen, T. A Novel Anisotropic Hydrogel with Integrated Self-Deformation and Controllable Shape Memory Effect. Macromol. *Rapid Commun*. **2018**, *39*, 1–6.

[168] Guvendiren, M.; Yang, S.; Burdick, J. A. Swelling-Induced Surface Patterns in Hydrogels with Gradient Crosslinking Density. *Adv. Funct. Mater.* **2009**, *19*, 3038–3045.

Chapter 3

Multi-responsive Wrinkling Surfaces of Polymer Bilayers Utilizing In-Situ Synthesized Plasmonic Nanoparticles

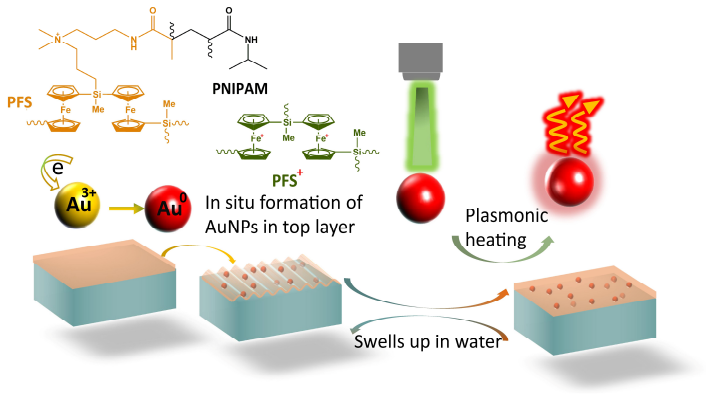

Multi-responsive wrinkling surfaces offer exciting opportunities for tuning surface properties dynamically on demand. Here, we report on the synthesis and properties of a bilayer hydrogel consisting of a compliant poly(acrylamide) bottom layer, and a poly(*N*-isopropylacrylamide) top layer that was copolymerized with redox responsive poly(ferrocenylsilane) (PFS) backbone, originally bearing a methacrylamide cationic side group. The presence of ferrocene in the top layer allowed us to prepare Au nanoparticles (AuNP) in-situ. These Au NPs allowed plasmonic heating of this layer by irradiation with light. Wrinkling of the top layer was induced by exposure to water, while irradiation with light (or external thermal

heating) flattened the layer again. The multi-responsive random and aligned wrinkle patterns formed were used as tunable isotropic and anisotropic light diffusors.

The contents of this chapter have been submitted for publication as: Jinmeng Hao, Lantian Chang, Herman Offerhaus, Mark A. Hempenius, G. Julius Vancso, Multi-responsive Wrinkling Surfaces of Polymer Bilayers Utilizing In-Situ Synthesized Plasmonic Nanoparticles, *submitted.*

3.1 Introduction

Surfaces patterned with micro/nanoscale structures have shown intriguing physical, chemical and biological properties,[1–7] with specific applications including microcontact printing,[8] stretchable electronics,[9] diffraction gratings,[6] controlled cell adhesion and growth platforms etc.[10] Recently, dynamic surface patterns with responsive topographies are attracting attention as these can be reversibly switched between states, using external stimuli such as temperature,[11] light,[12,13] moisture,[2] and changes in pH[14]. Unique dynamic surface morphologies with controllable properties, such as optical characteristics, friction, wettability, and adhesion have been obtained, enabling new applications in numerous fields.[7] Various approaches have been used to create such materials, which exhibit switchable surface patterns. Among these, bilayer systems consisting of a thin rigid layer at the top of a compliant substrate have proven to be suitable structures that are able to display multiple-scale ordering, rich surface patterns and large area surface wrinkles. Based on the linear buckling theory,[15] wrinkling is accompanied by the formation of a new equilibrium state to minimize the system's free energy, when the compressive strain ε exceeds a critical value ε_c. The wavelength (λ) of the wrinkles and the critical strain ε_c for buckling are determined by equations (1) and (2), where h is the thickness of the thin top layer and $\overline{E_f}$ and $\overline{E_s}$ are the plane-strain moduli of the rigid top layer, and the substrate, respectively: [9,15]

$$\lambda = 2\pi h \left(\frac{\overline{E_f}}{3\overline{E_s}}\right)^{1/3} \quad (1)$$

$$\varepsilon_c = -\frac{1}{4}\left(\frac{3\overline{Es}}{\overline{E_f}}\right)^{2/3} \quad (2)$$

Compressive strain ε can be induced by mechanical compression,[5,9] thermal expansion[5,16] and osmotic swelling or shrinkage, for example.[2,17] As an example, Crosby's group[18] reported the fabrication of a reversible wrinkling surface based on a compliant poly(dimethylsiloxane) substrate with a thin rigid oxidized top layer, in which the formation of wrinkles is driven by osmotic swelling and their disappearance is triggered by evaporation. In general, swelling constitutes a simple and economical way to introduce a controllable strain to materials without causing any physical damage and therefore is a facile method for creating uniform wrinkles.

Control over the swelling process, final wrinkle dimensions and geometry of the produced patterns can be achieved by tuning the crosslink density of the film and the solvent quality.[19]

Various stimuli-responsive materials have also been introduced into wrinkling systems, which resulted in smart, controllable, patterned surfaces responsive to different stimuli.[11,13,20] Li[15] reported light-erasable wrinkles on a poly(dimethylsiloxane) (PDMS) substrate with a photo-switchable supramolecular polymer network, consisting of a copolymer (P4VP-PS-PnBA) and carboxylic acid containing anthracene (AN-COOH) as a top layer. The top layer could be cross-linked dynamically through reversible photodimerization of anthracene and by hydrogen bonding between the anthracene carboxylic acid and the pyridine groups of the copolymer.

Here, we describe the use of plasmonic heating as a novel approach to manipulate wrinkling patterns. A bilayer consisting of a compliant poly(acrylamide) (PAAm) bottom layer and a rigid poly(*N*-isopropylacrylamide) (PNIPAM) hydrogel film copolymerized with PFS that originally was bearing a methacrylamide cationic side group was prepared. In situ synthesized gold nanoparticles (AuNPs) were introduced in the PNIPAM containing top layer, using the redox-responsive PFS chains to turn added $HAuCl_4$ salts into AuNPs.[21–23]

3.2 Results and Discussion

3.2.1 Fabrication of light-responsive wrinkles

The fabrication of light-responsive dynamic wrinkling surfaces is illustrated in Figure 3.1. The bilayers comprising an AuNP nanocomposite PNIPAM/PFS hydrogel as top layer and PAAm as bottom layer were made by a stepwise process.

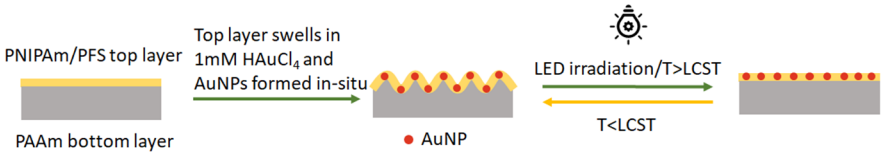

Figure 3.1 Illustration of the fabrication of light-responsive wrinkling polymer surfaces.

A PNIPAM-PFS pre-gel solution in methanol, containing *N*-isopropylacrylamide (NIPAM), *N,N'*-methylenebisacrylamide (MBAm) and a PFS polycation with a crosslinkable methacrylamide group in each repeat unit, was quickly injected into an assembled mould consisting of two glass slides, separated by a polyimide (Kapton) spacer (12 µm in thickness). In the next step the pre-gel was polymerized under ultraviolet irradiation (λ = 365 nm) for 5 min. The covering glass slide was removed, a second spacer (PDMS, 7 mm in thickness) was used to replace the thin Kapton used in the first step, an aqueous PAAm pre-gel solution containing acrylamide (AAm) and MBAm was injected into the mould and the structure was again covered by a glass slide. This construct was then irradiated by UV light (λ = 365 nm) for 15 min. (Further details and a schematic of the experimental procedures can be found in the Supporting Information.) With the bottom layer hydrogel precursor diffusing into the top layer film, an interpenetrating network structure was formed at the interface between the two layers with UV-crosslinking, which ensures a tight interface bonding.

AuNPs and wrinkling surfaces were formed simultaneously during swelling of the hydrogel top layer in 1 mM tetrachloroauric(III) acid trihydrate solution. Due to the presence of PFS chains which possess skeletal ferrocene redox centers, AuNPs were formed in situ in the top layer by direct reduction as the layer swelled in the $HAuCl_4$ solution.[22,24] Nanoparticle formation (Figure 3.2a) was accompanied by a color change from very light amber to pinkish within a few seconds.

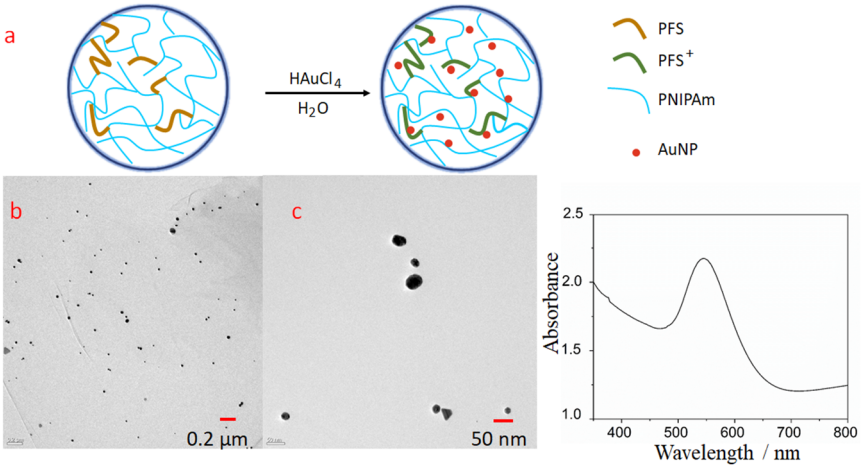

Figure 3.2 (**a**) Schematic illustration of the in-situ formation of AuNPs in the top hydrogel layer. (**b, c, d**) TEM images and UV-Vis absorption spectrum of in-situ synthesized AuNPs.

The TEM images (Figure 3.2b and Figure 3.2c) show that the AuNPs were well dispersed in the hydrogel matrix and have an average diameter of 25 nm. (We note that the AuNP size depends on several parameters, see ref.[24]) Figure 3.2d shows the UV-Vis absorption spectra of the produced AuNPs, which feature a localized Surface Plasmon Resonance (LSPR) peak centered around λ = 542 nm. In the responsive bilayer hydrogel samples, the top layer was uniformly crosslinked with a thickness of 31±2 µm and a compliant PAAm hydrogel layer was used as substrate. The modulus ratio of the top layer to the bottom layer was around 17 (Supporting information, Figure S3). When the top layer swelled up, the compressive stress value in the top layer exceeded the critical value for wrinkle formation, resulting in wrinkled surfaces. According to Equation (1), the estimated pattern wavelength should have a value of around 360 µm which is in good agreement with the experimentally obtained value of around 400 µm (Figure 3.3a, Figure 3.3d).

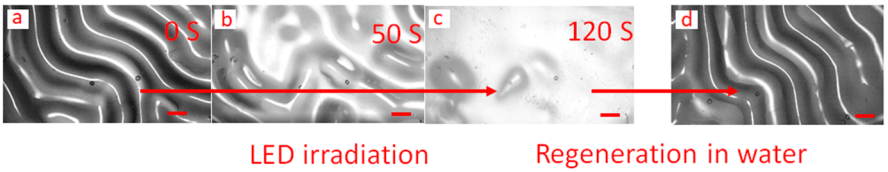

Figure 3.3 (**a** to **c**) Randomly oriented wrinkle pattern formation by swelling in water, and pattern extinction by light irradiation. Optical images of wrinkle disappearance induced by light irradiation. (**d**) Optical image of the wrinkle formation after swelling in water. Scale bar corresponds to 400 µm.

We note that the stress state has a profound effect on the pattern shape and morphology.[29] The profiles of the patterns in the cross section of the buckled surface can exhibit regular wrinkles, doubling and quadrupling of the period, and other more intricate shapes. In Figure 3.4 we show a representative image of a doubled pattern.

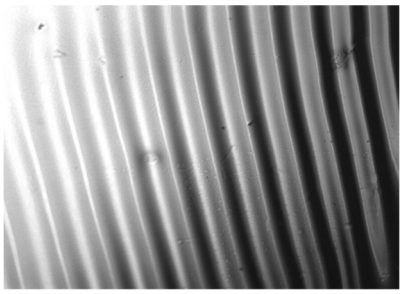

Figure 3.4 Representative image of a period doubled pattern.

3.2.2 Light-responsive behaviour

Following room temperature observations of the wrinkles, we turn now our attention to a pattern, which was created, smoothened by irradiation, and then regenerated by cooling. The observed patterns are displaced in Figure 3.3.

The dynamics of randomly oriented wrinkle generation and extinction was investigated through light irradiation by using a high power LED with a wavelength of λ = 405 nm and swelling in water. (We note that the presence of AuNPs might slightly change the LCST. However, as a first order approximation and due to the very low concentration of the initial $HAuCl_4$, we refer to the electrolyte as "water").

The evolution of the wrinkle pattern was monitored under an optical microscope. As illustrated in Figure 3.3 (a to c), the wrinkles gradually disappeared with light irradiation and completely disappeared after irradiation for 120 s. With light illumination at wavelengths that coincide with the NPs absorption, AuNPs intensively absorbed radiation and converted this into heat efficiently and rapidly based on localized surface plasmon resonances and intrinsic interband transitions.[25] These effects raised the hydrogel temperature above the lower critical solution temperature (LCST). As is well known, PNIPAM hydrogels undergo a significant size reduction above LCST.[26–28] When irradiated by a high power LED for 120 s, the strain induced by swelling could be reduced to zero which totally erased the wrinkles. Wrinkled surfaces were immediately regenerated after the top layer swelled in water at room temperature, which increased the strain by more than 20%. Based on linear buckling theory, the critical strain for the generation of wrinkles in this bilayer system is about 7.7%.[1] (We note that due to evaporation of water from the very thin top layer,

the wrinkled pattern eventually disappears with time when the top layer is dried out. However, this process is significantly slower, and takes place for our films at a time scale of hours.) Forming the wrinkles and regenerating them could be repeated at least 15 times.

Semi-infinite bilayer films possessing layers with different modulus values display random buckling upon swelling, producing labyrinth wrinkle patterns,[9,29] as driving forces that orient the buckles are absent (Figure 3.5).[30] For bilayer hydrogel objects with defined dimensions, however, the bilayer edge containing the boundary between the hard and the soft layer dictates the stress distribution. A larger compressive stress develops parallel to the edge (Figure 3.5, y-direction) compared with the stress normal to the edge (x-direction) and therefore patterns become oriented perpendicular to the edge. Similar oriented buckling phenomena have been observed for patterned bilayer films around steps.[31] In addition to using boundary effects, uniaxial alignment of wrinkles in bilayer films has been achieved for example by patterning rigid top layers,[32] by introducing trigger patterns in flexible bottom layers,[33] or by employing uniaxially prestrained elastomeric substrates.[34] Thus, we anticipate that the pattern geometry will depend on the size and shape of the bilayers.

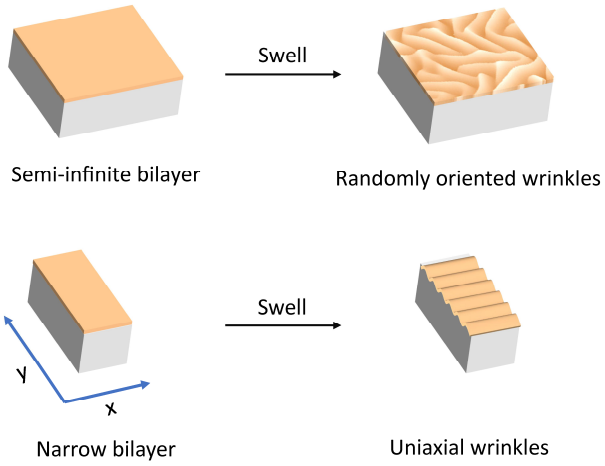

Figure 3.5 Schematic of the formation of responsive wrinkle patterns with changing bilayer dimensions

Now we describe observations, which were obtained for narrow bilayers. We exhibit here the appearance of well-aligned wrinkles. Indeed, these formed when the

width of the originally square-shaped constructs was reduced to 20 % (similar to the scenario depicted in Figure 3.5). The essentially uniaxial stripe patterns obtained for these specimens exhibited a wavelength of around 480 µm. However, a tendency from a single wavelength regular wrinkle pattern to a doubling of the repeat length can be observed. In the Supporting Information we exhibit a surface and a profile plot, respectively, showing the cross section and the onset of doubling. (Noted that Equation (1) does not apply to period double.)

As illustrated in Figure 3.6 (b to d), the uniaxially aligned wrinkles also gradually disappeared with light irradiation, as was the case for the random labyrinth patterns. Figure 3.6 (f to i) show the amplitude change with illumination time. When irradiation was terminated and the bilayers were swelled in water, the erased patterns immediately became restored to the uniaxially aligned initial state.

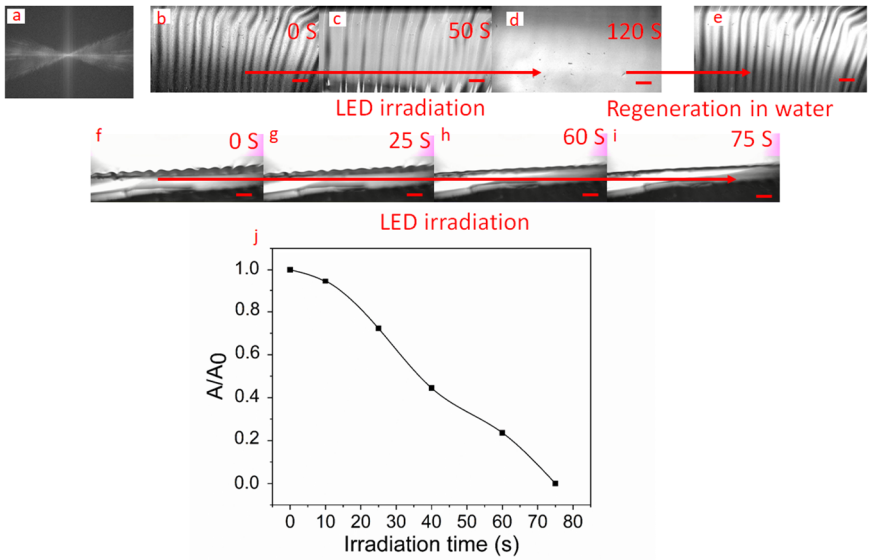

Figure 3.6 (**a**) Fast Fourier transform of a uniaxially aligned pattern indicating distance doubling of the pattern displayed in (**b**). (**b** to **d**) Formation and extinction of aligned patterns via swelling in water and light irradiation. Optical images (top view) of pattern disappearance via light irradiation. (**e**) Optical image of pattern formation after swelling in water. (**f** to **i**) Side view optical images of pattern disappearance triggered by light irradiation. (**j**) Amplitude variation as a function of light irradiation time. Scale bar, 400 µm.

3.2.2 Light diffusors

Periodic and rough surface microstructures can be applied to manufacture responsive optical devices by interacting with light and modulating the optical state via refraction and reflection. Since the wrinkling wavelength (400 μm for the random labyrinth patterns, 480 μm for the uniaxial patterns) of the bilayer hydrogels is much larger than the wavelength of visible light, the wrinkling bilayers can be used as optical diffusers to homogenize light, e.g., to prevent eye damage which may occur when viewing directly into a light source, or to achieve a soft illumination without sharp shadows. The light diffusion properties of the wrinkling surfaces were demonstrated by an experimental setup as shown in Figure 3.7a. The optical images of the transmitted laser spots on the screen are captured in Figure 3.7 (b to d).

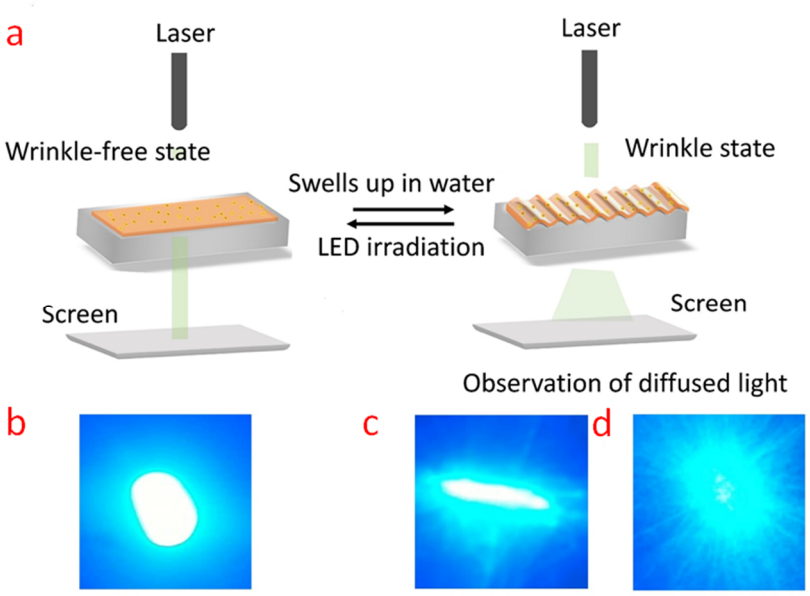

Figure 3.7 (**a**) Illustration of the light diffusing setup. Laser spots diffused through the wrinkled surfaces of (**b**) wrinkle-free surface, (**c**) uniaxially aligned patterning surface, (**d**) randomly oriented wrinkling surface.

Figure 3.7b shows the circular laser beam without diffusion effects when bilayer hydrogels are in the flat state. The laser beam is diffused unidirectionally for the

uniaxially aligned surface patterns as shown in Figure 3.7c, while the laser beam is diffused isotropically in case of a randomly oriented wrinkle surface (Figure 3.7d). Due to the multi-responsive, fully reversible features of the wrinkling surfaces, tunable diffusion can always be achieved with light being reverted to the original spot (Figure 3.7b) under high power LED irradiation.

3.3 Conclusions

In conclusion, hydrogel bilayers, possessing random and aligned wrinkling surfaces were developed. Wrinkle morphologies could be generated by exposure of the bilayer hydrogel to water and erased by irradiation of the surface morphologies with light, or thermal heating. Light responsiveness of these bilayers was realized by fabricating AuNPs in situ in the hydrogel top layer, which consequently could be addressed by rapid plasmonic heating. The fabricated wrinkling surfaces can be used as light diffusors that diffuse light anisotropically and isotropically.

3.4 Experimental Section

Materials: The cationic PFS polyelectrolyte, bearing methacrylamide side groups (Figure S3.1), was prepared according to a published procedure (Supporting information).[35] *N*-Isopropylacrylamide (NIPAM, Aldrich, 97%) was recrystallized twice from a toluene-hexane solution (50% v/v) and dried under vacuum prior to use. Acrylamide (AAm) (Aldrich, >99%), *N,N'*-methylenebisacrylamide (MBAm) (Aldrich, >99%), tetrachloroauric(III) acid trihydrate (Aldrich, >99.9%), sodium chloride (Aldrich, 99.5%) and methanol (Biosolve, AR) were used without further purification. Lithium phenyl-2,4,6-trimethylbenzoylphosphinate (LAP) was prepared according to an established procedure.[36] All water used in the experiments was Milli-Q grade.

Preparation of bilayer hydrogels: The PNIPAM-PFS pre-gel solution was prepared by mixing monomers in a mole ratio of PNIPAM: PFS: MBAm: Methanol = 100: 0.47: 3.2: 673. The AAm pre-gel solution was prepared by mixing monomers in a mole ratio of AAm: MBAm: H_2O = 100: 0.84: 1977. Bilayer hydrogels were fabricated in a two-step process (Figure S3.2). The PNIPAM-PFS pre-gel solution

was quickly injected into an assembled mould consisting of two glass plates separated by polyimide (Kapton) spacers (12 μm in thickness), then polymerized under ultraviolet irradiation (λ = 365 nm) for 5 min. The covering glass slide was lifted, PDMS spacers (7 mm in thickness) were added to replace the first ones, PAAm pre-gel solution was injected into the mould and covered by the glass slide again. The mixture was then irradiated under UV light (λ = 365 nm) for 15 min.

Fabrication of in-situ formed AuNPs in the hydrogel top layer Tetrachloroauric(III) acid trihydrate was dissolved in deionized water for a 1 mM solution. Then, the top layer of a bilayer hydrogel was covered with tetrachloroauric (III) acid trihydrate solution (1 mM). The color of the top layer turned from very light amber to pinkish.

Characterization: Surface patterns were imaged and their generation and erasure processes were recorded using an Olympus BX60 Microscope. The light source used for plasmonic heating of the bilayers was a high power LED (405 nm, 100W, Shenzhen kobee Technology Co., Ltd.), the laser used for light diffusing experiments was a laser pen (λ = 405 nm, 5 mW, AIBOULLY). UV-Vis spectra were measured with a TECAN Infinite 200 PRO instrument. Rheological experiments were carried out with an Anton Paar MCR-302 rheometer. Transmission Electron Microscopy (TEM) measurements were performed using a Philips CM300ST-FEG Transmission Electron Microscope, operated at 300 kV.

References

[1] Ebata, Y.; Croll, A. B.; Crosby, A. J. Wrinkling and Strain Localizations in Polymer Thin Films. *Soft Matter* **2012**, *8*, 9086–9091.

[2] Zeng, S.; Li, R.; Freire, S. G.; Garbellotto, V. M. M.; Huang, E. Y.; Smith, A. T.; Hu, C.; Tait, W. R. T.; Bian, Z.; Zheng, G.; Zhang, D.; Sun, L. Moisture-Responsive Wrinkling Surfaces with Tunable Dynamics. *Adv. Mater.* **2017**, *29*, 1–7.

[3] Chen, D.; Yoon, J.; Chandra, D.; Crosby, A. J.; Hayward, R. C. Stimuli-Responsive Buckling Mechanics of Polymer Films. *J. Polym. Sci. Part B Polym. Phys.* **2014**, *52*, 1441–1461.

[4] Chan, E. P.; Smith, E. J.; Hayward, R. C.; Crosby, A. J. Surface Wrinkles for Smart Adhesion. *Adv. Mater.* **2008**, *20*, 711–716.

[5] Wu, K.; Sun, Y.; Yuan, H.; Zhang, J.; Liu, G.; Sun, J. Harnessing Dynamic Wrinkling Surfaces for Smart Displays. *Nano Lett.* **2020**, *20*, 4129–4135.
[6] Chan, E. P.; Crosby, A. J. Fabricating Microlens Arrays by Surface Wrinkling. *Adv. Mater.* **2006**, *18*, 3238–3242.
[7] Yang, S.; Khare, K.; Lin, P. C. Harnessing Surface Wrinkle Patterns in Soft Matter. *Adv. Funct. Mater.* **2010**, *20*, 2550–2564.
[8] Wang, X.; Sperling, M.; Reifarth, M.; Böker, A. Shaping Metallic Nanolattices: Design by Microcontact Printing from Wrinkled Stamps. *Small* **2020**, *16*, 1–8.
[9] Khang, D. Y.; Rogers, J. A.; Lee, H. H. Mechanical Buckling: Mechanics, Metrology, and Stretchable Electronics. *Adv. Funct. Mater.* **2009**, *19*, 1526–1536.
[10] Ng, C. C. A.; Magenau, A.; Ngalim, S. H.; Ciampi, S.; Chockalingham, M.; Harper, J. B.; Gaus, K.; Gooding, J. J. Using an Electrical Potential to Reversibly Switch Surfaces between Two States for Dynamically Controlling Cell Adhesion. *Angew. Chemie - Int. Ed.* **2012**, *51*, 7706–7710.
[11] Tokudome, Y.; Kuniwaki, H.; Suzuki, K.; Carboni, D.; Poologasundarampillai, G.; Takahashi, M. Thermoresponsive Wrinkles on Hydrogels for Soft Actuators. *Adv. Mater. Interfaces.* **2016**, *3*, 1500802.
[12] Li, F.; Hou, H.; Yin, J.; Jiang, X. Near-Infrared Light–Responsive Dynamic Wrinkle Patterns. *Sci. Adv.* **2018**, *4*, 1–9.
[13] Zong, C.; Zhao, Y.; Ji, H.; Han, X.; Xie, J.; Wang, J.; Cao, Y.; Jiang, S.; Lu, C. Tuning and Erasing Surface Wrinkles by Reversible Visible-Light-Induced Photoisomerization. *Angew. Chemie - Int. Ed.* **2016**, *55*, 3931–3935.
[14] González-Henríquez, C. M.; Alfaro-Cerda, P. A.; Veliz-Silva, D. F.; Sarabia-Vallejos, M. A.; Terraza, C. A.; Rodriguez-Hernandez, J. Micro-Wrinkled Hydrogel Patterned Surfaces Using PH-Sensitive Monomers. *Appl. Surf. Sci.* **2018**, *457*, 902–913.
[15] Li, F.; Hou, H.; Yin, J.; Jiang, X. Multi-Responsive Wrinkling Patterns by the Photoswitchable Supramolecular Network. *ACS Macro Lett.* **2017**, *6*, 848–853.
[16] Ogurtani, O. T.; Senyildiz, D.; Cambaz Buke, G. Wrinkling of Graphene Because of the Thermal Expansion Mismatch between Graphene and Copper. *Surf. Interface Anal.* **2018**, *50*, 547–551.
[17] Zhou, Z.; Li, Y.; Guo, T. F.; Guo, X.; Tang, S. Surface Instability of Bilayer Hydrogel Subjected to Both Compression and Solvent Absorption. *Polymers (Basel).* **2018**, *8*, 1–15.
[18] Kim, H. S.; Crosby, A. J. Solvent-Responsive Surface via Wrinkling Instability. *Adv. Mater.* **2011**, *23*, 4188–4192.
[19] Rodríguez-Hernández, J. Wrinkled Interfaces: Taking Advantage of Surface Instabilities to Pattern Polymer Surfaces. *Prog. Polym. Sci.* **2015**, *42*, 1–41.
[20] Li, T.; Hu, K.; Ma, X.; Zhang, W.; Yin, J.; Jiang, X. Hierarchical 3D Patterns with Dynamic Wrinkles Produced by a Photocontrolled Diels–Alder Reaction on the Surface. *Adv. Mater.* **2020**, *32*, 1–8.

[21] Hailes, R. L. N.; Oliver, A. M.; Gwyther, J.; Whittell, G. R.; Manners, I. Polyferrocenylsilanes: Synthesis, Properties, and Applications. *Chem. Soc. Rev.* **2016**, *45*, 5358–5407.
[22] Feng, X.; Hempenius, M. A.; Vancso, G. J. Metal Nanoparticle Foundry with Redox Responsive Hydrogels. *Macromol. Chem. Phys.* **2018**, *219*, 1–7.
[23] Feng, X.; Zhang, K.; Chen, P.; Sui, X.; Hempenius, M. A.; Liedberg, B.; Vancso, G. J. Highly Swellable, Dual-Responsive Hydrogels Based on PNIPAM and Redox Active Poly(Ferrocenylsilane) Poly(Ionic Liquid)s: Synthesis, Structure, and Properties. *Macromol. Rapid Commun.* **2016**, *37*, 1939–1944.
[24] Sui, X.; Feng, X.; Hempenius, M. A.; Vancso, G. J. Redox Active Gels: Synthesis, Structures and Applications. *J. Mater. Chem. B* **2013**, *1*, 1658–1672.
[25] Shi, Q.; Xia, H.; Li, P.; Wang, Y. S.; Wang, L.; Li, S. X.; Wang, G.; Lv, C.; Niu, L. G.; Sun, H. B. Photothermal Surface Plasmon Resonance and Interband Transition-Enhanced Nanocomposite Hydrogel Actuators with Hand-Like Dynamic Manipulation. *Adv. Opt. Mater.* **2017**, *5*, 1–9.
[26] Yan, H.; Tsujii, K. Potential Application of Poly(N-Isopropylacrylamide) Gel Containing Polymeric Micelles to Drug Delivery Systems. *Colloids Surfaces B: Biointerfaces* **2005**, *46*, 142–146.
[27] Chung, J. E.; Yokoyama, M.; Yamato, M.; Aoyagi, T.; Sakurai, Y.; Okano, T. Thermo-Responsive Drug Delivery from Polymeric Micelles Constructed Using Block Copolymers of Poly(N-Isopropylacrylamide) and Poly(Butylmethacrylate). *J. Control. Release* **1999**, *62*, 115–127.
[28] Antunes, F. E.; Gentile, L.; Tavano, L.; Rossi, C. O. Rheological Characterization of the Thermal Gelation of Poly(N-Isopropylacrylamide) and Poly(N-Isopropylacrylamide) Co-Acrylic Acid. *Appl. Rheol.* **2009**, *19*, 3–5.
[29] Breid, D.; Crosby, A. J. Effect of Stress State on Wrinkle Morphology. *Soft Matter* **2011**, *7*, 4490–4496.
[30] Chan, E. P.; Crosby, A. J. Spontaneous Formation of Stable Aligned Wrinkling Patterns. *Soft Matter* **2006**, *2*, 324–328.
[31] Whitesides, G. M. Spontaneous Formation of Ordered Structures in Thin. *Nature* **1998**, *393*, 0–3.
[32] Tokudome, Y.; Kuniwaki, H.; Suzuki, K.; Carboni, D.; Poologasundarampillai, G.; Takahashi, M. Thermoresponsive Wrinkles on Hydrogels for Soft Actuators. *Adv. Mater. Interfaces* **2016**, *3*, 1500802–1500807.
[33] Ohzono, T.; Watanabe, H.; Vendamme, R.; Kamaga, C.; Kunitake, T.; Ishihara, T.; Shimomura, M. Spatial Forcing of Self-Organized Microwrinkles by Periodic Nanopatterns. *Adv. Mater.* **2007**, *19*, 3229–3232.
[34] Khang, D.-Y.; Jiang, H.; Huang, Y.; Rogers, J. A. A stretchable form of single-crystal silicon for high-performance electronics on rubber substrates. *Science* **2006**, *311*, 208–212.

[35] Zhang, K.; Feng, X.; Ye, C.; Hempenius, M. A.; Vancso, G. J. Hydrogels with a Memory: Dual-Responsive, Organometallic Poly(Ionic Liquid)s with Hysteretic Volume-Phase Transition. *J. Am. Chem. Soc.* **2017**, *139*, 10029–10035.

[36] Mingot-Castellano, M. E.; Diaz-Canales, D.; Fernandez-Fuertes, F.; Perera-Alvarez, M.; Caparros-Miranda, I.; Jimenez-Barcenas, R.; Palomo-Bravo, A.; Heiniger Mazo, A. I.; ACC, G. Thrombopoietin Analogs In ITP Patients Daily Practice: Treatment Profile, Efficacy and Safety. *Blood* 2013, 122, 4749–4749.

3.5 Supporting Information

Preparation of the PFS bearing methacrylamide cationic side groups: The cationic PFS polyelectrolyte, bearing methacrylamide side groups (Figure S3.1), was prepared according to a published procedure.[35] N-[3-(Dimethylamino)propyl]methacrylamide (1 mL, 8.3 mmol) was added to a solution of Poly(ferrocenyl(3-iodopropyl)methylsilane) (0.50 g, 1.26 mmol) in THF (8 mL) and DMSO (4 mL). The reaction mixture was subsequently stirred at room temperature for 24 h. THF was then removed by a N_2 flow, transferred to a Spectra/Pro 4 dialysis hose (MWCO 12-14,000 g mol^{-1}), and dialyzed against 0.1 M NaCl (3 × 1 L) and Milli-Q water (3 × 1 L). Final orange flakes product was obtained by drying the salt free solution with a flow of N_2 (0.6g, 100%)

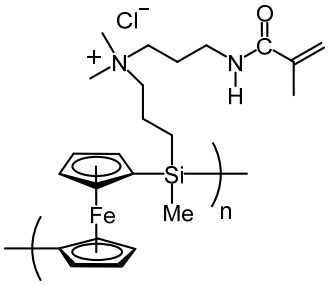

Figure S3.1 Structure of the crosslinkable PFS polycation.

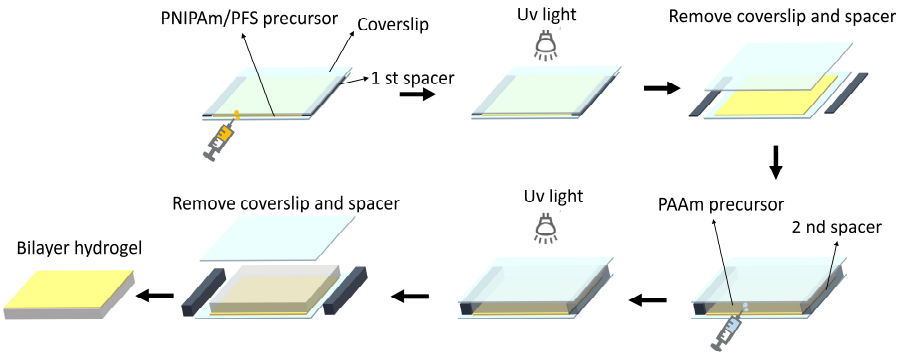

Figure S3.2 Fabrication process of the bilayer hydrogels.

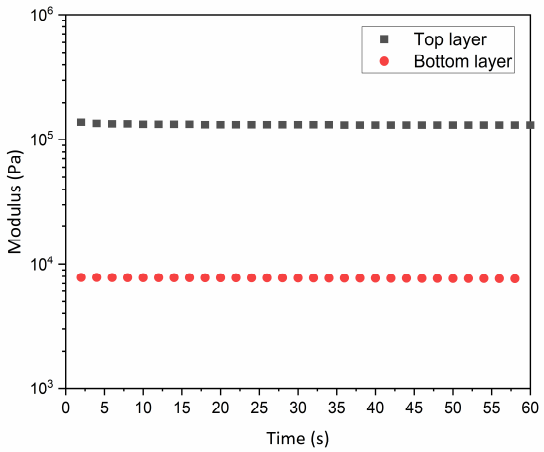

Figure S3.3 Storage moduli of the hydrogel top layer (with AuNPs) and of the hydrogel bottom layer.

To enhance the visibilities, we prepared we prepared surface plot images by using ImageJ function.

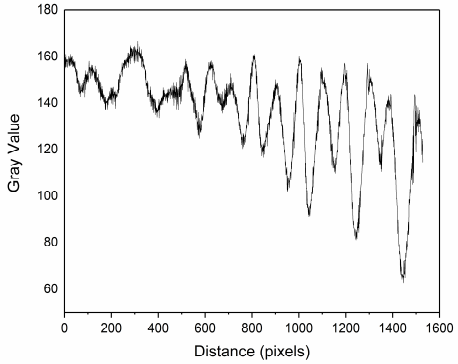

Figure S3.4. Profile plot of the aligned patterns.

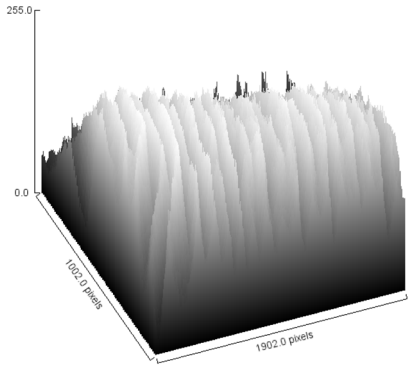

Figure S3.5. Surface plot of the aligned patterns.

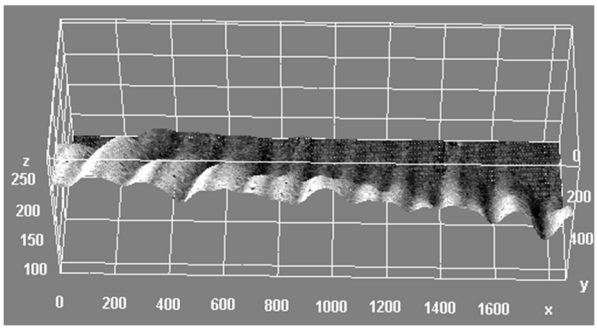

Figure S3.6. 3D surface plot image of the aligned patterns.

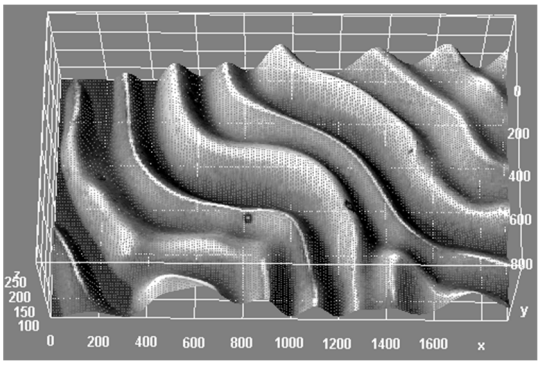

Figure S3.7. 3D Surface plot image of the aligned patterns.

3

Chapter 4

Dynamic Evolution of Surface Patterns on Light-Responsive Bilayer Hydrogels

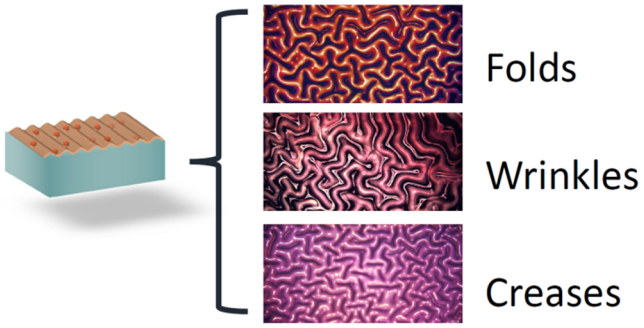

The swelling of hydrogels can generate large compressive stresses at their surfaces. Bilayer hydrogels comprised of a thin top layer and thick bottom layer with different swelling ratio and rigidity develop various surface patterns upon swelling in water. Here in this Chapter, we synthesized a series of bilayer hydrogels using AuNP nanocomposite PNIPAM/PFS hydrogel films with different crosslink densities as top layers and PAAm hydrogels with different crosslink densities as bottom layers. As the top layer swelled in water, patterns like creases, folds and wrinkles developed at the surfaces. The patterns were then decompressed by swelling up the bottom layer to different degrees, accompanied by the evolution of morphologies such as Y shape folds to I shape folds to flat surface transitions, aligned wrinkles to weave-like wrinkles transitions, and jog angle changes in herringbone wrinkling patterns.

Contents of this Chapter will be published as: Jinmeng Hao, Mark A. Hempenius, G. Julius Vancso, Dynamic Evolution of Surface Patterns on Light-Responsive Bilayer Hydrogels, *To be submitted*.

4.1 Introduction

A bilayer system with a thin rigid film attached to a compliant thick substrate spontaneously generates wrinkling patterns when mismatch-induced in-plane compressive strains exceed a critical value.[1] Wrinkles are a periodic sinusoidal deformation that form at a small strain. As the strain increases beyond a critical value, the wrinkles double their period, which leads to deep folds.[2] Wrinkles have been extensively studied theoretically[3–6] and experimentally[7–12] as they have shown potential as useful surface patterns in diverse applications such as patterned templates,[9,13,14] cell alignment,[15] tunable optics,[16–18] flexible electronics,[19,20] metrology,[21] microfluidic,[22,23] and dynamic displays.[18,24,25]

To meet the requirements for different applications, it is essential to be able to tune basic characteristics of wrinkles including wavelength, amplitude, direction and location.[12] For example, oriented growth of cells can be achieved through the use of aligned wrinkle patterns.[26] Water can be transported through specific arrangements in the orientation (θ) and location of ridges on leaves and insects.[27] Wrinkling morphologies can be controlled by regulating the applied strain and changing material properties of films and substrates. The applied strain can be adjusted by prestrain relaxation,[22,28,29] thermal shrinkage,[24] swelling[16,30–34] and externally imposed stimuli.[9,25,35] For example, Sun,[36] Zhao[1], and Yang[33] reported a series of wrinkling systems which were tuned by the release and application of prestrain. Burdick[5,32,37], Sun[16] and Jiang[4] incorporated smart materials in osmotically and thermally driven wrinkling systems and developed thermal, light and moisture responsive dynamic wrinkles.

Different loading conditions can be achieved with changing the relative strain in the planar directions and the top layer can buckle into various two-dimensional wrinkling patterns such as triangular, herringbone, stripes, checkerboards, hexagonal, and labyrinth structures.[36,38–40] Labyrinth patterns emerge when the compressive stress remains perfectly equi-biaxial throughout the wrinkle formation process, while the herringbone pattern occurs when the applied stress at the critical buckling point is non-equi-biaxial, even if the final stress is equi-biaxial.[33] The jog angle (θ) in the herringbone pattern also changes with the relative strain in the planar directions.[33] In experiments, the formation and transition of these wrinkling patterns greatly depend

on the strain state and the loading sequence of the strain. With mismatch in compressive strain further increasing, wrinkles become unstable and evolve into new morphological phases such as folding, period-double, ridges, cracks or delamination depending on the magnitude of applied strain and elastic nature of the substrate.[41] The transition of wrinkles developing into other morphologies is crucial for biological systems, such as the formation of villi in human and chick gut, wherein the mesenchyme and attached epithelium first fold into longitudinal ridges, then a herringbone pattern, and finally into individual villi.[42] Wang and Zhao constructed a quantitative phase diagram that can predict the formation and evolution of various types of surface patterns based on the geometrical variations and moduli mismatches.[41] However, film-substrate systems with systematically varied mechanical properties have never been reported.

In this Chapter, harnessing swelling induced instability, surface patterns with controlled morphology, order, size and complexity were produced in a bilayer hydrogel system. A series of bilayer hydrogels consisting of poly(acrylamide) (PAAm) hydrogel substrates with different crosslink densities and thin poly(*N*-isopropylacrylamide) (PNIPAM) hydrogels were fabricated. In-situ synthesized gold nanoparticles (AuNPs) were introduced in the PNIPAM top layer, using redox responsive poly(ferrocenylsilane) chains incorporated in the PNIPAM hydrogel layer to turn added $HAuCl_4$ salts into AuNPs.[43–45] Bilayers with different dimensions were developed to realize controllable formation/relaxation of the local anisotropic stress state and thus create elaborate wrinkling patterns. The applied strain could be controlled by fast swelling and deswelling of the thin top layer which led to pattern formation and disappearance. The PNIPAM top layer containing in-situ fabricated Au nanoparticles allowed plasmonic heating of this layer by irradiation with light. The top layer could be flattened by irradiation with light or thermal heating. By swelling the bottom layers for different periods of time, patterns with complex features were fabricated through the decrease of the compressive strain to different degrees, which induced the decompression of the patterns to different extents. Particularly, dynamic evolution of surface patterns including the formation of sulcal folding patterns, stripes to weave-like patterns, change of jog angle in herringbone patterns, Y shape folds to I shape folds to flat surface transitions were observed and studied by decompressing in water for different periods of time.

4.2 Results and Discussion

4.2.1 The fabrication of patterns

The fabrication of light-responsive patterns is illustrated in Chapter 3 Figure 3.1. The bilayers comprising AuNP nanocomposite PNIPAM/PFS hydrogel as top layer and PAAm as bottom layer were made by a stepwise process. The hydrogel top layer was fabricated from a UV-curable precursor solution composed of NIPAM, a PFS polycation with a crosslinkable methacrylamide group in each repeat unit, photoinitiator LAP and crosslinker MBAm. The precursor solution was polymerized under UV irradiation in an assembled mold with a 12 μm spacer. Subsequently, the bottom layer hydrogel precursor composed of AAm, LAP and MBAm was then added to the mold, now featuring a much thicker spacer, and crosslinked with UV irradiation. AuNPs and patterns were formed simultaneously while swelling the hydrogel top layer in 1 mM tetrachloroauric(III) acid trihydrate solution. Due to the presence of PFS chains which possess skeletal ferrocene redox centers, AuNPs were formed in-situ in the top layer by direct reduction as the layer swelled in the $HAuCl_4$ solution.[44,46] Nanoparticle formation was accompanied by a color change from very light amber to pinkish within a few seconds. When the top layer swelled up, the generated osmotic stress exceeded the critical stress for buckling. As a result, patterns (folds, creases and wrinkles) developed to reduce the energy of the bilayer system.

As it is well known that the moduli of hydrogels depend on the cross-linking density, which can be controlled by simply varying the crosslinker concentration, surface patterns with controlled order and periodicity were generated. Three top layers (T1-T3) with different MBAm concentrations were used against five PAAm bottom layers (B1-B5) with different MBAm concentrations, which separately allowed the tuning of the morphologies and pattern wavelength. Fifteen samples with varied patterns of different wavelengths are shown in Figure 4.1. According to the buckling theory, the wavelength, λ, of the patterns is correlated to the thickness of the top layer, h, and the top layer to bottom substrate modulus ratio as described in Equation (1).[25,37]

$$\lambda = 2\pi h \left(\frac{\bar{E}_f}{3E_s}\right)^{1/3} \qquad (1)$$

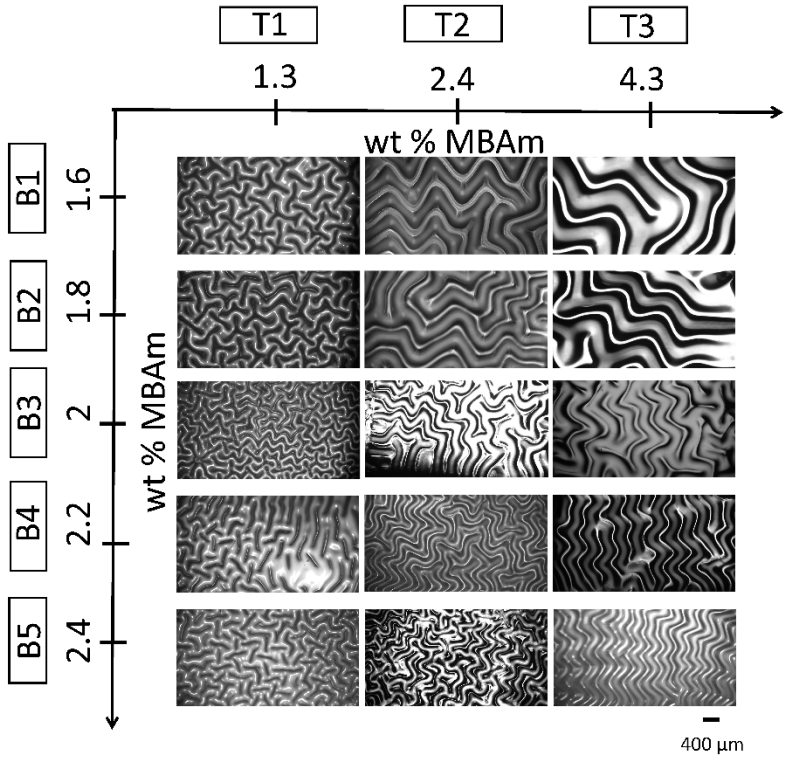

Figure 4.1 Optical microscopy (OM) images of patterns on bilayer surfaces with different wavelengths; T1-T3 represent top layer hydrogels and B1-B5 represent bottom layer hydrogels, with MBAm content increasing.

In these bilayer hydrogels, top layer films were swelled up to a thickness of 28–33 µm. With the same top layers, the wavelength of the patterns decreases as the bottom layer becomes more rigid (with the MBAm concentration increasing) which confirms with Equation (1). Bilayers with T2 as top layers are taken as an example, a quantitative comparison between experimental wavelength and theoretical wavelength is found, as shown in Figure 4.2.

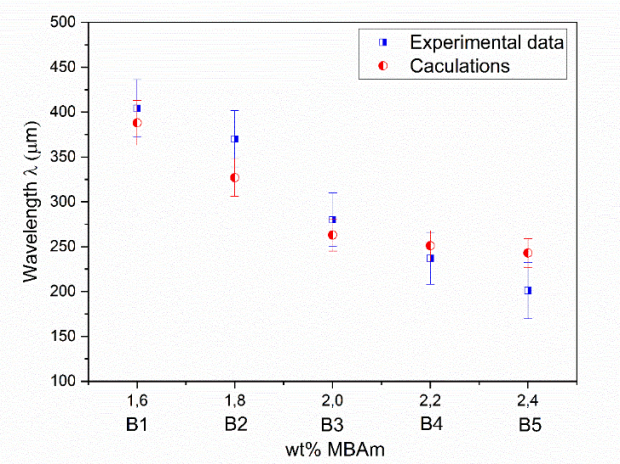

Figure 4.2 A quantitative comparison between experimental wavelength and theoretical wavelength values for wrinkled surfaces on bilayers with T2 as top layers. Calculations are based on Equation (1).

Although the driving force for patterns like folding, creasing and wrinkling is the same, the three modes of instability occur at very different critical strains.[41] When the compressed strain reaches the critical values, patterns can initiate and transit into others. For a compliant substrate with a stiff thin top layer, a compression exceeding a critical value generates wrinkles while a further increased compression will turn wrinkles into folds. For a relatively soft top layer, compression directly results in crease formation without forming wrinkles first. It must be noted that the folding tip is open because of the bending rigidity of the stiff top layer, while the crease tip is sharp. The type of instability mode depends on the compressive strain and modulus ratio of the top layer and the substrate layer.[41]

Here, the swelling degree of the top layer, which determines the magnitude of the compressive strain, depends on the gel composition and degree of crosslinking. Briefly, for bilayer hydrogels, the larger the swelling degree of the top layer is, the higher the compressive strain is. The swelling degree decreases with increasing MBAm concentration, which means the compressive strain applied by top layer T1 is larger than T2 and T3. With the same bottom layer, clear transitions from folds and creases to wrinkles are observed as the MBAm concentration in the top layer increases from 1.3 wt% (T1) to 4.3 wt% (T3). Furthermore, folding and creasing patterns (higher critical strain) only exist in bilayers with T1 as top layer while

samples with T2 and T3 top layers exhibited wrinkling patterns (lower critical strain) instead. And for bilayers with T1 as top layer, patterns transited from folds (T1B1, T1B2 and T1B3) to creases (T1B4, T1B5) when the MBAm concentration in the bottom substrate was higher than 2.2 wt%.

A phase diagram has been developed in previous theoretical studies and simulations to predict the formation and evolution of the instability patterns as a function of applied strain and film-substrate modulus ratio have been established.[43] Figure 4.3 presents a typical phase diagram which also includes our experimental data. The results are in agreement with previous simulations.[47] According to previous reports, creasing patterns initiate at the critical strain 0.396. For samples T1B4 and T1B5, the applied strain is around 0.53 (determined by the change in width of the top layer before and after swelling), indicating that swelling can be expected to induce creasing pattern formation. The shear modulus ratio, μ_f / μ_s (μ_f is shear modulus of the top layer film, μ_s is shear modulus of the substrate hydrogel), however, also plays a role in determining the type of pattern that is finally obtained. For T1B4 and T1B5, the shear modulus ratio lies around 2.6 and 3.1, respectively. These values also support creasing pattern formation (Figure 4.3).[43]

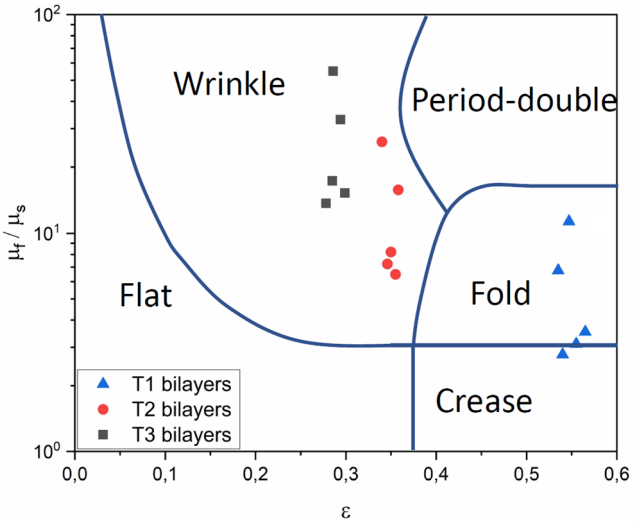

Figure 4.3 A phase diagram of four types of instability patterns determined by the applied strain ε, and also by the modulus ratio μ_f / μ_s. Experimental data of the 15 samples are shown in the diagram. The theoretical phase diagram is established in reference.[41]

For samples with the same shear modulus ratio but a larger applied strain, the surfaces are initially flat, then form creases, and finally become flat again with the creases disappearing completely. For samples T1B1 to T1B3 which were subjected to the same strain (0.53) but higher shear modulus ratio, folding patterns formed instead of creases. Note that the strain applied on the same sample is not always equal because of surface defects and boundaries. The pattern morphology was attributed to the competition between osmotic stress and lateral confinement within the bilayer gel. In general, the swelling-induced osmotic strain may not necessarily remain equi-biaxial during the formation process, especially at the critical point where buckling is initiated. It is also worth noting that the compressive stress induced by swelling can be large enough to exceed the interfacial adhesion forces between the top layer and the bottom substrate, causing bilayer hydrogel delamination.

4.2.2 Evolution of patterns with decompressing

In sample T1B1, three dimensional sulcal folding patterns can be observed. The generation of these patterns is due to the high isotropic compression induced by the highly swollen hydrogel top layer T1. Sulci-like folding patterns are often seen in tissues like primate brain,[48] with the cerebellum showing striped patterns and the cortex showing triple junctions that are similar to those seen in the experiments listed in Figure 4.1. In the T1B1 sample, the fully swollen top layer already showed a dense pattern of Y-shaped triple junctions of folds on an approximately triangular lattice. The Y-shaped folds showed a threefold symmetry with an angle of 120^{o}; while some Y-shaped folds were connected with neighboring junctions, most of them were independent.

When PAAm hydrogel is immersed in water, its modulus decreases as solvent diffuses through the bottom layer with time.[49] For the soft gels, a substantial decrease in elastic modulus can be attained while for stiff gels such as our top layer in hydrogel T1B1, the modulus changed negligibly with time. The variation of modulus values is expected to change the pattern appearance.

Figure 4.4 shows the degree of swelling of both layers for sample T1B1 at room temperature, as a function of time. When the bottom layer swelled up, decompression took place gradually over time while preserving the isotropic strain. Y-shaped folds gradually transformed to I-shaped folds as shown in Figure 4.5. When T1B1 swelled in water for 4 h, the applied strain was reduced from 0.53 to 0.40, where both Y and

I-shaped folds existed (Figure 4.5b), while all Y-shaped folds were turned into I-shaped folds at a strain of about 0.35 (Figure 4.5c). Interestingly, most formed I-shaped folds are perpendicular to their adjacent ones, which indicates that the Y-shaped folds relaxed mostly in their perpendicular directions. According to previous investigations,[50] perfect symmetric Y-shaped surface patterns are based on a hexagonal lattice while I-shaped patterns are based on a square lattice with alternating orientations. With further decompressing (swelling of the bottom layer), I-shaped folds gradually become dominant in minimizing energy. With the bottom layer swelling more, I-shaped folds shortened and finally disappeared when the strain was almost completely released by unfolding (Figure 4.5d). To express these findings in a phase diagram (Figure 4.3), as μ_s decreases with swelling, the applied strain ε and the modulus ratio μ_f / μ_s increase and if at the same time the applied strain decreases, the patterns transform from folds to flat surfaces. T1B2 also shows a very similar way of pattern changing as T1B1, while for sample T1B3, the formed folding patterns did not disappear in the end (Supporting Information, Figure S4.1) due to a relatively rigid bottom layer that keeps the compressive strain at 0.19, which is above the critical strain of 0.14 and a μ_f / μ_s value of 5 which means the pattern transits from folds to wrinkled structures, as predicted by the phase diagram.

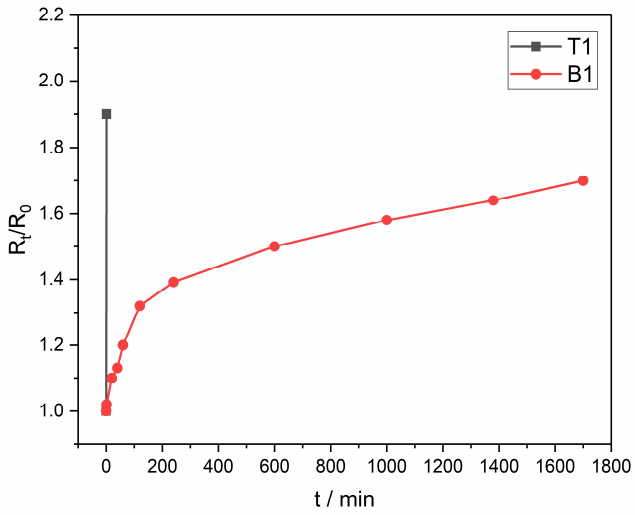

Figure 4.4 Degree of swelling verses time at RT for T1B1. The length at t min (R_t) is normalized by the initial length (R_0).

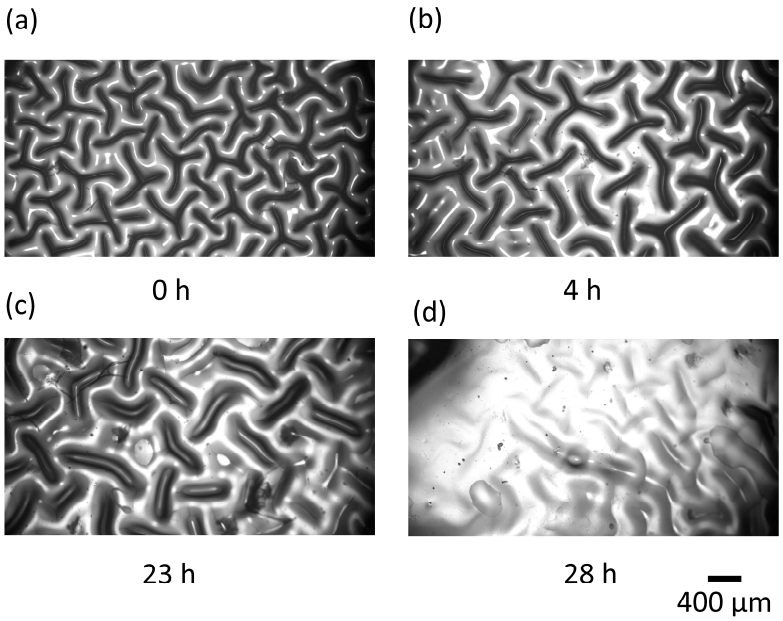

Figure 4.5 Optical microscopy images of surface patterns on sample T1B1 taken at four characteristic points while immersing in water from 0 to 28 h.

In comparison, sample T2B3 which bears both a more rigid top and bottom layer, shows a different pattern changing path when swelling up in water (Figure 4.6). Wrinkles with a wavelength around 280 μm first developed on the T2B3 surface. Based on Equation (1), as E_S decreases with the swelling of the bottom layer, λ increased to 391 μm in the fully swollen state and the amplitude decreased. Although morphologies changed in amplitude and periodic length, the wrinkling orders and shapes were barely changed because decompression developed isotropically. During the whole swelling process, the μ_f / μ_s ratio and applied strain-determined patterns all formed in the wrinkling instability area. Interestingly, patterns on samples with B1 as bottom layers can fully disappear when the swollen bottom layers decompress the compressive strain to a value below critical strain.

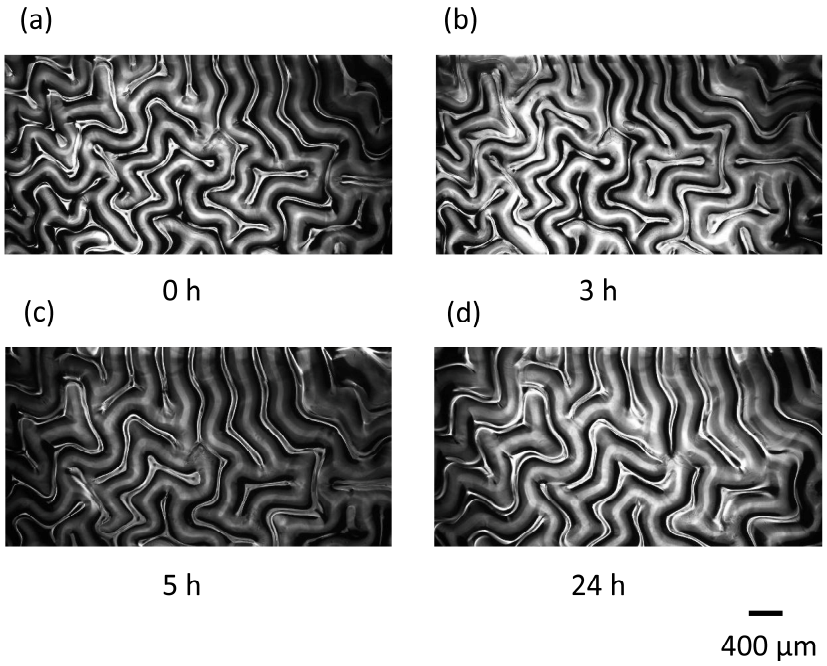

Figure 4.6 Optical microscopy images of surface patterns on sample T2B3 taken at four characteristic points while immersing in water from 0 to 24 h.

When osmotic strain is applied to semi-infinite bilayers, disorganized labyrinth wrinkle patterns[19,51] are produced as the compression is applied equi-biaxially in both directions simultaneously, so driving forces that orient the buckles are absent.[52] For bilayer hydrogel objects with defined dimensions, however, the bilayer edge containing the boundary between the hard and the soft layer dictates the stress distribution. As shown in Figure 4.7, *x* and *y* are taken as in-plane coordinates, the length of the bilayer is denoted by *L*, and the width is represented by W. To regulate boundary conditions, bilayers with three different dimensions were fabricated. Typical labyrinth wrinkle patterns like T2B1, T2B3 and T2B5 in Figure 4.1 were produced with L=2 cm and W=2 cm (Figure 4.7a), dimensions that can be considered to correspond with semi-infinite bilayers. At this size scale, boundary effects are minimal, with the sample being large enough to accommodate equilibrium equi-biaxial buckling patterns some distance away from the edge. The non-equi-biaxial stress would be the highest at the edge of the sample. Two T3B3 samples were made with two different dimensions. Figure 4.8a shows T3B3 with L=2 cm and W=0.5 cm

(Figure 4.7b). With long edges in the y-direction, the initial osmotic stress can relax along the x-direction at the soft boundary by local deformation of the substrate; therefore, the compressive stress developed in the y-direction is larger than in the x-direction and a uniaxial wrinkle pattern is formed perpendicular to the long axis.

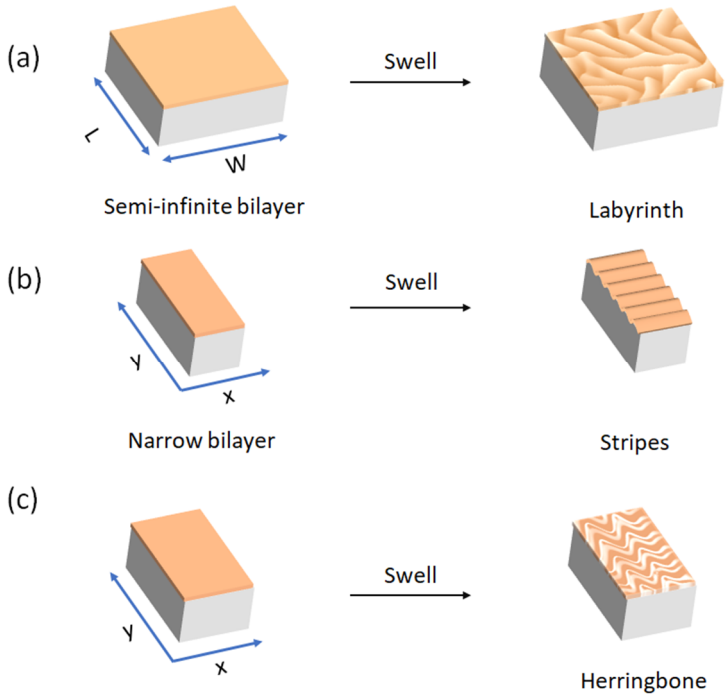

Figure 4.7 Schematic of the formation of responsive wrinkle patterns with changing bilayer dimensions

Interestingly, a weave like pattern showed up during the decompressing process as shown in Figure 4.8b and Figure 4.8c. These patterns are characterized by backbone-like ridges with perpendicular "cuts" protruding from the spines, which interlock with each other. The formation of the well-ordered weave-like patterns depends on the well-aligned stripe wrinkles. Similar like Y-shaped folds relax mostly in their perpendicular directions, we assume the stripes also tend to get decompressed in the perpendicular directions. It is assumed that the uniaxial wrinkles on the top

layer constrained the bottom layer's swelling in the direction parallel to the stripe alignment in the early swelling stage. Thus, the one-directional swelling of the bottom layer which occurs perpendicular to the stripes, induced a compressive strain in the direction parallel to the stripe alignment due to Poisson's effects.[53] The bilayers experienced a compressive strain that turned stripe patterns into a weave-like pattern at the surface. This long-range ordered orthogonal periodic weave-like patterns are kinetically trapped structures that will gradually disappear when the swelling degree in the bottom layer becomes large enough to unfold the weave-like wrinkles in both directions (Figure 4.8d).

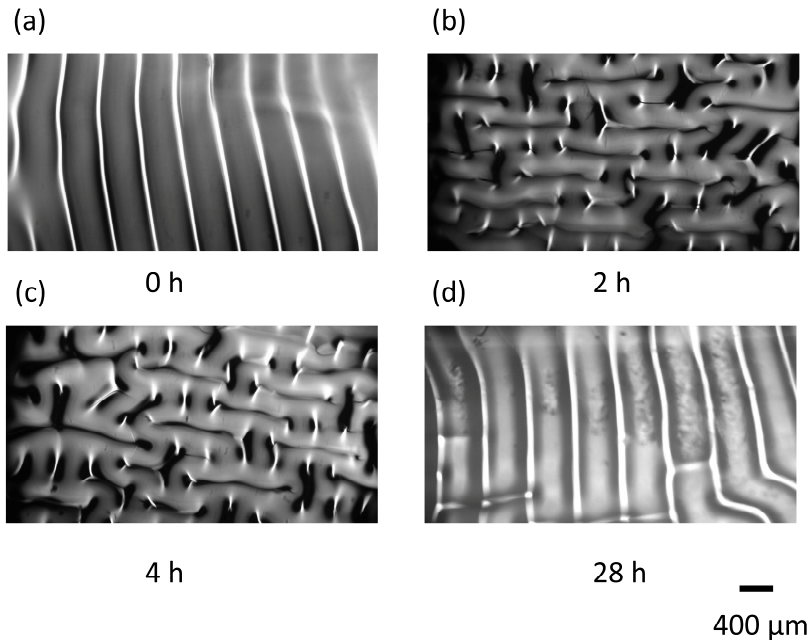

Figure 4.8 Optical microscopy images of surface patterns on sample T3B3 taken at four characteristic points while immersing in water from 0 to 28 h.

Figure 4.9 shows T3B3 with L=2 cm and W=1 cm (Figure 4.7c). As seen from Figure 4.9a, before the top layer becomes fully swollen, uniaxial wrinkles were formed just like in Figure 4.8a. When the continuous swelling exceeds the critical expansion of the *x*-direction, the residual stress in the x-direction is released by

forming herringbone wrinkles (Figure 4.9b). The jog angle of the herringbone turning of an equi-biaxially stretched, sequentially released sample is always around 90°.[54]

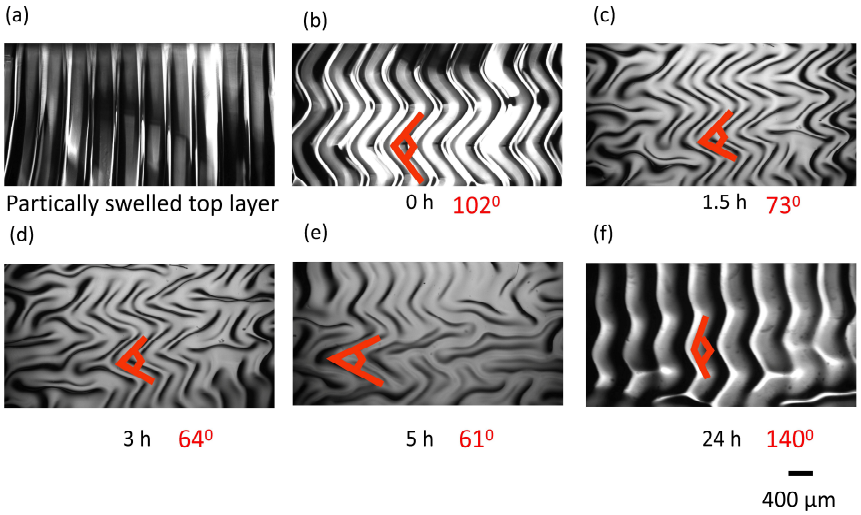

Figure 4.9 Optical microscopy images of surface patterns on sample T3B3 taken at four characteristic points while immersing in water from 0 to 24 h.

When the applied strain is not equi-biaxial, it is possible to tune the jog angle to different degrees in a herringbone pattern. For similar reasons as for weave-like pattern evolution, T3B3 developed a tunable jog angle in the herringbone structure. After the bottom layer swelled in water, the herringbone jog angle gradually decreased from 102° to 61° with swelling time, in response to the compressive strain increasing in a direction that is parallel to the stripes. When the bottom layer was fully swollen, the jog angle turned back to 140° instead of 102° because the rather rigid bottom layer did not fully decompress the patterns.

4.2.3 Light-responsive behavior

PNIPAM hydrogel as a typical temperature-responsive hydrogel shrinks at a temperature above a lower critical solution temperature (LCST) of around 32 °C whereas PAAm hydrogel shows no substantial volume change with temperature.[55] Since 25 nm sized plasmonic AuNPs are well dispersed in the PNIPAM hydrogel matrix, with light illumination at wavelengths that coincide with the NPs absorption,

AuNPs intensively absorb light and rapidly convert this into heat. This efficient process, which is based on localized surface plasmon resonances and intrinsic interband transitions,[56] allows one to raise the temperature of PNIPAM hydrogels above the LCST. In our experiments, a high-power LED with a wavelength of λ = 405 nm was used as a light source, and wrinkle patterns gradually disappeared after irradiation for 120 s as illustrated in Figure 4.10. With the top layer undergoing a significant size reduction, the applied strain was reduced down to zero which totally erased the patterns. For comparison, without light irradiation, wrinkles disappeared at a much slower speed, taking around 1 h. Bilayer surfaces can change from a patterned state to a pattern-free state rapidly and reversibly with light illumination and reswelling in water for multiple times.

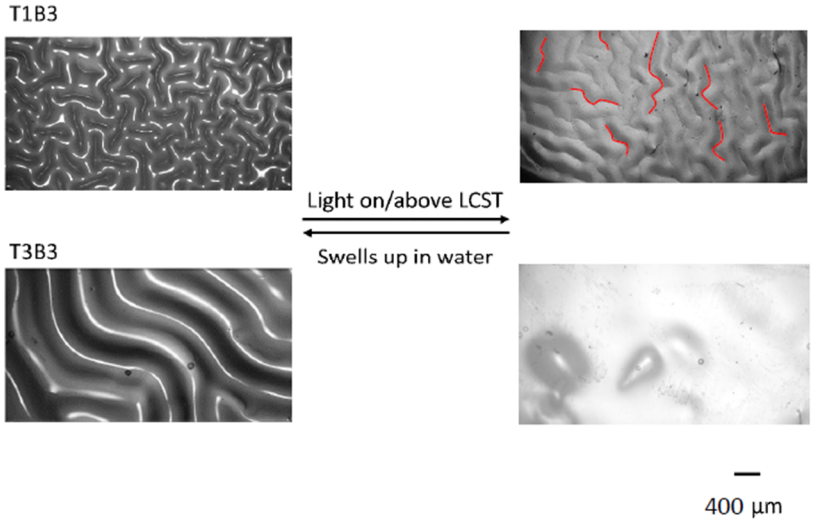

Figure 4.10 Optical microscopy images of surface patterns on sample T1B3 and T3B3 formation and disappearance behavior via swelling up in water and light irradiation. Part of the cracks are indicated with red lines.

Interestingly, compared with the T2 and T3 samples that show patterns which appear and disappear with complete reversibility with light stimuli and swelling in water, samples with T1 as top layer (T1B1 to T1B3) exhibited localized closed cracks after folding patterns disappeared due to illumination (Figure 4.10). Even if the folds disappeared, the cracks remained. Cracking always accompanied the folding in these samples. The cracking occurred because the compressive stress exceeded the bonding

strength between the top layer and the bottom substrate. Samples subjected to higher compressive stress which exceeds the interfacial adhesion forces will lead to delamination in the end.

4.3 Conclusions

In this Chapter, we presented the fabrication and evolution of light-responsive patterns (creases, folds and wrinkles) on bilayer hydrogels with controlled morphology, order, size, and complexity comprising AuNP nanocomposite PNIPAM/PFS hydrogels with different crosslink densities as top layers and PAAm with different crosslink densities as bottom layers. The dynamic evolution of surface instability was investigated and experimental observations of patterns throughout a range of applied strains were presented.

The wavelength of the wrinkles can be systematically controlled by changing the mechanical properties of the bilayers through changing crosslink densities. By changing bilayer dimensions, labyrinth, stripe and herringbone patterns were produced. Patterns can be decompressed by swelling the bottom layer, accompanied by the evolution of several different non-equilibrium morphologies. Y-shaped folds can gradually transform into I-shaped folds and finally vanish during the decompression process. Stripes transform to weave-like patterns which are kinetically trapped structures that finally disappear. The jog angles of the herringbone patterns can be tuned by swelling the bottom layer in water for different periods of time.

Our study demonstrates that various types of ordered patterns and their delicate geometrical features can be tuned in a bilayer hydrogel system. The versatile approach can be potentially useful for various bilayers to create complex patterns which can be applied in diverse applications, including tunable optical devices, tissue engineering, and sensors. These findings will also offer new insights for further theoretical studies of the instability mechanism.

4.4 Experimental Section

Materials: The cationic PFS polyelectrolyte, bearing methacrylamide side groups was prepared according to a published procedure.[57] *N*-Isopropylacrylamide (NIPAM,

Aldrich, 97%) was recrystallized twice from a toluene-hexane solution (50% v/v) and dried under vacuum prior to use. Acrylamide (AAm) (Aldrich, >99%), *N,N'*-methylenebisacrylamide (MBAm) (Aldrich, >99%), sodium chloride (Aldrich, 99.5%), methanol (Biosolve), and tetrachloroauric(III) acid trihydrate (Aldrich, > 99.9%) were used without further purification. Lithium phenyl-2,4,6-trimethylbenzoylphosphinate (LAP) was prepared according to established procedures.[58] All water used in the experiments was Milli-Q grade.

Preparation of Bilayer Hydrogels: The PNIPAM-PFS pre-gel solution was prepared by dissolving NIPAM monomers with LAP (1 wt%), PFS (2 wt%), MBAm (**T1** 1.3 wt%, **T2** 2.4 wt%, **T3** 4.3 wt%) in methanol. The AAm pre-gel solution was prepared by dissolving AAM monomers with LAP (1 wt%), MBAm (**B1** 1.6 wt%, **B2** 1.8 wt%, **B3** 2 wt%, **B4** 2.2 wt%, **B5** 2.4 wt%) in a mixture of water and methanol with a ratio of 6:1. Bilayer hydrogels were fabricated in a two-step process. The PNIPAM-PFS pre-gel solution was quickly injected into an assembled mold consisting of two glass plates separated by polyimide (Kapton) spacers (12 μm in thickness), then polymerized under ultraviolet irradiation (λ = 365 nm) for 5 min. The covering glass slide was lifted, PDMS spacers (7 mm in thickness) were added to replace the first ones, PAAm pre-gel solution was injected into the mold and covered by the glass slide again. The mixture was then irradiated under UV light (λ = 365 nm) for 15 min.

Fabrication of in-situ formed AuNPs in the hydrogel top layer: The tetrachloroauric(III) acid trihydrate was dissolved in deionized water for a 1 mM solution. Then, the top layer of a bilayer hydrogel was covered with 1 mM tetrachloroauric(III) acid trihydrate solution. The top layer color turned from very light amber to pinkish.

Surface patterns: The patterns formed immediately when the top layer swelled in water. The development of patterns was realized by immersing the bilayer hydrogel in water for different periods of time.

Characterization: Surface patterns were imaged and their generation and erasure processes were recorded using an Olympus BX60 Microscope. The light source used for plasmonic heating of the bilayers was a high-power LED (405 nm, 100W,

Shenzhen kobee Technology Co., Ltd.). Transmission Electron Microscopy (TEM) measurements were performed with a Philips CM300ST-FEG Transmission Electron Microscope at 300 kV.

References

[1] Wang, Q.; Zhao, X. Beyond Wrinkles: Multimodal Surface Instabilities for Multifunctional Patterning. *MRS Bull.* **2016**, *41*, 115–122.

[2] Ebata, Y.; Croll, A. B.; Crosby, A. J. Wrinkling and Strain Localizations in Polymer Thin Films. *Soft Matter* **2012**, *8*, 9086–9091.

[3] Weiss, F.; Cai, S.; Hu, Y.; Kyoo Kang, M.; Huang, R.; Suo, Z. Creases and Wrinkles on the Surface of a Swollen Gel. *J. Appl. Phys.* **2013**, *114*, 073507

[4] Hou, H.; Yin, J.; Jiang, X. Reversible Diels–Alder Reaction To Control Wrinkle Patterns: From Dynamic Chemistry to Dynamic Patterns. *Adv. Mater.* **2016**, *28*, 9126–9132.

[5] Guvendiren, M.; Burdick, J. A.; Yang, S. Kinetic Study of Swelling-Induced Surface Pattern Formation and Ordering in Hydrogel Films with Depth-Wise Crosslinking Gradient. *Soft Matter* **2010**, *6*, 2044–2049.

[6] Chen, D.; Jin, L.; Suo, Z.; Hayward, R. C. Controlled Formation and Disappearance of Creases. *Mater. Horizons* **2014**, *1*, 207–213.

[7] Rhee, D.; Lee, W.-K.; Odom, T. W. Crack-Free, Soft Wrinkles Enable Switchable Anisotropic Wetting. *Angew. Chemie* **2017**, *129*, 6623–6627.

[8] Cao, Y.; Hutchinson, J. W. From Wrinkles to Creases in Elastomers: The Instability and Imperfection-Sensitivity of Wrinkling. *Proc. R. Soc. A Math. Phys. Eng. Sci.* **2012**, *468*, 94–115.

[9] Zong, C.; Zhao, Y.; Ji, H.; Han, X.; Xie, J.; Wang, J.; Cao, Y.; Jiang, S.; Lu, C. Tuning and Erasing Surface Wrinkles by Reversible Visible-Light-Induced Photoisomerization. *Angew. Chemie - Int. Ed.* **2016**, *55*, 3931–3935.

[10] Lee, W. K.; Jung, W. Bin; Nagel, S. R.; Odom, T. W. Stretchable Superhydrophobicity from Monolithic, Three-Dimensional Hierarchical Wrinkles. *Nano Lett.* **2016**, *16*, 3774–3779.

[11] Genzer, J.; Groenewold, J. Soft Matter with Hard Skin: From Skin Wrinkles to Templating and Material Characterization. *Soft Matter* **2006**, *2*, 310–323.

[12] Chen, Y. C.; Crosby, A. J. High Aspect Ratio Wrinkles via Substrate Prestretch. *Adv. Mater.* **2014**, *26*, 5626–5631.

[13] Chan, E. P.; Smith, E. J.; Hayward, R. C.; Crosby, A. J. Surface Wrinkles for Smart Adhesion. *Adv. Mater.* **2008**, *20*, 711–716.

[14] Chan, E. P.; Crosby, A. J. Fabricating Microlens Arrays by Surface Wrinkling. *Adv. Mater.* **2006**, *18*, 3238–3242.

[15] Chan, H. F.; Zhao, R.; Parada, G. A.; Meng, H.; Leong, K. W.; Griffith, L. G.; Zhao, X. Folding Artificial Mucosa with Cell-Laden Hydrogels Guided by Mechanics Models. *Proc. Natl. Acad. Sci. U. S. A.* **2018**, *115*, 7503–7508.

[16] Zeng, S.; Li, R.; Freire, S. G.; Garbellotto, V. M. M.; Huang, E. Y.; Smith, A. T.; Hu, C.; Tait, W. R. T.; Bian, Z.; Zheng, G.; Zhang, D.; Sun, L. Moisture-Responsive Wrinkling Surfaces with Tunable Dynamics. *Adv. Mater.* **2017**, *29*, 1–7.

[17] Lee, S. G.; Lee, D. Y.; Lim, H. S.; Lee, D. H.; Lee, S.; Cho, K. Switchable Transparency and Wetting of Elastomeric Smart Windows. *Adv. Mater.* **2010**, *22*, 5013–5017.

[18] Wu, K.; Sun, Y.; Yuan, H.; Zhang, J.; Liu, G.; Sun, J. Harnessing Dynamic Wrinkling Surfaces for Smart Displays. *Nano Lett.* **2020**, *20*, 4129–4135.

[19] Khang, D. Y.; Rogers, J. A.; Lee, H. H. Mechanical Buckling: Mechanics, Metrology, and Stretchable Electronics. *Adv. Funct. Mater.* **2009**, *19*, 1526–1536.

[20] Hu, X.; Dou, Y.; Li, J.; Liu, Z. Buckled Structures: Fabrication and Applications in Wearable Electronics. *Small* **2019**, *15*, 1–26.

[21] Stafford, C. M.; Harrison, C.; Beers, K. L.; Karim, A.; Amis, E. J.; Vanlandingham, M. R.; Kim, H. C.; Volksen, W.; Miller, R. D.; Simonyi, E. E. A Buckling-Based Metrology for Measuring the Elastic Moduli of Polymeric Thin Films. *Nat. Mater.* **2004**, *3*, 545–550.

[22] Goel, P.; Kumar, S.; Sarkar, J.; Singh, J. P. Mechanical Strain Induced Tunable Anisotropic Wetting on Buckled PDMS Silver Nanorods Arrays. *ACS Appl. Mater. Interfaces* **2015**, *7*, 8419–8426.

[23] Stoychev, G.; Turcaud, S.; Dunlop, J. W. C.; Ionov, L. Hierarchical Multi-Step Folding of Polymer Bilayers. *Adv. Funct. Mater.* **2013**, *23*, 2295–2300.

[24] Li, F.; Hou, H.; Yin, J.; Jiang, X. Near-Infrared Light–Responsive Dynamic Wrinkle Patterns. *Sci. Adv.* **2018**, *4*, 1–9.

[25] Li, F.; Hou, H.; Yin, J.; Jiang, X. Multi-Responsive Wrinkling Patterns by the Photoswitchable Supramolecular Network. *ACS Macro Lett.* **2017**, *6*, 848–853.

[26] Backman, D. E.; LeSavage, B. L.; Shah, S. B.; Wong, J. Y. A Robust Method to Generate Mechanically Anisotropic Vascular Smooth Muscle Cell Sheets for Vascular Tissue Engineering. *Macromol. Biosci.* **2017**, *17*, 1–13.

[27] Sack, L.; Scoffoni, C.; McKown, A. D.; Frole, K.; Rawls, M.; Havran, J. C.; Tran, H.; Tran, T. Developmentally Based Scaling of Leaf Venation Architecture Explains Global Ecological Patterns. *Nat. Commun.* **2012**, *3*.

[28] Wang, Z.; Tonderys, D.; Leggett, S. E.; Williams, E. K.; Kiani, M. T.; Spitz Steinberg, R.; Qiu, Y.; Wong, I. Y.; Hurt, R. H. Wrinkled, Wavelength-Tunable Graphene-Based Surface Topographies for Directing Cell Alignment and Morphology. *Carbon N. Y.* **2016**, *97*, 14–24.

[29] Rhee, D.; Lee, W. K.; Odom, T. W. Crack-Free, Soft Wrinkles Enable Switchable Anisotropic Wetting. *Angew. Chemie - Int. Ed.* **2017**, *56*, 6523–6527.

[30] Wu, G.; Xia, Y.; Yang, S. Buckling, Symmetry Breaking, and Cavitation in Periodically Micro-Structured Hydrogel Membranes. *Soft Matter* **2014**, *10*, 1392–1399.

[31] Hou, J.; Li, Q.; Han, X.; Lu, C. Swelling/Deswelling-Induced Reversible Surface Wrinkling on Layer-by-Layer Multilayers. *J. Phys. Chem. B* **2014**, *118*, 14502–14509.
[32] Guvendiren, M.; Burdick, J. A.; Yang, S. Solvent Induced Transition from Wrinkles to Creases in Thin Film Gels with Depth-Wise Crosslinking Gradients. *Soft Matter* **2010**, *6*, 5795–5801.
[33] Yang, S.; Khare, K.; Lin, P. C. Harnessing Surface Wrinkle Patterns in Soft Matter. *Adv. Funct. Mater.* **2010**, *20*, 2550–2564.
[34] Zhao, Z.; Gu, J.; Zhao, Y.; Guan, Y.; Zhu, X. X.; Zhang, Y. Hydrogel Thin Film with Swelling-Induced Wrinkling Patterns for High-Throughput Generation of Multicellular Spheroids. *Biomacromolecules* **2014**, *15*, 3306–3312.
[35] Yoon, J.; Bian, P.; Kim, J.; McCarthy, T. J.; Hayward, R. C. Local Switching of Chemical Patterns through Light-Triggered Unfolding of Creased Hydrogel Surfaces. *Angew. Chemie - Int. Ed.* **2012**, *51*, 7146–7149.
[36] Lin, G.; Li, J.; Xu, Z.; Ge, D.; Sun, W.; Chen, P. Hierarchical Surface Patterns via Global Wrinkling on Curved Substrate for Fluid Drag Control. *Adv. Mater. Interfaces* **2020**, *2001489*, 1–12.
[37] Guvendiren, M.; Yang, S.; Burdick, J. A. Swelling-Induced Surface Patterns in Hydrogels with Gradient Crosslinking Density. *Adv. Funct. Mater.* **2009**, *19*, 3038–3045.
[38] Zhao, Y.; Han, X.; Li, G.; Lu, C.; Cao, Y.; Feng, X. Q.; Gao, H. Effect of Lateral Dimension on the Surface Wrinkling of a Thin Film on Compliant Substrate Induced by Differential Growth/Swelling. *J. Mech. Phys. Solids* **2015**, *83*, 129–145.
[39] Chen, X.; Hutchinson, J. W. A Family of Herringbone Patterns in Thin Films. *Scr. Mater.* **2004**, *50*, 797–801.
[40] Huang, Z.; Hong, W.; Suo, Z. Evolution of Wrinkles in Hard Films on Soft Substrates. *Phys. Rev. E - Stat. Physics, Plasmas, Fluids, Relat. Interdiscip. Top.* **2004**, *70*, 4.
[41] Wang, Q.; Zhao, X. A Three-Dimensional Phase Diagram of Growth-Induced Surface Instabilities. *Sci. Rep.* **2015**, *5*, 1–10.
[42] Shyer, A. E.; Tallinen, T.; Nerurkar, N. L.; Wei, Z.; Gil, E. S.; Kaplan, D. L.; Tabin, C. J.; Mahadevan, L. Villification: How the Gut Gets Its Villi. *Science* **2013**, *342*, 212–218.
[43] Hailes, R. L. N.; Oliver, A. M.; Gwyther, J.; Whittell, G. R.; Manners, I. Polyferrocenylsilanes: Synthesis, Properties, and Applications. *Chem. Soc. Rev.* **2016**, *45*, 5358–5407.
[44] Feng, X.; Hempenius, M. A.; Vancso, G. J. Metal Nanoparticle Foundry with Redox Responsive Hydrogels. *Macromol. Chem. Phys.* **2018**, *219*, 1–7.
[45] Feng, X.; Zhang, K.; Chen, P.; Sui, X.; Hempenius, M. A.; Liedberg, B.; Vancso, G. J. Highly Swellable, Dual-Responsive Hydrogels Based on PNIPAM and Redox Active Poly(Ferrocenylsilane) Poly(Ionic Liquid)s:

Synthesis, Structure, and Properties. *Macromol. Rapid Commun.* **2016**, *37*, 1939–1944.

[46] Feng, X.; Zhang, K.; Chen, P.; Sui, X.; Hempenius, M. A.; Liedberg, B.; Vancso, G. J. Highly Swellable, Dual-Responsive Hydrogels Based on PNIPAM and Redox Active Poly(Ferrocenylsilane) Poly(Ionic Liquid)s: Synthesis, Structure, and Properties. *Macromol. Rapid Commun.* **2016**, *37*, 1939–1944.

[47] Jin, L.; Suo, Z. Smoothening Creases on Surfaces of Strain-Stiffening Materials. *J. Mech. Phys. Solids* **2015**, *74*, 68–79.

[48] Amiez, C.; Sallet, J.; Hopkins, W. D.; Meguerditchian, A.; Hadj-Bouziane, F.; Ben Hamed, S.; Wilson, C. R. E.; Procyk, E.; Petrides, M. Sulcal Organization in the Medial Frontal Cortex Provides Insights into Primate Brain Evolution. *Nat. Commun.* **2019**, *10*, 1-14.

[49] Subramani, R.; Izquierdo-Alvarez, A.; Bhattacharya, P.; Meerts, M.; Moldenaers, P.; Ramon, H.; Van Oosterwyck, H. The Influence of Swelling on Elastic Properties of Polyacrylamide Hydrogels. *Front. Mater.* **2020**, *7*, 212

[50] Tallinen, T.; Biggins, J. S.; Mahadevan, L. Surface Sulci in Squeezed Soft Solids. *Phys. Rev. Lett.* **2013**, *110*, 024302.

[51] Breid, D.; Crosby, A. J. Effect of Stress State on Wrinkle Morphology. *Soft Matter* **2011**, *7*, 4490–4496.

[52] Chan, E. P.; Crosby, A. J. Spontaneous Formation of Stable Aligned Wrinkling Patterns. *Soft Matter* **2006**, *2*, 324–328.

[53] Cerda, E.; Mahadevan, L. Geometry and Physics of Wrinkling. *Phys. Rev. Lett.* **2003**, *90*, 4.

[54] Yagüe, J. L.; Yin, J.; Boyce, M. C.; Gleason, K. K. Design of Ordered Wrinkled Patterns with Dynamically Tuned Properties. *Phys. Procedia* **2013**, *46*, 40–45.

[55] Tokudome, Y.; Kuniwaki, H.; Suzuki, K.; Carboni, D.; Poologasundarampillai, G.; Takahashi, M. Thermoresponsive Wrinkles on Hydrogels for Soft Actuators. *Adv. Mater. Interfaces* **2016**, *3*, 1500802.

[56] Shi, Q.; Xia, H.; Li, P.; Wang, Y. S.; Wang, L.; Li, S. X.; Wang, G.; Lv, C.; Niu, L. G.; Sun, H. B. Photothermal Surface Plasmon Resonance and Interband Transition-Enhanced Nanocomposite Hydrogel Actuators with Hand-Like Dynamic Manipulation. *Adv. Opt. Mater.* **2017**, *5*, 1–9.

[57] Zhang, K.; Feng, X.; Ye, C.; Hempenius, M. A.; Vancso, G. J. Hydrogels with a Memory: Dual-Responsive, Organometallic Poly(Ionic Liquid)s with Hysteretic Volume-Phase Transition. *J. Am. Chem. Soc.* **2017**, *139*, 10029–10035.

[58] Mingot-Castellano, M. E.; Diaz-Canales, D.; Fernandez-Fuertes, F.; Perera-Alvarez, M.; Caparros-Miranda, I.; Jimenez-Barcenas, R.; Palomo-Bravo, A.; Heiniger Mazo, A. I.; ACC, G. Thrombopoietin Analogs In ITP Patients Daily Practice: Treatment Profile, Efficacy and Safety. *Blood* **2013**, *122*, 4749–4749.

4.5 Supporting Information

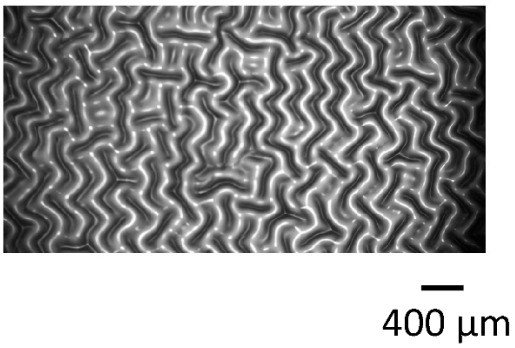

Figure S4.1 OM image of surface pattern on sample T1B3 with a fully swollen bottom layer.

To enhance the visibilities, we prepared 3D surface plot images by using ImageJ function.

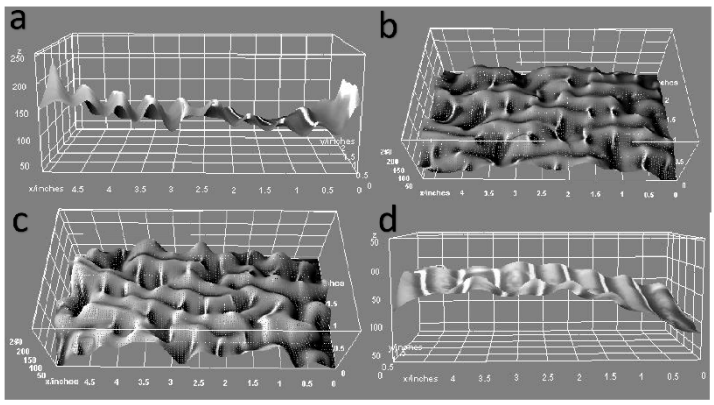

Figure S4.2 3D surface plot images of corresponding surface patterns of Figure 4.8.

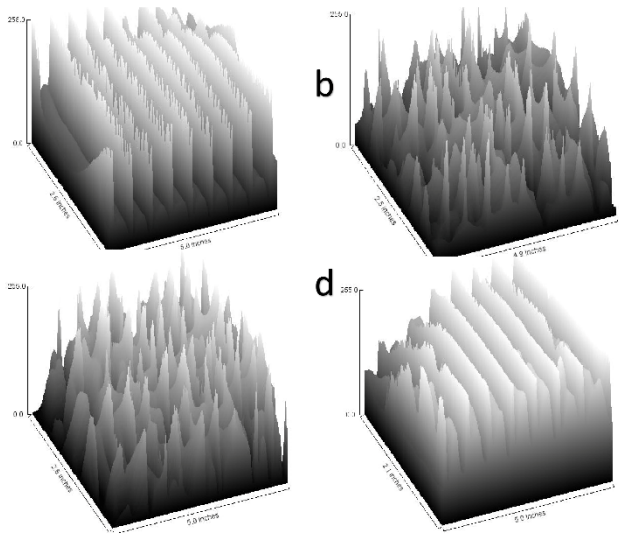

Figure S4.3 Surface plot images of corresponding surface patterns of Figure 4.8.

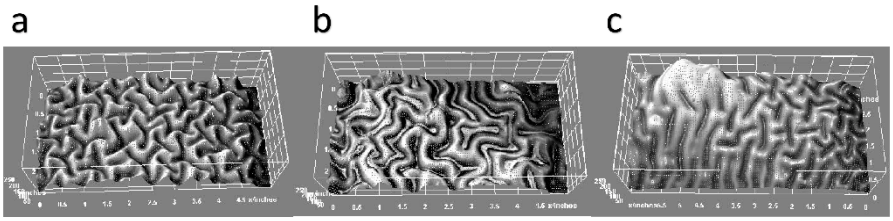

Figure S4.4 Respresentive 3D surface plot images of **a**) folding pattern, **b**) wrinkling pattern, **c**) creasing pattern.

Table S4.1 Wavelength of the surface patterns for bilayer hydrogel samples with different top layers and bottom layers.

Wavelength/μm	**T2**	**T3**
B1	400	650
B2	370	500
B3	280	380
B4	240	300
B5	200	280

Table S4.2 Shear modulus of fully swollen top layers with in-situ synthesized AuNP.

	T1	**T2**	**T3**
Shear modulus/Kpa	27,0	62,8	132

Table S4.3 Shear modulus of bottom layers before swelling up in water.

Shear modulus/Kpa	**B1**	**B2**	**B3**	**B4**	**B5**
Before swelling up in water	2,40	4,00	7,64	8,68	9,68
Fully swollen in water	1,52	3,14	5,30	6,20	7,02

4

Chapter 5

Rapid Anisotropic Actuation of Gold Nanoparticle-Poly(N-isopropylacrylamide)/Poly(vinyl alcohol) Hydrogel Composites

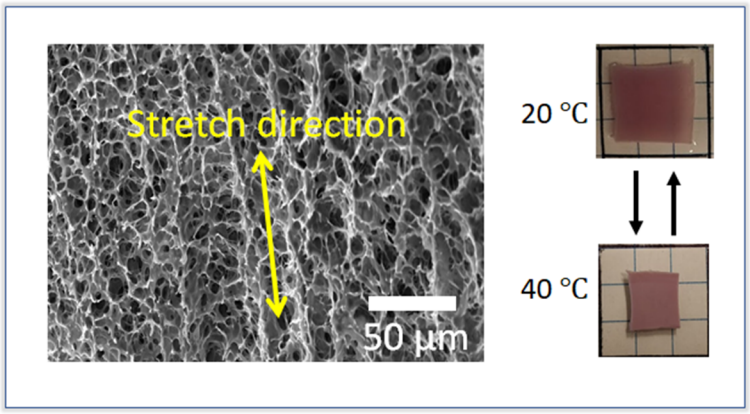

Inspired by biological systems, gold nanoparticle (AuNP) poly(*N*-isopropylacrylamide)(PNIPAM)/poly(vinyl alcohol)(PVA) hydrogel actuators with fast, reversible, macroscopic and anisotropic motion under temperature/light stimuli are described in this Chapter. The anisotropic structures were fabricated by aligning a chemically crosslinked PNIPAM network by means of mechanical stretching and subsequently fixed by a physically crosslinked PVA network which contained in-situ reduced and stabilized AuNPs. The AuNP/hydrogel composites showed remarkable anisotropic mechanical, swelling and de-swelling behavior. Owing to the plasmonic heating effects of AuNPs, the composites exhibited multi-responsive performance under light irradiation and temperature.

5.1 Introduction

For smart functions and movements, biological systems such as muscles, skin, articular cartilage, tendons, and ligaments, possess well-defined hierarchical structures that are anisotropically integrated from the molecular level to a macroscopic length scale.[1,2] The anisotropy often plays an essential role in carrying out particular functions, such as mass transport, surface lubrication, guidance of cell growth, signal transduction, and force generation.[3,4] For example, muscle contraction is achieved with anisotropic arrangement of actin and myosin in the muscle sarcomere, triggered by the presence of calcium ions, and produces macroscale contraction from staggered fibrous structures.[5] However, most synthetic hydrogels demonstrate unordered isotropic structures and weak mechanical properties from homogeneous polymerization of monomers in an aqueous solution, leading to non-oriented deformation in response to environmental stimuli which limits their application.[6–8] Thus, fabricating soft actuators with anisotropic hydrogels and exploring their distinctive behaviors arising from anisotropic effects is of great significance but still challenging.

In recent years, various types of anisotropic hydrogels with oriented structure and anisotropic responsiveness have been developed by self-assembly through intermolecular interactions,[2,9,10] directional freezing,[7,11–13] external field effects,[14,15,16] reaction–diffusion processes,[17,18] and strain or compression induced reorientation.[19,20,21] Anisotropic properties were achieved with anisotropic aligned networks, which were studied in the areas of mechanical performance, optical properties, electrical conductivity and actuating abilities.[12,21–25]

To control the mechanical movement of hydrogel actuators, stimuli-responsive hydrogels were widely used due to their facile fabrication, diverse actuation modes, high degree of freedom during actuation and large volume changes under external stimuli.[16,26,27] Poly(N-isopropylacrylamide) (PNIPAM), as a typical thermo-responsive polymer, has been extensively used for hydrogels. PNIPAM hydrogels can undergo a reversible volume phase transition with a significant size change at a lower critical solution temperature (LCST~32°C).[28] PNIPAM-based actuators have shown significant advantages over many other types of hydrogels because of remote control capabilities when combined with photothermal/magnetothermal materials.[29–

[32] Nevertheless, traditional PNIPAM hydrogels are very fragile with low strength ~5 kPa and modulus ~10 kPa and low response rates due to their low solid contents (70−98% water contents) and lack of energy dissipating mechanisms.[33,34] The softness and fragility lead to a low deliverable force[35,36] and large passive deformation as actuators. For enhancing the mechanical performance, several toughening mechanisms have been proposed, such as creating double networks,[37] fabricating anisotropic structures,[38] incorporating nanocomposites,[32,34,36] and using Hofmeister effects.[39] In spite of these measures, many toughened hydrogels can be applied only under specific application conditions. For example, PNIPAM hydrogels enhanced with Hofmeister effects can only work in high concentration salt solutions.[39] Besides mechanical properties, another factor affecting their application as actuator is the response rate. The actuation of a hydrogel actuator relies on the swelling and de-swelling process induced by the osmotic-pressure changes when exposed to external stimuli.[40] Due to the slow diffusion of water in and out of the hydrogel networks, even a slight volume change in the hydrogel actuator takes several minutes.[41]

High-molecular-weight poly(vinyl alcohol) (PVA) shows excellent mechanical properties due to its high fracture toughness compared to the short chain counterparts.[42] Due to its hydrophilic nature (rich hydroxide group content), PVA has also been used as a reducing agent for the synthesis of gold nanoparticles (AuNPs) in hot water.[43,44] The PVA-stabilized AuNPs showed long term stability without agglomeration. PVA can be physically cross-linked into a hydrogel by forming nanocrystalline domains using cyclic freezing–thawing (FT) and annealing treatments. The frozen–thawed PVA hydrogels have demonstrated enhanced mechanical properties compared with chemically crosslinked PVA hydrogels.[7] The mechanical strength and wear resistance of PVA hydrogels can be further improved by annealing treatments which promote higher degrees of crystallinity.[7,11,42] Many examples for tough anisotropic PVA hydrogels were reported that were produced by applying a stress to the hydrogels during the FT process,[45] by directional freezing[7,11] and by mechanical training.[19] Interestingly, PNIPAM hydrogels incorporating PVA show much faster shrinking and reswelling rates than those of the conventional PNIPAM hydrogels.[41]

Motivated by the enhanced mechanical properties and faster swelling and deswelling rates achieved with anisotropic structures, an interpenetrating polymer network (IPN) hydrogel of PVA/PNIPAM gold nanocomposite was prepared. The hydrogel was chemically crosslinked into a semi-IPN first, then physically

crosslinked into a full-IPN by cyclic FT of pre-stretched hydrogel following by freeze-drying, annealing treatments and swelling in water. The AuNPs loaded in the hydrogel were formed in-situ with PVA as both reducing and stabilizing agent in hot water. Combined with photothermally active AuNPs, light can be absorbed at the resonance wavelength and be converted into thermal energy which induces shrinkage of the hydrogel.[46,47] The PVA/PNIPAM gold nanocomposite hydrogel showed an anisotropic structure with good mechanical properties and fast response rates to light and temperature changes. The hydrogel showed capabilities to lift 100 times of its own weight with 20% contraction strain in the stretched direction and 40% contraction in the perpendicular direction.

5.2 Results and Discussion

5.2.1 Preparation of the thermo-responsive nanocomposite hydrogels

To prepare anisotropic thermo-responsive nanocomposite hydrogels, PVA-stabilized AuNPs were first synthesized. PVA was used as a reducing, capping, and stabilizing agent in a one-step synthesis of AuNPs. PVA was dissolved to form a thin molecular layer which, under specific stirring and heating conditions, underwent mechanochemical stretching as described earlier.[8,9] As a result, OH groups were freed from H-bonding which brought these groups in a rather high-energy metastable state, allowing these OH groups to serve as reducing agents to induce a $Au^{3+} \rightarrow Au$ reaction. With the resulting solution color turning from light yellowish to reddish, AuNPs were formed with an average size of 20 nm. The PVA-stabilized AuNPs were highly stable and did not display any aggregation in the PNIPAM hydrogel precursor solution. PVA-stabilized AuNPs possess a higher stability compared to most AuNPs generated by conventional fabrication methods, due to the steric stabilization of colloidal particles achieved by physical adsorption of polymers on the surface of the particles.[48] As comparison, citrate-capped gold nanoparticles prepared using the classical Turkevich–Frens method are meta-stable at best, which usually aggregate upon salt addition, dialysis, or repetitive centrifugation.

The anisotropic thermo-responsive nanocomposite hydrogel (PNIPAM/PVA (A)) was prepared through a mechanical strain induced method. As shown in Figure 5.1, the semi-IPN composite hydrogels were prepared first with chemical crosslinking

and one cycle of FT, where NIPAM monomer and *N,N'*-methylenebisacrylamide (MBAm) were initiated by lithium phenyl-2,4,6 trimethylbenzoylphosphinate (LAP) and copolymerized and crosslinked in the presence of PVA stabilized AuNPs. As a semi-IPN hydrogel composed of a PNIPAM network with a low degree of crosslinking, the hydrogel can be stretched to form a temporarily oriented structure at a large deformation. The semi-IPN hydrogels were then stretched to a given strain followed by cyclic FT steps to form full-IPN hydrogels. PVA polymer chains possess abundant hydroxyl groups, which can form interchain and intrachain hydrogen bonds. Upon exposure to −20 °C, water in the hydrogel network freezes and forms ice crystals which can expel PVA chains to form regions of high polymer concentration. Hydrogen bonds are able to form when PVA chains are in close contact with each other. The formed H-bonds remain intact in the subsequent thawing process, leading to a second physically crosslinked network which permanently fixes the aligned structure induced by mechanical stretching. With an increasing number of FT cycles, more and more PVA chains are expelled from the PVA solution to form stronger interactions among PVA chains and hence more crystalline regions. The hydrogels were then freeze-dried and subsequently annealed at a temperature of 120 °C for 5h, in order to initiate further crystal growth. Previous studies have shown that an annealing treatment can endow PVA hydrogels with larger crystal size and overall crystallinity.[42] The final hydrogel material is obtained after swelling in deionized water until equilibrium. The hydrogels with 10 wt% PVA content possess a water content of 870 wt%, exhibiting outstanding softness yet good strength. The full-IPN hydrogels appeared opaque compared with the semi-IPN hydrogels because of light scattering by crystalline PVA domains.

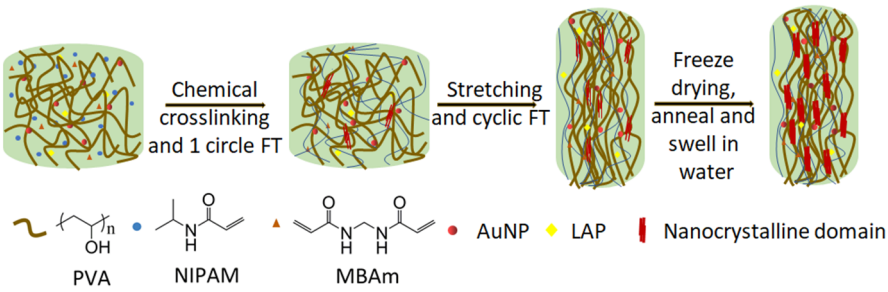

Figure 5.1 Illustration of the fabrication of the anisotropic thermo-responsive nanocomposite hydrogels.

As the TEM images show in Figure 5.2a, the AuNPs incorporated in the hydrogel possessed an average diameter of 20 nm. UV-Vis spectroscopy was carried out to monitor the change in localized surface plasmon resonance (LSPR) properties of the PVA-stabilized AuNPs and hydrogel incorporated AuNPs. As shown in Figure 5.2b, a typical LSPR band of PVA-stabilized AuNPs located at 545 nm was observed, which is in a good agreement with the size determined by TEM. A 5 nm red shift of the LSPR peak was observed when the PVA stabilized-AuNPs were included in the hydrogel matrix and, in addition, the LSPR peak became slightly broader. The LSPR property of AuNPs is dependent on the refractive index and inter-particle distance. No significant change in the LSPR peak was observed. This proves that the AuNPs were dispersed evenly in the hydrogel matrix with barely any coupling between AuNPs or the occurrence of aggregation. The slight shift of the LSPR peak can be induced by a local refractive index change due to the existence of the PNIPAM network.

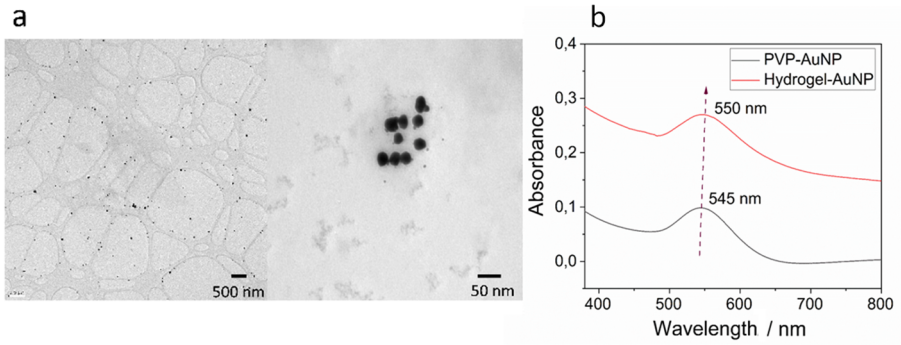

Figure 5.2 TEM images (**a**) and UV-Vis (**b**) absorption spectrum of PVA-stabilized AuNPs.

The hydrogels with PVA-stabilized AuNPs are highly stable with no AuNPs leaking out over a long period of 6 months. The addition of AuNPs into the hydrogels not only improved the mechanical properties (as we shall discuss later) but also endow hydrogels with a light-responsive actuation property. Isotropic thermo-responsive nanocomposite hydrogels (PNIPAM/PVA (I)) were also synthesized under the same procedure without mechanical stretching which were used by contrast.

5.2.2 Structure of polymer networks

The morphologies of the isotropic and anisotropic nanocomposite hydrogels were characterized by scanning electron microscopy (SEM) and polarized optical microscopy (POM). From the cross-sectional SEM images shown in Figure 5.3a, preferentially aligned microstructures were observed for anisotropic nanocomposite hydrogels while the isotropic hydrogels exhibited random and uniform porous structures with an average pore size of 6 μm (Figure 5.3b).

When the hydrogels were placed between crossed polarizers and rotated at 0° and 45° angles, polarized light passed through the isotropic and anisotropic hydrogels. Materials with anisotropic structures could depolarize the light beam, allowing it to pass through the analyzer and be captured. Changes in brightness observed by POM therefore indicates birefringence behavior of hydrogels. For anisotropic hydrogels, when the azimuthal angle between the polarized direction of incident light and stretched direction was 0°, a complete extinction was observed, and a maximum brightness was observed at 45° (Figure 5.3c).. For isotropic hydrogels, however, the POM images observed were both dark at 0° and 45°, indicating no birefringence behavior. This further confirms that anisotropic structures were achieved along the mechanically stretched direction.

The PVA content has a large influence on the mechanical properties of the hydrogels. Hydrogels containing 6 wt% and 3 wt% PVA content possess no aligned microstructures with mechanical stretching (Supporting information), a high water content of 1670 wt% and 2340 wt% and very poor strength. The pore sizes in the hydrogel structures increase significantly from 6 μm (10 wt% PVA) to 25 μm (6 wt% PVA) and 38 μm (3 wt% PVA) as the PVA content is decreased. This is because a high content of PNIPAM chains increases the distance between the PVA chains which prevents the formation of hydrogen bonds and crystallites. A high PVA content can increase the density of crystalline PVA domains, leading to smaller pore sizes. Thus, a low content (less than 6 wt%) of PVA in these hydrogels does not allow the formation of sufficient amounts of physical crosslinks to preserve the temporarily aligned nanostructures generated by mechanical stretching the covalently cross-linked gels.

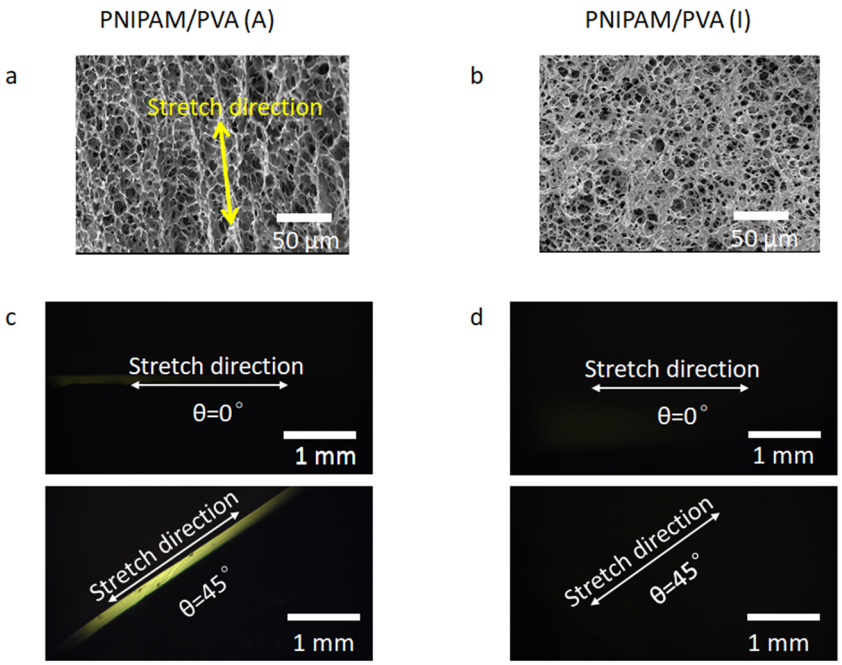

Figure 5.3 SEM and polarized microscope images of PNIPAM/PVA hydrogels. (**a**) SEM image of PNIPAM/PVA (A) investigated from the parallel to the stretch direction. (**b**) SEM image of PNIPAM/PVA (I). (**c**, **d**) Polarized microscope images of PNIPAM/PVA hydrogels.

The macroscopic mechanical properties of the thermo-responsive nanocomposite hydrogels were comparatively investigated by performing tensile tests. As shown in Figure 5.4b, the tensile strength of isotropic hydrogel PNIPAM/PVA (I) is 85 kPa, which is much higher than found for traditional, weak and fragile single network PNIPAM hydrogels which possess strengths of about 5 kPa.[33] To verify the anisotropic mechanical properties of PNIPAM/PVA (A), tensile strength was measured both parallel (PNIPAM/PVA (A∥)) and perpendicular (PNIPAM/PVA (A⊥)) to the stretch direction. Figure 5.4b, shows that there are obvious differences between the mechanical properties of the PNIPAM/PVA (A) hydrogels along the directions parallel and perpendicular to the stretch direction, indicating that the PNIPAM/PVA (A) hydrogels have anisotropic mechanical properties.

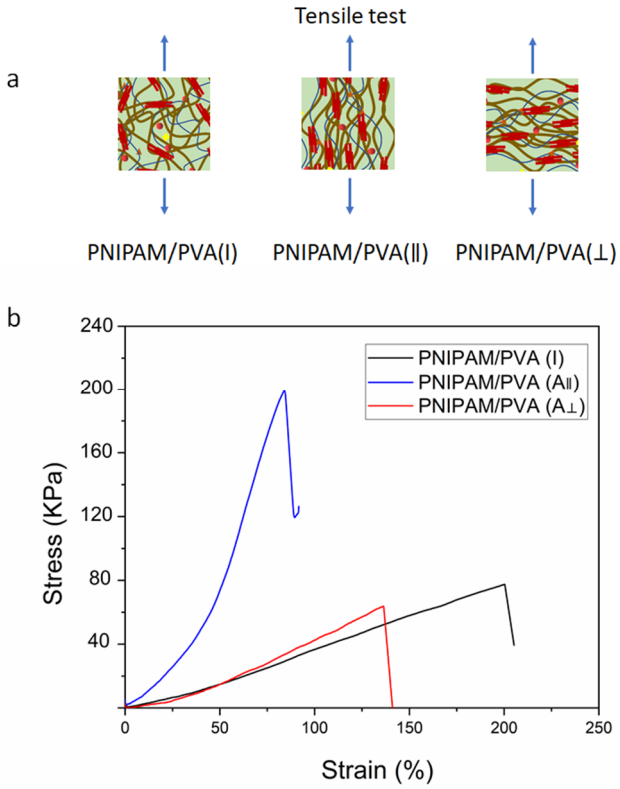

Figure 5.4 The mechanical properties of the PNIPAM/PVA hydrogels. (**a**) Schematic representation for the mechanical tests of the samples; (**b**) tensile stress-strain curves of PNIPAM/PVA (I) hydrogel (black line) and PNIPAM/PVA (A) hydrogel (blue line for the parallel direction, red line for the perpendicular direction). The tensile test diagram shown are representative examples, and they were repeated 3-6 times.

PNIPAM/PVA (A∥) exhibited a tensile strength of 205 kPa which is much higher than that of PNIPAM/PVA (A⊥) (63kPa) and PNIPAM/PVA (I). However, the ruptured strain of the PNIPAM/PVA (A) hydrogel is much lower than PNIPAM/PVA (I), changing from 200% to 87% for PNIPAM/PVA (A∥) and 133% for PNIPAM/PVA (A⊥). Generally, for an isotropic material, much of the load is carried by van der Walls interactions and random coil entanglements between chains. For materials with aligned polymer chains, however, a larger portion of the load can be

transmitted to the main chain covalent bonds when they are stretched in the oriented direction. Thus, the structural alignment of the polymer network could endow the PNIPAM/PVA (A∥) hydrogels with improved tensile strength. Also, PNIPAM/PVA (A) exhibits a lower ruptured strain due to the breaking of the strong, stiff covalent bonds of the polymer chains. Meanwhile, the strength in the perpendicular angles is generally reduced.

5.2.3 Thermo-responsive behavior of hydrogels

To study the thermo-responsive properties of the PNIPAM/PVA hydrogels, bulk hydrogel samples with width × length × thickness of 10 mm × 10 mm × 1 mm were prepared as shown in Figure 5.5a With temperature rising up to 40 ºC, PNIPAM/PVA(I) hydrogel underwent isotropic volume changes with a 30% isotropic contraction strain in X, Y, and Z directions in 30 s. For PNIPAM/PVA (A) hydrogel, however, a 20% contraction was observed in the stretched direction (X-direction) and a 40% contraction in both perpendicular (Y-direction) and Z directions in 30 s. The contraction along the direction parallel to the polymer orientation axis is smaller than in the perpendicular directions due to the higher stiffness in the parallel direction caused by aligned PVA. The anisotropic elasticity of the hydrogels results in the anisotropic swelling and shrinkage. When heated above the LCST of PNIPAM, the hydrogel quickly turned opaquer as the grafted NIPAM chains phase separated from water and formed globules that additionally scattered light further.

It is well known that conventional PNIPAM hydrogels form a dense, thick skin layer when heated above their LCST, which restricts water transport in and out of the hydrogel networks, resulting in slow response rates. Thus, a slight volume change in a PNIPAM hydrogel actuator may require several minutes to complete. Previous studies have shown that the incorporation of PVA in PNIPAM hydrogels accelerated the swelling and deswelling process.[41] The deswelling behavior of PNIPAM/PVA gold nanocomposite hydrogels was studied by recording the weights of hydrogels at specific time intervals after the gels swollen at 20 ºC had been quickly transferred into hot water at 40 ºC. As shown in Figure 5.5b, PNIPAM/PVA (I) lost 67% percent of its weight within 30 s and PNIPAM/PVA (A) lost 73%. The response rate of PNIPAM/PVA hydrogels was enhanced significantly and hydrogels could shrink to the equilibrium state in a very short period of time. This is because the incorporation of PVA hindered the formation of the PNIPAM skin layer. In addition, for

PNIPAM/PVA (A) hydrogels, oriented micrometer-sized hole-like aisles, formed in the aligned network, act as water-releasing channels when the collapse occurs, which further enhances the shrinking rate. In contrast, 6 wt% and 3 wt% PVA content hydrogels require around 3 min and 5 min, respectively, to lose 50 percent of their weight. The deswelling rate increases with increasing PVA content. Clearly, more PVA incorporated into the hydrogel networks leads to more water-releasing channels and easier removal of water from the network when the temperature is raised above the LCST.

Figure 5.5c shows the reversibility of the PNIPAM/PVA hydrogel response to temperature changes. Upon cooling, the hydrogels absorbed water and recovered to their original sizes. The heating and cooling cycles were repeated seven times to prove the reversibility of the swelling and deswelling processes.

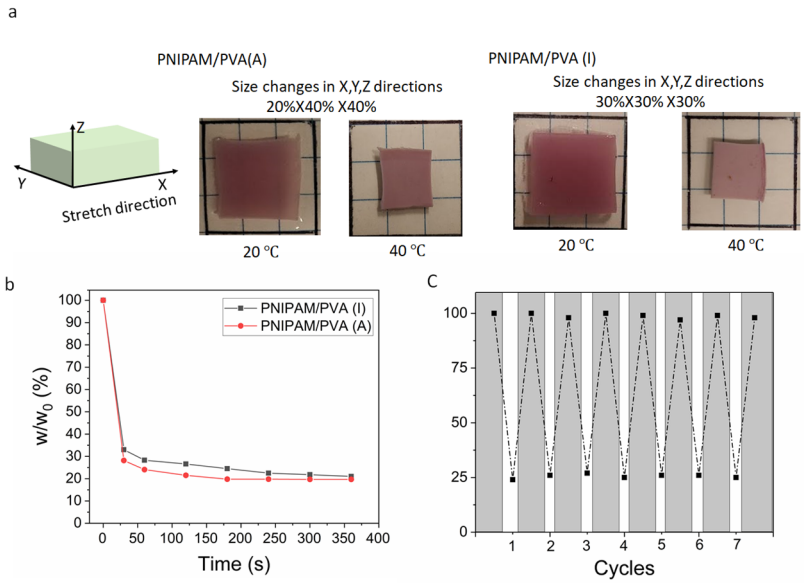

Figure 5.5 Thermo-responsive behavior of the PNIPAM/PVA hydrogels. (**a**) Images of PNIPAM/PVA hydrogels and plots showing the changes in the relative length ($(L_0-L_t)/L_0(\%)$). (**b**) Relative weight of hydrogels changes (w_t/w_0 (%)) vs. time at 40 °C. (**c**) Reversibility of PNIPAM/PVA (A) hydrogel expansion and contraction. L_0 is the original length of hydrogel specimens, L_t is the length of the contracted hydrogels; w_0 is the original weight of hydrogels, and w_t is the weight of the hydrogels at time t.

5.2.4 Actuation properties

The actuation properties of hydrogels when triggered by temperature stimuli were evaluated by investigating the rolling performance of a hydrogel stripe with gradient structures. Isotropic PNIPAM hydrogels display only volume shrinkage without rolling behavior above their LCST. Temperature-responsive rolling characteristics of the composite hydrogel were realized by the design of a gradient structure in the composite hydrogel by employing a gradient in UV intensity along the irradiation axis, which coincided with the long axis of the hydrogel stripe. Higher crosslink densities were achieved with a higher UV intensity, and crosslink densities decreased with a decreasing UV intensity, leading to a gradient hydrogel structure. When temperature was used as stimulus, the side with higher PNIPAM concentration shrunk faster than the other side. As shown in Figure 5.6, the hydrogel stripes curled up to their maximum degree within 30 s in 40 ºC water due to the driving force provided by the asymmetric curling of the two sides of the hydrogel above LCST. The synthesized hydrogel stripes exhibited fast deformation and can be programmed to achieve different structures and actuation behaviors such as folding, bending, curving and wrinkling.

Figure 5.6 Rolling of hydrogel stripe with gradient structures at 40 ºC.

The actuation abilities were further investigated by their use as a weight-lift device. Hydrogel samples were loaded with 5 g of weight and actuated in 40 ºC water as shown in Figure 5.7. PNIPAM/PVA (I) could lift up 100 times of its own weight with a 25% contraction strain in 30 s. For PNIPAM/PVA (A) hydrogels, contraction strain reached 38% for PNIPAM/PVA (A⊥) and 20% for PNIPAM/PVA(A∥) hydrogels with the same 5 g load and actuation conditions.

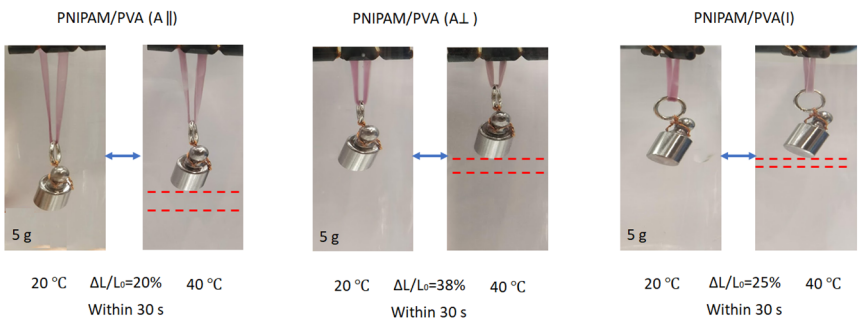

Figure 5.7 Actuation of PNIPAM/PVA hydrogels in 40 °C water.

As known, AuNPs intensively absorb radiation and convert this into heat efficiently and rapidly with light illumination at wavelengths that coincide with the NPs absorption based on localized surface plasmon resonances and intrinsic interband transitions.[32] Here, we investigated the light properties on PNIPAM/PVA (A‖) hydrogels. A high-power LED with a wavelength of 405 nm was used for irradiation. PNIPAM/PVA (A‖) hydrogel was loaded with 5 g and 10 g weight separately and actuated with a high power LED in air. 20% and 10% contraction strains were achieved for 5 g and 10 g weight, respectively, after an irradiation time of 150 s. As shown in Figure 5.8, the light driven contraction showed the same deformation performance as in water but with a longer driving time than in warm water. This can be due to the opaque feature of the hydrogels which hinders penetration of light into the inner parts, resulting in lower heating rates than achieved with warm water.

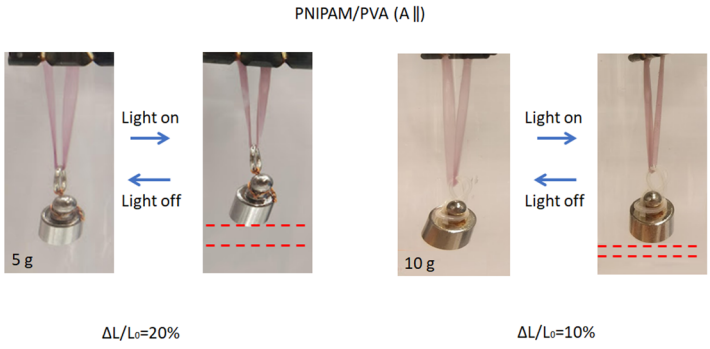

Figure 5.8 Actuation of PNIPAM/PVA (A‖) hydrogels with light irradiation.

5.3 Conclusions

In summary, anisotropic PNIPAM/PVA hydrogels with PVA reduced and stabilized AuNPs were synthesized with the combination of IPN and mechanical strain induced method. The aligned polymer network structure imparted the hydrogels actuators with anisotropic actuation amplitude, good actuation velocity, nice cycle stability, and good anisotropic mechanical performance. PNIPAM/PVA(A) showed tensile strength of 205 kPa and 63kPa along the stretched direction and perpendicular to the stretched direction respectively. Thermal response contraction strain of 20% and 40% were achieved within 30 s in 40 ºC water for PNIPAM/PVA(A∥) and PNIPAM/PVA(A⊥). And hydrogel actuators were able to lift a load with 100 times of their own weight within 30s. Besides, the hydrogels can be actuated by light irradiation. Other types of actuations like bending and rolling can also be achieved by hydrogels with gradient structures. These thermo-responsive hydrogels provide new opportunities for soft materials used in robotics, artificial muscles and soft tissues, etc. The approach developed can be applied to other nanocomposite hydrogel actuators and PVA-based gold nanocomposite materials for anisotropic performance.

5.4 Experimental Section

Materials: N-Isopropylacrylamide (NIPAM, Aldrich, 97%) was recrystallized twice from a toluene-hexane solution (50% v/v) and dried under vacuum prior to use. Poly(vinyl alcohol) (PVA, 99% hydrolyzed, MW 89000−98000 g/mol, Aldrich), N,N'-methylenebisacrylamide (MBAm) (Aldrich, >99%), tetrachloroauric(III) acid trihydrate (Aldrich, >99.9%). Lithium phenyl-2,4,6 trimethylbenzoylphosphinate (LAP) was prepared according to an established procedure.[49] All water used in the experiments was Milli-Q grade.

Fabrication of PVA stabilized AuNPs: A 10 wt% PVA solution was prepared by dissolving PVA granules in deionized water under heating (90 °C). Chloroauric acid (0.5 wt% with respect to PVA) was slowly added to the hot (90 °C) PVA solution under magnetic stirring. The resulting solution was stirred at 90 °C for another 30 min until the solution became reddish, indicating the formation of AuNPs.

Fabrication of nanocomposite hydrogels: NIPAM (65.8 wt%), LAP (2 wt% of NIPAM), chemical crosslinking agent MBAm (0.06 mol% of NIPAM) were added to cold PVA-AuNP solution. The resulting solution was poured into a glass mold and covered with a glass plate to control the thickness of 1 mm. The solution was crosslinked under ultraviolet irradiation (λ = 365 nm) for 2 h. The hydrogels were then frozen at −20 °C for 12 h followed by thawing at ambient temperature for 2 h. The hydrogels were then cut into a rectangular shape and stretched to a given strain (0, 150%). The FT process was repeated 5 times until the recovery rate was less than 10%. Hydrogel samples were then freeze-dried for 48 h, followed by an annealing treatment at 120 °C for 5 h, and subsequently immersed in water at room temperature until the weight became constant.

Fabrication of nanocomposite hydrogels with gradient structures: The nanocomposite hydrogels with gradient structures were synthesized with the same procedure as mentioned above, but the gel precursor was transferred into a Teflon mold and crosslinked under ultraviolet irradiation (λ = 365 nm) coming from one direction for 2 h. UV irradiation is absorbed by AuNPs and leads to the formation of a light intensity gradient along the irradiation axis. A higher UV intensity causes the generation of a higher concentration of free radicals which accelerates the polymerization of the monomers in comparison to regions subject to lower intensity. Thus, the UV-exposed side has higher crosslink densities than the other side.

Characterization:

Swelling ratio measurements: The swelling ratios of the hydrogels were measured by comparing their weights before and after freeze-drying. Excess surface water was wiped from the hydrogel surface before measurement. The weight before (m_w) and after (m_d) freeze-drying was measured with a balance. The water content was obtained as $[(m_w - m_d)/m_d] \times 100\%$.

Tensile testing: Hydrogel samples were cut into a rectangular shape (50 mm × 20 mm). The thickness of the individual specimens was measured with a caliper and was typically around 1 mm. A universal testing machine (INSTRON 5565) with a load cell of 1 kN was used to perform mechanical tests and the crosshead velocity was kept at 30 mm/min in the tensile measurements.

SEM characterization: SEM was carried out using a HR-LEO 1550 FEF SEM instrument at 1kV.

TEM characterization: Transmission Electron Microscopy (TEM) images were captured using a high-resolution transmission electron microscopy instrument (TEM, Philips CM300ST–FEG). The TEM samples were prepared by deposition of the nanoparticle suspension (10 μL) onto a carbon-coated microscopy copper grid.

UV-Vis spectra: UV-Vis spectra were measured with a TECAN Infinite 200 PRO instrument.

References

[1] Duan, B.; Huang, Y.; Lu, A.; Zhang, L. Recent Advances in Chitin Based Materials Constructed via Physical Methods. *Prog. Polym. Sci.* **2018**, *82*, 1–33.

[2] Ling, S.; Kaplan, D. L.; Buehler, M. J. Nanofibrils in Nature and Materials Engineering. *Nat. Rev. Mater.* **2018,** *3*, 1–15.

[3] Kim, J. K.; Kim, D. H.; Joo, S. H.; Choi, B.; Cha, A.; Kim, K. M.; Kwon, T. H.; Kwak, S. K.; Kang, S. J.; Jin, J. Hierarchical Chitin Fibers with Aligned Nanofibrillar Architectures: A Nonwoven-Mat Separator for Lithium Metal Batteries. *ACS Nano* **2017**, *11*, 6114–6121.

[4] Song, J.; Chen, C.; Zhu, S.; Zhu, M.; Dai, J.; Ray, U.; Li, Y.; Kuang, Y.; Li, Y.; Quispe, N.; Yao, Y.; Gong, A.; Leiste, U. H.; Bruck, H. A.; Zhu, J. Y.; Vellore, A.; Li, H.; Minus, M. L.; Jia, Z.; Martini, A.; Li, T.; Hu, L. Processing Bulk Natural Wood into a High-Performance Structural Material. *Nature* **2018**, *554*, 224–228.

[5] Weber, A.; Murray, J. M. Molecular Control Mechanisms in Muscle Contraction. *Physiol. Rev.* **1973**, *53*, 612–672.

[6] Sano, K.; Ishida, Y.; Aida, T. Synthesis of Anisotropic Hydrogels and Their Applications. *Angew. Chemie - Int. Ed.* **2018**, *57*, 2532–2543.

[7] Zhang, L.; Zhao, J.; Zhu, J.; He, C.; Wang, H. Anisotropic Tough Poly(Vinyl Alcohol) Hydrogels. *Soft Matter* **2012**, *8*, 10439–10447.

[8] Wang, Q.; Asoh, T. A.; Uyama, H. Rapid Uniaxial Actuation of Layered Bacterial Cellulose/Poly(: N -Isopropylacrylamide) Composite Hydrogel with High Mechanical Strength. *RSC Adv.* **2018**, *8*, 12608–12613.

[9] Xiao, S.; Lu, X.; Lu, Q. Photosensitive Polymer from Ionic Self-Assembly of Azobenzene Dye and Poly(Ionic Liquid) and Its Alignment Characteristic toward Liquid Crystal Molecules. *Macromolecules* **2007**, *40*, 7944–7950.

[10] Lee, S. G.; Lim, H. S.; Lee, D. Y.; Kwak, D.; Cho, K. Tunable Anisotropic Wettability of Rice Leaf-like Wavy Surfaces. *Adv. Funct. Mater.* **2013**, *23*, 547–553.

[11] Zhang, H.; Cooper, A. I. Aligned Porous Structures by Directional Freezing. *Adv. Mater.* **2007**, *19*, 1529–1533.

[12] Liu, T.; Huang, M.; Li, X.; Wang, C.; Gui, C. X.; Yu, Z. Z. Highly Compressible Anisotropic Graphene Aerogels Fabricated by Directional Freezing for Efficient Absorption of Organic Liquids. *Carbon N. Y.* **2016**, *100*, 456–464.

[13] Chen, K.; Zong, T.; Chen, Q.; Liu, S.; Xu, L.; Zhang, D. Preparation and Characterization of Polyvinyl Alcohol/ Sodium Alginate/Carboxymethyl Cellulose Composite Hydrogels with Oriented Structure. *Soft Matter* **2021**, *00*, 1–10.

[14] De France, K. J.; Yager, K. G.; Chan, K. J. W.; Corbett, B.; Cranston, E. D.; Hoare, T. Injectable Anisotropic Nanocomposite Hydrogels Direct Growth and Alignment of Myotubes. *Nano Lett.* **2017**, *17*, 6487–6495.

[15] Liu, K.; Han, L.; Tang, P.; Yang, K.; Gan, D.; Wang, X.; Wang, K.; Ren, F.; Fang, L.; Xu, Y.; Lu, Z.; Lu, X. An Anisotropic Hydrogel Based on Mussel-Inspired Conductive Ferrofluid Composed of Electromagnetic Nanohybrids. *Nano Lett.* **2019**, *19*, 8343–8356.

[16] Qin, H.; Zhang, T.; Li, N.; Cong, H. P.; Yu, S. H. Anisotropic and Self-Healing Hydrogels with Multi-Responsive Actuating Capability. *Nat. Commun.* **2019**, *10*, 1–11.

[17] Wu, Z. L.; Kurokawa, T.; Sawada, D.; Hu, J.; Furukawa, H.; Gong, J. P. Anisotropic Hydrogel from Complexation-Driven Reorientation of Semirigid Polyanion at Ca^{2+} Diffusion Flux Front. *Macromolecules* **2011**, *44*, 3535–3541.

[18] Mredha, M. T. I.; Tran, V. T.; Jeong, S. G.; Seon, J. K.; Jeon, I. A Diffusion-Driven Fabrication Technique for Anisotropic Tubular Hydrogels. *Soft Matter* **2018**, *14*, 7706–7713.

[19] Lin, S.; Liu, J.; Liu, X.; Zhao, X. Muscle-like Fatigue-Resistant Hydrogels by Mechanical Training. *Proc. Natl. Acad. Sci. U. S. A.* **2019**, *116*, 10244–10249.

[20] Liang, X.; Chen, G.; Lin, S.; Zhang, J.; Wang, L.; Zhang, P.; Wang, Z.; Wang, Z.; Lan, Y.; Ge, Q.; Liu, J. Anisotropically Fatigue-Resistant Hydrogels. *Adv. Mater.* **2021**, *33*, 1–8.

[21] Tang, Z.; Huang, Q.; Liu, Y.; Chen, Y.; Guo, B.; Zhang, L. Uniaxial Stretching-Induced Alignment of Carbon Nanotubes in Cross-Linked Elastomer Enabled by Dynamic Cross-Link Reshuffling. *ACS Macro Lett.* **2019**, *8*, 1575–1581.

[22] Small, W. R.; Paunov, V. N. Dielectrophoretic Fabrication of Electrically Anisotropic Hydrogels with Bio-Functionalised Silver Nanowires. *J. Mater. Chem. B* **2013**, *1*, 5798–5805.

[23] Ahadian, S.; Ramón-Azcón, J.; Estili, M.; Liang, X.; Ostrovidov, S.; Shiku, H.; Ramalingam, M.; Nakajima, K.; Sakka, Y.; Bae, H.; Matsue, T.;

Khademhosseini, A. Hybrid Hydrogels Containing Vertically Aligned Carbon Nanotubes with Anisotropic Electrical Conductivity for Muscle Myofiber Fabrication. *Sci. Rep.* **2014**, *4*, 1–11.

[24] Kong, W.; Wang, C.; Jia, C.; Kuang, Y.; Pastel, G.; Chen, C.; Chen, G.; He, S.; Huang, H.; Zhang, J.; Wang, S.; Hu, L. Muscle-Inspired Highly Anisotropic, Strong, Ion-Conductive Hydrogels. *Adv. Mater.* **2018**, *30*, 1–7.

[25] Mredha, M. T. I.; Le, H. H.; Tran, V. T.; Trtik, P.; Cui, J.; Jeon, I. Anisotropic Tough Multilayer Hydrogels with Programmable Orientation. *Mater. Horizons* **2019**, *6*, 1504–1511.

[26] Rhee, D.; Lee, W. K.; Odom, T. W. Crack-Free, Soft Wrinkles Enable Switchable Anisotropic Wetting. *Angew. Chemie - Int. Ed.* **2017**, *56*, 6523–6527.

[27] Le, X.; Lu, W.; Zhang, J.; Chen, T. Recent Progress in Biomimetic Anisotropic Hydrogel Actuators. *Adv. Sci.* **2019**, *6,* 1801584.

[28] Chung, J. E.; Yokoyama, M.; Yamato, M.; Aoyagi, T.; Sakurai, Y.; Okano, T. Thermo-Responsive Drug Delivery from Polymeric Micelles Constructed Using Block Copolymers of Poly(N-Isopropylacrylamide) and Poly(Butylmethacrylate). *J. Control. Release* **1999**, *62*, 115–127.

[29] Li, L.; Scheiger, J. M.; Levkin, P. A. Design and Applications of Photoresponsive Hydrogels. *Adv. Mater.* **2019**, *31*, 1807333.

[30] Zhu, C. H.; Lu, Y.; Peng, J.; Chen, J. F.; Yu, S. H. Photothermally Sensitive Poly(N-Isopropylacrylamide)/Graphene Oxide Nanocomposite Hydrogels as Remote Light-Controlled Liquid Microvalves. *Adv. Funct. Mater.* **2012**, *22*, 4017–4022.

[31] Chen, T.; Hou, K.; Ren, Q.; Chen, G.; Wei, P.; Zhu, M. Nanoparticle–Polymer Synergies in Nanocomposite Hydrogels: From Design to Application. *Macromol. Rapid Commun.* **2018**, *39*, 1–26.

[32] Zhang, C. L.; Cao, F. H.; Wang, J. L.; Yu, Z. L.; Ge, J.; Lu, Y.; Wang, Z. H.; Yu, S. H. Highly Stimuli-Responsive Au Nanorods/Poly(N-Isopropylacrylamide) (PNIPAM) Composite Hydrogel for Smart Switch. *ACS Appl. Mater. Interfaces* **2017**, *9*, 24857–24863.

[33] Shibayama, M. Structure-Mechanical Property Relationship of Tough Hydrogels. *Soft Matter* **2012**, *8*, 8030–8038.

[34] Haq, M. A.; Su, Y.; Wang, D. Mechanical Properties of PNIPAM Based Hydrogels: A Review. *Mater. Sci. Eng. C* **2017**, *70*, 842–855.

[35] Illeperuma, W. R. K.; Sun, J. Y.; Suo, Z.; Vlassak, J. J. Force and Stroke of a Hydrogel Actuator. *Soft Matter* **2013**, *9*, 8504–8511.

[36] Depa, K.; Strachota, A.; Šlouf, M.; Hromádková, J. Fast Temperature-Responsive Nanocomposite PNIPAM Hydrogels with Controlled Pore Wall Thickness: Force and Rate of T-Response. *Eur. Polym. J.* **2012**, *48*, 1997–2007.

[37] Zarrintaj, P.; Jouyandeh, M.; Ganjali, M. R.; Hadavand, B. S.; Mozafari, M.; Sheiko, S. S.; Vatankhah-Varnoosfaderani, M.; Gutiérrez, T. J.; Saeb, M. R.

Thermo-Sensitive Polymers in Medicine: A Review. *Eur. Polym. J.* **2019**, *117*, 402–423.

[38] Tang, P.; Yan, H.; Chen, L.; Wu, Q.; Zhao, T.; Li, S.; Gao, H.; Liu, M. Anisotropic Nanocomposite Hydrogels with Enhanced Actuating Performance through Aligned Polymer Networks. *Sci. China Mater.* **2020**, *63*, 832–841.

[39] Hua, M.; Wu, D.; Wu, S.; Ma, Y.; Alsaid, Y.; He, X. 4D Printable Tough and Thermoresponsive Hydrogels. *ACS Appl. Mater. Interfaces* **2021**, *13*, 12689–12697.

[40] Liu, J.; Xu, W.; Kuang, Z.; Dong, P.; Yao, Y.; Wu, H.; Liu, A.; Ye, F. Gradient Porous PNIPAM-Based Hydrogel Actuators with Rapid Response and Flexibly Controllable Deformation. *J. Mater. Chem. C* **2020**, *8*, 12092–12099.

[41] Zhang, J. T.; Cheng, S. X.; Zhuo, R. X. Poly(Vinyl Alcohol)/Poly(N-Isopropylacrylamide) Semi-Interpenetrating Polymer Network Hydrogels with Rapid Response to Temperature Changes. *Colloid Polym. Sci.* **2003**, *281*, 580–583.

[42] Ou, K.; Dong, X.; Qin, C.; Ji, X.; He, J. Properties and Toughening Mechanisms of PVA/PAM Double-Network Hydrogels Prepared by Freeze-Thawing and Anneal-Swelling. *Mater. Sci. Eng. C* **2017**, *77*, 1017–1026.

[43] Sun, C.; Qu, R.; Ji, C.; Meng, Y.; Wang, C.; Sun, Y.; Qi, L. Preparation and Property of Polyvinyl Alcohol-Based Film Embedded with Gold Nanoparticles. *J. Nanoparticle Res.* **2009**, *11*, 1005–1010.

[44] Ram, S.; Tripathy, P.; Fecht, H. J. Gold Nanoparticles Reinforced Polyvinyl Alcohol of Self-Standing Optical Films. *J. Nanosci. Nanotechnol.* **2007**, *7*, 3200–3206.

[45] Chee, B. S.; Goetten de Lima, G.; Devine, D. M.; Nugent, M. J. D. Investigation of the Effects of Orientation on Freeze/Thawed Polyvinyl Alcohol Hydrogel Properties. *Mater. Today Commun.* **2018**, *17*, 82–93.

[46] Shi, Q.; Xia, H.; Li, P.; Wang, Y. S.; Wang, L.; Li, S. X.; Wang, G.; Lv, C.; Niu, L. G.; Sun, H. B. Photothermal Surface Plasmon Resonance and Interband Transition-Enhanced Nanocomposite Hydrogel Actuators with Hand-Like Dynamic Manipulation. *Adv. Opt. Mater.* **2017**, *5*, 1–9.

[47] Hauser, A. W.; Evans, A. A.; Na, J. H.; Hayward, R. C. Photothermally Reprogrammable Buckling of Nanocomposite Gel Sheets. *Angew. Chemie - Int. Ed.* **2015**, *54*, 5434–5437.

[48] Zong, C.; Zhao, Y.; Ji, H.; Han, X.; Xie, J.; Wang, J.; Cao, Y.; Jiang, S.; Lu, C. Tuning and Erasing Surface Wrinkles by Reversible Visible-Light-Induced Photoisomerization. *Angew. Chemie - Int. Ed.* **2016**, *55*, 3931–3935.

[49] Fairbanks, B. D.; Schwartz, M. P.; Bowman, C. N.; Anseth, K. S. Photoinitiated Polymerization of PEG-Diacrylate with Lithium Phenyl-2,4,6-Trimethylbenzoylphosphinate: Polymerization Rate and Cytocompatibility. *Biomaterials* **2009**, *30*, 6702–6707.

5.5 Supporting Information

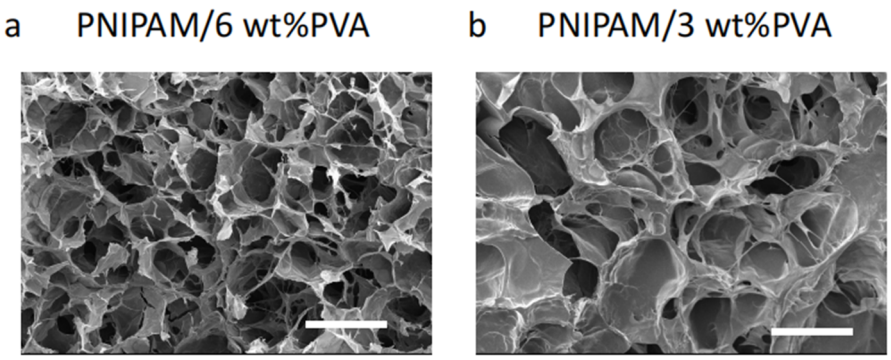

Figure S5.1 SEM images of hydrogels contained 6 wt% (**a**) and 3 wt% (**b**) PVA investigated from parallel to the stretch direction. Scale bar: 50 μm.

Chapter 6

Metal Nanoparticles by Direct Reduction of Electrolytes with Redox- Responsive Poly(ferrocenylsilane)s: Where do the Electrons Come From?

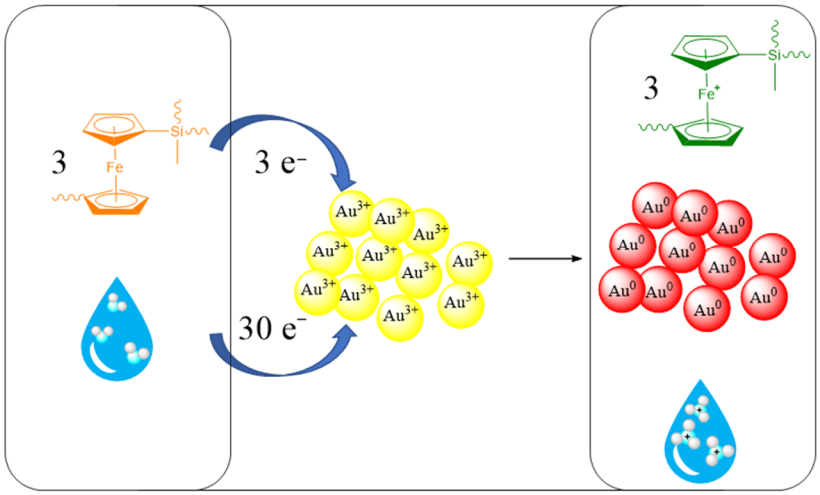

Poly(ferrocenylsilane)s (PFS) as redox responsive organometallic polymers have been used in redox reactions in noble metal ion containing polyelectrolyte solutions, and in hydrogels swollen by polyelectrolytes, with success to prepare metal nanoparticles (NP) by in-situ direct reduction. In this Chapter, we report on a surprising imbalance of stoichiometric ratios in redox reactions with transition metals between metal cations and (PFS) observed in hydrogels. Due to the redox-active

ferrocene center in PFS backbones, well dispersed noble metal nanoparticles are directly formed in-situ in the hydrogel matrix, depending on their redox potential. By careful analysis, extra-stoichiometric amount of gold nanoparticles were found in the reaction when following the principle that exergonic electron transfer from ferrocene to gold(III) with the reduction of Au^{III} to Au^{0} and the iron center's oxidation state increases from II to III. This surprising result is targeted to account for a stoichiometric balance of the electrons in the redox reaction, i.e. we tackle the question of "where do the electrons come from"? First, $HAuCl_4$ was allowed to react with oxidized PFS hydrogel to discover the source of the electrons unaccounted. Regardless of the redox state of PFS, similar amounts of gold nanoparticles were formed. The formation of H^+ ions in the reaction indicates that H_2O could be the possible electron source. A comparison with Pt nanoparticles formation stoichiometry further confirms this hypothesis.

The contents of this chapter have been submitted for publication as: Tibor Halmagyi†, Jinmeng Hao†, Mark Hempenius, G. Julius Vancso, Metal Nanoparticles by Direct Reduction of Electrolytes with Redox- Responsive Poly(ferrocenylsilane)s: Where do the Electrons Come From? †*Tibor Halmagyi and Jinmeng Hao contributed equally to this paper. Submitted.*

6.1 Introduction

Metal nanoparticles (MNPs), typically gold and silver nanoparticles, have attracted intense scientific and technical interest due to their special optical, electronic, and thermal properties;[1] as well as the facile synthesis and surface bioconjugation possibilities[2,3] and feasibility in clinical diagnostics and therapeutics.[4,5] Gold nanoparticles (AuNPs) garnered the most attention owing to their useful optical properties as well as their utility in catalysis, biosensing, and biochemistry. There are numerous well-known methods to produce AuNPs, most often via the reduction of the gold(III) cation of tetrachloroauric acid ($HAuCl_4$) or its salts. The citrate-based, or Turkevich method[6,7] (named after John Turkevich who made significant contributions to the understanding of the reaction) is perhaps the most widely utilized. In this synthesis, trisodium citrate acts as both reductant and the stabilizer of the nanoparticles, referred to as the capping agent. Sodium borohydride can also be used as reductant in a modified Turkevich method, where the citrate only acts as capping agent.[8] $NaBH_4$ can serve as reducing, as well as stabilizing agent, in aqueous solutions.[9] Numerous other small-molecule reductants and capping agents have also been employed for the synthesis of AuNPs and other gold nanostructures, over a wide variety of reaction conditions.[10–13]

Two-phase syntheses involving nonpolar organic solvents have also been described. The Brust-Schiffrin method[14–16] utilizes $NaBH_4$ as reductant, but the stabilization of the MNPs is ensured on the phase boundary through covalent bonding of non-water-soluble alkanethiols to the nanoparticle surface. Another material that has been used for AuNP synthesis at a phase boundary is ferrocene (Fc).[17,18] This metal-organic compound owes its redox activity to the iron(II) ion sandwiched between the two cyclopentadienyl rings. The Fe^{II}/Fe^{III} redox pair's potential is below that of numerous metal ion/metal pairs, making ferrocene- or ferrocene-derivative mediated MNP synthesis possible (Table 6.1).[19] In Astruc's group, a large variety of ferrocenes[17,20–25] were used in THF/water mixtures or ether to reduce aqueous $HAuCl_4$ to gold nanoparticles. The formed water-soluble gold nanoparticles were stabilized by chloride ligands and the electrostatic stabilization provided by the variety of ferriceniums.

Table 6.1 Standard electrode potentials of common half-reactions of MNP formation reactions as well as that of ferrocene and water oxidation[19].

Redox pair	Redox potential vs SHE / V
Au^{3+}/Au	1.50
Pt^{2+}/Pt	1.19
Ir^{3+}/Ir	1.16
Ag^{+}/Ag	0.80
$PtCl_4^{2-}/Pt$	0.76
Rh^{3+}/Rh	0.76
$PdCl_4^{2-}/Pd$	0.64
Fc^{+}/Fc	**0.40**
O_2/H_2O	1.23

Poly(ferrocenylsilane)s (PFSs) are one of the most well-developed classes of metallopolymers with a main chain consisting of alternating silane and ferrocene units. Due to the presence of ferrocene, PFSs possess a high density of redox centers and can be reversibly oxidized and reduced by chemical and electrochemical means.[26–28] PFSs were reported to reduce metal ions to the corresponding MNP by Manners[29–31] as early as 2005 and more recently by our group.[32] Among other macromolecules capable of stabilizing AuNPs[33–35], water-soluble PFSs were found to synthesize AuNPs that were then also stabilized by the polymer chains.[32,36] For PFSs featuring propyl-sulfonate side-chains, when they are used to obtain MNPs, the NPs were also stable in solutions of up to 3 M NaCl. Other PFS containing hydrogels were shown to stabilize in-situ formed nanoparticles within the crosslinked hydrogel system, providing antibacterial properties, higher conductivity and no aggregate formation.[37]

Of course, if progress is to be made towards obtaining designer MNP containing hybrid materials, one must understand the mechanism of the redox process fully. A remarkable result to this end has been recently published by Loh, Nijhuis et al., who have shown that electrons for the gold(III) reduction do not necessarily need to come from a chemical reactant,[38] or from an electrochemical device. The authors have concluded that the electron irradiation under a transmission electron microscope (which was performed in an attempt to obtain further insights into the formation mechanism of the MNPs) can induce AuNP formation from a supersaturated $HAuCl_4$ solution. This result draws attention to the fact that other factors outside the immediate reaction system need to be addressed to account for the MNP formation

mechanism. In addition to external electrons coming from a cathode, photons can also induce AuNP formation.[39–42] Photochemical AuNP synthesis involves the (photo) decomposition of organic precursors into ketyl radicals. These radicals then reduce the gold ions in one-electron transfer steps. These reactions have also been exploited for the preparation of other MNPs, such as silver. When external electron sources participate in MNP reduction process, the formation of the extra amount of MNPs could confuse the assumed reaction stoichiometry between chemical reactant and MNP precursors. In our research group, a PFS containing hydrogel was used for the in-situ formation of MNPs (Au, Ag, Pt, Pd, Rh, Ir) as shown in Figure 6.1.[19] The redox-responsive PFSs were assumed as the only reducing agent in the system which means that each ferrocene unit can provide one electron during the redox process. By changing the amount of $HAuCl_4$, which reacts with constant amount of PFS hydrogel, PFS hydrogel is found capable of reducing more than the stoichiometric amount of $HAuCl_4$. We were surprised by observing this apparent stoichiometric imbalance and embarked upon a systematic study to find an explanation.

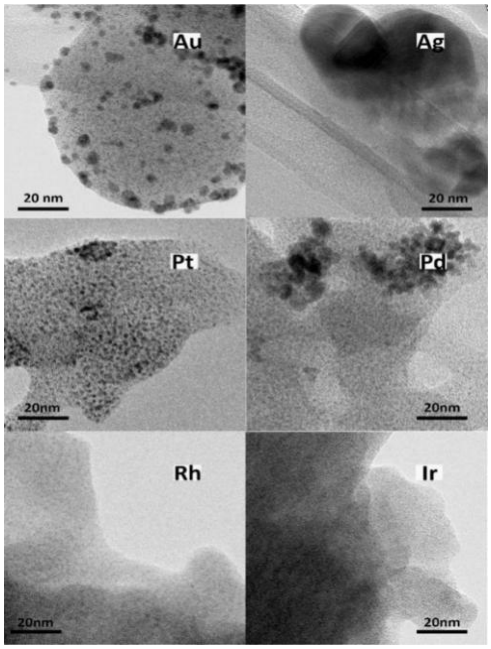

Figure 6. 1 TEM images of the MNPs (Au, Ag, Pt, Pd, Rh, Ir) formed in-situ within a PFS hydrogel. Scale bar: 20 nm.[19]

Additional motivation for this work was triggered by the possibility of PFS-capped AuNPs where the polymer chains bear active side-groups for catalysis, antibacterial uses, sensing, or other applications. For this, precise determination of the reaction stoichiometry and the mechanism of the redox process became necessary. In principle, the stoichiometric reaction of aqueous $HAuCl_4$ with 3 equiv of ferrocene (Equation (1)) results from exergonic electron transfer between Au^{III} and ferrocene corresponding to the reduction of Au^{III} to Au^0, while the iron center's oxidation state in the ferrocene increases from II to III:

$$AuCl_4^- + 3Fc \rightarrow 3Fc^+ + 4Cl^- + Au^0 \quad (1).$$

The same should apply to PFS repeat units as each unit contains one ferrocene group in its main chain. However, in the study of PFS hydrogels for gold nanoparticle formation presented here, about 10 times more than the stoichiometric amount of gold nanoparticles were formed. When PFS hydrogels were oxidized first, and then reacted with $HAuCl_4$, the amount of the resulting gold particles barely changed. This extra-stoichiometric MNP formation has not been found to occur in the in-situ synthesis of PtNPs in PFS hydrogels. The possible origin of the electrons in the process of gold nanoparticle formation will also be discussed here.

6.2 Results and Discussion

The materials shown in Figure 6.2 were used in attempts to synthesize AuNPs, and in the case of **1** to synthesize PtNPs. **1**, $\mathbf{1_{ox}}$ and **2** were used as crosslinked polymeric hydrogels, with a random arrangement of the monomers in the case of **1** and $\mathbf{1_{ox}}$.

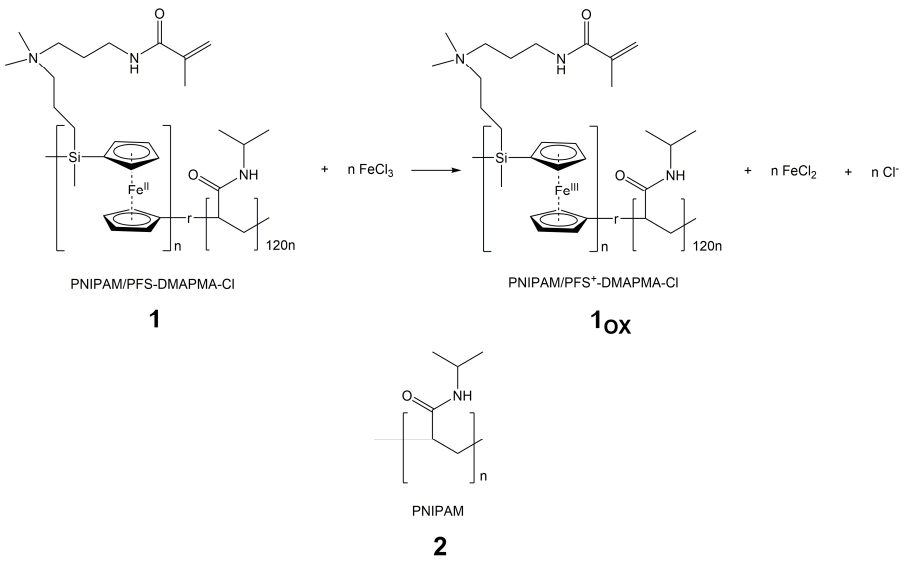

Figure 6.2 Polymer structures used in this study for the synthesis of gold nanoparticles.

6.2.1 Investigations on stoichiometry

Building on previous (inconclusive) experimental data by our group, our first goal was to ascertain whether the reaction between the ferrocene centers of the PNIPAM/PFS-DMAPMA-Cl hydrogel and the gold ions of $HAuCl_4$ proceeds according to the simple 1:3 stoichiometry outlined in Equation (1).

To this end, we immersed dry pieces of 1 into electrolytes containing different concentrations of $HAuCl_4$. Reactions were left to run in the dark for up to 120 h. According to data obtained with UV-Vis spectrophotometry (Figure 6.3 & Table 6.1), up to 13.8 times the stoichiometric amount of Au^{3+} (or 4.6 Au^{3+} equiv. per Fc) was consumed during the reaction, depending on the duration of the experiment. The UV-Vis measurements were conducted at pH 1.1 to avoid the speciation of the $AuCl_4^-$ anion. The two characteristic absorbance peaks of this anion, at 226 and 313 nm, were used to follow the concentration change of the Au^{3+} ions. After 72 h, only the sample with 15x the stoichiometric amount of $HAuCl_4$ exhibited these two peaks. The stoichiometry was calculated to be 4.3 Au^0 synthesized per Fc unit at 72 h, and 4.6 at 120 h.

As a control measurement, we conducted an experiment with a hydrogel only containing crosslinker **2**. In this case, no substantial change in [$AuCl_4^-$] occurred, as can be seen in the Supplementary Information(Figure S6.3).

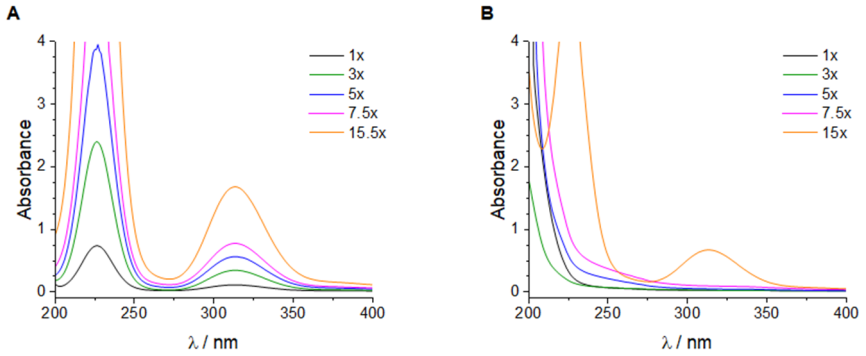

Figure 6.3 UV-Vis spectra of the $HAuCl_4$ solutions before (A) and after immersion of the PFS-containing hydrogel sample (B). The numbers in the legend signify the amount of $HAuCl_4$ in solution compared to the "stoichiometric" amount according to Equation (1).

Building on these data, we conducted a time-dependence study using hydrogels immersed in 15x stoichiometric amounts of $HAuCl_4$. The results (Table 6.1) indicate that the reaction speed dropped after 24 hours. This slowdown of the synthesis can be attributed to two factors: the decreasing concentration of available Au^{3+} and the blocking of the active sites within the hydrogel by the nanoparticles formed. Syntheses longer than 120 h were not attempted, but it can be assumed that more gold would be reduced, albeit at ever slower speeds.

We note that using smaller hydrogel pieces, the reaction proceeded faster, presumably due to the easier diffusion of Au^{3+} moieties into the hydrogel.

In addition to the surprising excess in nanoparticle formation, oxidation of the ferrocene centers with ferric chloride prior to the nanoparticle synthesis only has a minor effect on Δ[$AuCl_4^-$]. This points to a redox reaction distinct from the Fc^+/Fc couple taking place in the system.

The same observations, however, do not apply to the formation of PtNPs: when **1** was immersed in a solution containing an excess amount of K_2PtCl_4 for 24 h, only approximately the stoichiometric amount (0.5 equiv.) of Pt^{2+} was consumed from the electrolyte (Figure S6.2).

Table 6.2 Results of time-controlled AuNP & PtNP syntheses using Fc-containing materials. Stoichiometric amount according to Equation (1) is one Au^{III} per three Fc units. Similarly, the stoichiometry in the case of Pt is one Pt^{II} per two Fc units.

Reductant	n_{Fc} / µmol	t / h	Au^{3+} equiv. per Fc (initial)	Au^{3+} equiv. per Fc(consumed)
1	0.26	3	5.1	1.4
1	0.25	24	5.1	3.7
1	0.26	72	5.1	4.3
1	0.26	120	5.1	4.6
1	1.33	72	5.2	3.0
$\mathbf{1_{ox}}$	1.39	72	5.2	3.1
Reductant	n_{Fc} / µmol	t / h	Pt^{2+} equiv. per Fc (initial)	Pt^{2+} equiv. per Fc (consumed)
1	0.80	24	7.7	0.55

XPS measurements were conducted on dried hydrogel samples (Figure 6.4) to check whether the lower concentration of Au^{3+} in the electrolyte was not simply due to adsorption onto or absorption into the gel. These experiments reinforce the spectroscopic results. The shifted $4f_{5/2}$ and $4f_{7/2}$ peaks of Au^{3+} as compared to Au^0 present an Au^{3+} : Au^0 ratio (79 % Au^0) in line with the change of [$AuCl_4^-$] indicated by UV-Vis in the electrolyte (73 % in the case of this sample), with no other gold moiety detected.

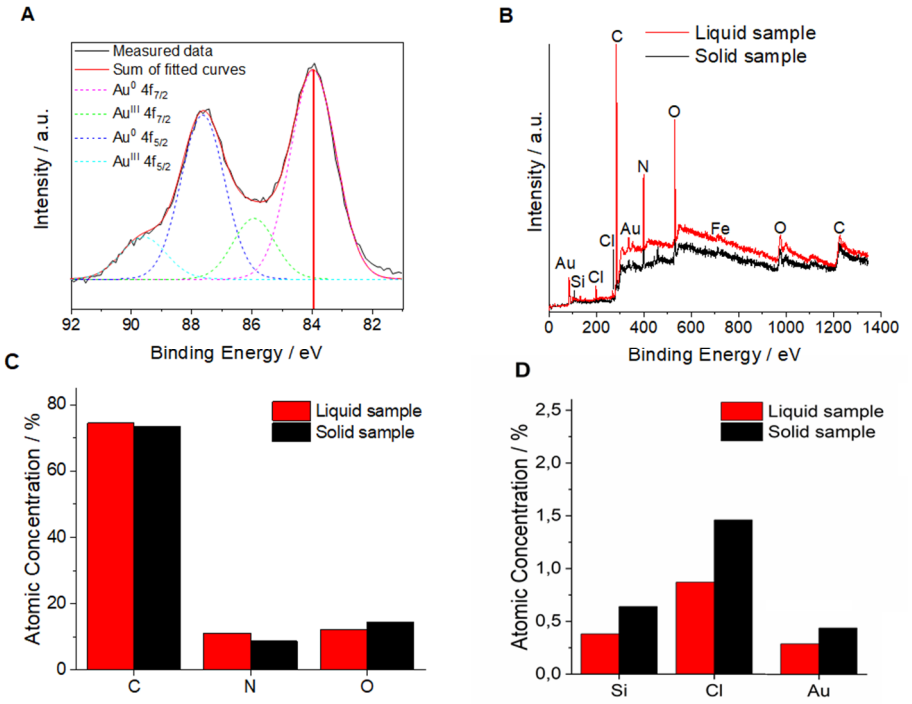

6

Figure 6.4 Results of XPS measurements on the PFS-containing hydrogel samples and dried electrolytes after AuNP synthesis from 15x $HAuCl_4$. The area specific to the gold 4f peaks in the hydrogel sample (**A**). The full spectrum of the samples (**B**). The atomic concentration of majority (**C**) and minority elements (**D**) in the two samples.

In order to prove that no other redox-active material was present in the system, cyclic voltammograms (CV) of the hydrogel was recorded after depositing it on an Indium Tin Oxide (ITO) electrode (Figure 6.5). The CV only shows the characteristic double redox peak of PFS, indicating that no other species within the hydrogel was redox-active in the observed potential range.

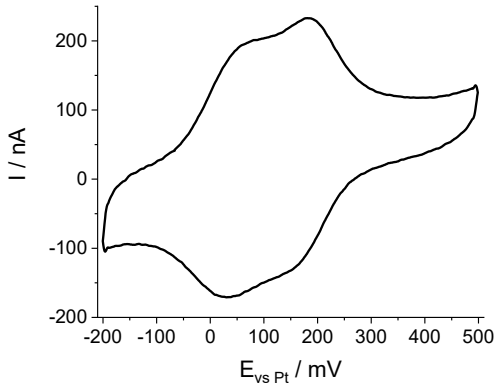

Figure 6.5 Cyclic voltammogram of a PFS/PNIPAM hydrogel on ITO. 0.5 M NaCl; Pt wire counter -and reference electrodes; sweep rate = 10 mV/s.

To shed further light on the processes behind these anomalous results, pH-metric measurements were performed on the electrolytes before and after the immersion of the hydrogel. In the electrolyte we examined, the pH changed from 3.0 to 2.7. This, taking into account the volume and concentration used, corresponds to 1.2 H^+ being freed for every Au^0 formed.

6.2.2 Water oxidation hypothesis

From the above-mentioned experiments we concluded that the mechanism of the gold formation in our system is not as simple as presented in Equation (1). The change in pH, particularly, points to the formation of H^+ or H_3O^+ ions during the reaction. One answer to what could be the source of both these protons and the electrons required for the gold reduction could be that these species form during water oxidation. While the standard potential of the $AuCl_4^-/AuCl_2^-$ or the $AuCl_2^-/Au^0$ redox pairs is below that of the O_2/H_2O couple, uncomplexed Au^{3+} is thermodynamically capable to oxidize water (Table 6.2), though this reaction has a stoichiometry of 3:1 with respect to protons and neutral Au atoms formed (Equations. 2 & 3).

Table 6. 3 Redox pairs relevant to the water oxidation hypothesis.

Redox pair	Redox potential vs SHE / V
$AuCl_4^-/AuCl_2^-$	0.93
$AuCl_2^-/Au^0$	1.15
Au^{3+}/Au^0	1.50
Pt^{2+}/Pt^0	1.19
O_2/H_2O	1.23

$$AuCl_4^- \rightarrow Au^{3+} + 4Cl^-_{bound} \text{ (2)}$$

$$4Au^{3+} + 6H_2O \rightarrow 4Au^0 + 3O_2 + 12H^+ \text{ (3)}$$

This hypothesis could also explain why similar, anomalous results were not observed when Pt was used instead of gold. In this case, the relevant redox pair's potential is slightly lower than that of O_2/H_2O.

6.3 Conclusions

In summary, our investigations have shown that gold nanoparticle formation in PNIPAM/PFS-DMAPMA-Cl hydrogels does not follow the 1:3 stoichiometry represented by the Au^{3+}/Au^0 and Fc^+/Fc redox couples. We have also shown that ferrocene is not the only reducing agent that is operational during MNP formation. Instead, the formation of AuNPs is likely due to a possibly Fc or Fc^+-catalyzed reaction with the confirmed products of Au^0 and hydronium ions. Further research is required to shed light on the precise nature of this process but our findings show that water oxidation by uncomplexed Au^{3+} moieties provides an explanation for our unexpected stoichiometry results.

6.4 Experimental Section

Materials: Poly(ferrocenyl(3-iodopropyl)methylsilane) (M_w:3.12 kDa, M_n: 156 kDa, M_w/M_n = 2.0) was synthesized according to previously published procedure.[36]

Lithium phenyl-2,4,6 trimethylbenzoylphosphinate (LAP) was prepared according to an established procedure.[44] N-[3-(Dimethylamino)propyl]methacrylamide (DMAPMA), N,N'-Methylenebisacrylamide (MBAm), sodium chloride, ferrocene, (dimethylaminomethyl)ferrocene, ferric chloride, tetrachloroauric(III) acid and potassium tetrachloroplatinate(II) were obtained from Aldrich and used without further purification. N-Isopropylacrylamide (NIPAM, Aldrich) was recrystallized twice from a toluene-hexane solution (50% v/v) and dried under vacuum prior to use. Dimethyl sulfoxide (DMSO), terahydrofuran (THF), hexane, ethanol, diethyl ether, toluene, and methanol were obtained from Biosolve. N-isopropylacrylamide (NIPAM, Aldrich) was recrystallized twice from a toluene-hexane solution (50% v/v) and dried under vacuum prior to use.

Synthesis of PFS-DMAPMA-Cl: PFS-DMAPMA-Cl was synthesized according to a previously published procedure.[43] DMAPMA (1.0 mL, 8.3 mmol) in THF/DMSO (2:1 v:v, 12 mL) was allowed to react with poly(ferrocenyl(3-iodopropyl)methylsilane) (0.5 g, 1.26 mmol repeat units) at room temperature for 24 h. After removing THF by N_2 flow, the viscous mixture was diluted with ethanol (20 mL), transferred into a Spectra/Por 4 dialysis hose (MWCO 12-14,000 g/mol) and dialyzed against 0.1 M NaCl (4 × 1 L) and Milli-Q water (4 × 1 L). After removing water by N_2 flow, PFS-DMAPMA-Cl orange flakes (0.6 g, 100%) were obtained.

Synthesis of PNIPAM/ PFS-DMAPMA-Cl hydrogels: A high-power UV-LED (P8D236, Seoul Optodevice Co., South Korea) with a narrow emission spectrum (365±5 nm) was mounted onto a printed circuit board in series with a 4.7 Ω power resistor and operated with a laboratory power supply. NIPAM, PFS-DMAPMA-Cl, MBAm, LAP (photoinitiator) were added into methanol in a mole ratio of NIPAM: PFS-DMAPMA: MBAm: LAP: Methanol =100: 0.47: 1: 1.28: 673. The solution was placed at a distance of 15 mm from the LED. A voltage of 6.7 V was applied to the LED with a fixed forward current of 0.6 A. Photopolymerization was conducted under UV-LED irradiation for 20 min at room temperature. After completion of the photo-polymerization, the gel was washed with milli-Q water to remove unreacted monomer and photoinitiator.

AuNP synthesis with PFS: A PNIPAM/PFS-DMAPMA-Cl (120:1) hydrogel sample was dried and periodically weighed until its mass remained constant, then a

piece with a dry weight between 10 and 20 mg was broken off. This piece was swollen in water for at least an hour, then the extra water was removed from the vial. The sample was weighed again so that the water absorbed by the hydrogel could be accounted for, then the $HAuCl_4$ electrolyte was added into the vial. The Au^{3+} to Fc ratio was adjusted by changing the concentration of $HAuCl_4$ in the electrolyte. The reaction was left to proceed for a given time in the dark, during which time both the hydrogel and the electrolyte turned purple.

In one case, the hydrogel was immersed in a solution containing an excess amount of $FeCl_3$ (36.4 mmol $FeCl_3$ to a hydrogel containing 1.43 mmol Fc units) before the nanoparticle synthesis. The sample was left in the dark overnight, during which time the hydrogel turned to dark green, the typical color for oxidized PFS hydrogels. We repeatedly washed the hydrogel with water to remove the unreacted $FeCl_3$ as well as the $FeCl_2$ resulting from the reaction, then we proceeded with the AuNP synthesis as described above.

PtNP synthesis with PFS: The procedure was identical to that of the AuNP synthesis. The Pt^{2+} to Fc ratio was chosen to be 7.7:1 (15.4 times the stoichiometric amount of Pt^{2+}). The reaction was left to proceed overnight, or over two nights in the dark, during which time the color of the hydrogel darkened slightly.

References

[1] Huang, X.; El-Sayed, M. A. Gold Nanoparticles: Optical Properties and Implementations in Cancer Diagnosis and Photothermal Therapy. *Journal of Advanced Research* **2010**, *1* (1), 13–28.

[2] Hamouda, R. A.; Hussein, M. H.; Abo-elmagd, R. A.; Bawazir, S. S. Synthesis and Biological Characterization of Silver Nanoparticles Derived from the Cyanobacterium Oscillatoria Limnetica. *Sci. Rep.* **2019**, *9* (1), 13071.

[3] Li, Y.; Wu, Y.; Ong, B. S. Facile Synthesis of Silver Nanoparticles Useful for Fabrication of High-Conductivity Elements for Printed Electronics. *J. Am. Chem. Soc.* **2005**, *127* (10), 3266–3267.

[4] Huang, L.; Wan, J.; Wei, X.; Liu, Y.; Huang, J.; Sun, X.; Zhang, R.; Gurav, D. D.; Vedarethinam, V.; Li, Y.; Chen, R.; Qian, K. Plasmonic Silver Nanoshells for Drug and Metabolite Detection. *Nat. Commun.* **2017**, *8* (1), 220.

[5] Farooq, M. U.; Novosad, V.; Rozhkova, E. A.; Wali, H.; Ali, A.; Fateh, A. A.; Neogi, P. B.; Neogi, A.; Wang, Z. Gold Nanoparticles-Enabled Efficient Dual

Delivery of Anticancer Therapeutics to HeLa Cells. *Sci. Rep.* **2018**, *8* (1), 2907.

[6] Turkevich, J.; Stevenson, P. C.; Hillier, J. The Formation of Colloidal Gold. *J. Phys. Chem.* **1953**, *57* (7), 670–673.

[7] Wuithschick, M.; Birnbaum, A.; Witte, S.; Sztucki, M.; Vainio, U.; Pinna, N.; Rademann, K.; Emmerling, F.; Kraehnert, R.; Polte, J. Turkevich in New Robes: Key Questions Answered for the Most Common Gold Nanoparticle Synthesis. *ACS Nano* **2015**, *9* (7), 7052–7071.

[8] Brown, K. R.; Fox, A. P.; Natan, M. J. Morphology-Dependent Electrochemistry of Cytochrome *c* at Au Colloid-Modified SnO_2 Electrodes. *J. Am. Chem. Soc.* **1996**, *118* (5), 1154–1157.

[9] Deraedt, C.; Salmon, L.; Gatard, S.; Ciganda, R.; Hernandez, R.; Ruiz, J.; Astruc, D. Sodium Borohydride Stabilizes Very Active Gold Nanoparticle Catalysts. *Chem. Commun.* **2014**, *50* (91), 14194–14196.

[10] Zhao, P.; Li, N.; Astruc, D. State of the Art in Gold Nanoparticle Synthesis. *Coord. Chem. Rev.* **2013**, *257* (3–4), 638–665.

[11] Polte, J. Fundamental Growth Principles of Colloidal Metal Nanoparticles – a New Perspective. *CrystEngComm* **2015**, *17* (36), 6809–6830.

[12] Porta, F.; Krpetić, Ž.; Prati, L.; Gaiassi, A.; Scarì, G. Gold-Ligand Interaction Studies of Water-Soluble Aminoalcohol Capped Gold Nanoparticles by NMR. *Langmuir* **2008**, *24* (14), 7061–7064.

[13] Yu, Y.; Wu, Y.; Liu, J.; Zhan, Y.; Wu, D. Ultrasmall Dopamine-Coated Nanogolds: Preparation, Characteristics, and CT Imaging. *Journal of Experimental Nanoscience* **2016**, *11* (sup1), S1–S11.

[14] Brust, M.; Walker, M.; Bethell, D.; Schiffrin, D. J.; Whyman, R. Synthesis of Thiol-Derivatised Gold Nanoparticles in a Two-Phase Liquid–Liquid System. *Chem. Commun.* **2000**, 7, 801–802.

[15] Goulet, P. J. G.; Lennox, R. B. New Insights into Brust−Schiffrin Metal Nanoparticle Synthesis. *J. Am. Chem. Soc.* **2010**, *132* (28), 9582–9584.

[16] Perala, S. R. K.; Kumar, S. On the Mechanism of Metal Nanoparticle Synthesis in the Brust–Schiffrin Method. *Langmuir* **2013**, *29* (31), 9863–9873.

[17] Ciganda, R.; Irigoyen, J.; Gregurec, D.; Hernández, R.; Moya, S.; Wang, C.; Ruiz, J.; Astruc, D. Liquid–Liquid Interfacial Electron Transfer from Ferrocene to Gold(III): An Ultrasimple and Ultrafast Gold Nanoparticle Synthesis in Water under Ambient Conditions. *Inorg. Chem.* **2016**, *55* (13), 6361–6363.

[18] Sabahat, S.; Janjua, N. K.; Akhter, Z.; Hassan, M. U. Ferrocene-Functionalized Gold Nanoparticles: Study of a Simple Synthesis Method and Their Electrochemical Behavior. *Chem. Pap.* **2019**, *73* (4), 943–951.

[19] Feng, X.; Hempenius, M. A.; Vancso, G. J. Metal Nanoparticle Foundry with Redox Responsive Hydrogels. *Macromol. Chem. Phys.* **2018**, *219* (22), 1800223.

[20] Astruc, D. Why Is Ferrocene so Exceptional? *Eur. J. Inorg. Chem*. **2017**, *2017* (1), 6–29.

[21] Ciganda, R.; Gu, H.; Hernandez, R.; Escobar, A.; Martínez, A.; Yates, L.; Moya, S.; Ruiz, J.; Astruc, D. Electrostatic Assembly of Functional and Macromolecular Ferricinium Chloride-Stabilized Gold Nanoparticles. *Inorg. Chem.* **2017**, *56* (5), 2784–2791.

[22] Wang, Q.; Fu, F.; Martinez-Villacorta, A. M.; Moya, S.; Salmon, L.; Vax, A.; Hunel, J.; Ruiz, J.; Astruc, D. Electron Flow in Large Metallomacromolecules and Electronic Switching of Nanoparticle Stabilization: Click Ferrocenyl Dentromers That Reduce Au ^{III} to Au Nanoparticles. *Chem. Eur. J.* **2018**, *24* (48), 12686–12694.

[23] Rapakousiou, A.; Deraedt, C.; Irigoyen, J.; Wang, Y.; Pinaud, N.; Salmon, L.; Ruiz, J.; Moya, S.; Astruc, D. Synthesis and Redox Activity of "Clicked" Triazolylbiferrocenyl Polymers, Network Encapsulation of Gold and Silver Nanoparticles and Anion Sensing. *Inorg. Chem.* **2015**, *54* (5), 2284–2299.

[24] Liu, X.; Liu, F.; Astruc, D.; Lin, W.; Gu, H. Highly-Branched Amphiphilic Organometallic Dendronized Diblock Copolymer: ROMP Synthesis, Self-Assembly and Long-Term Au and Ag Nanoparticle Stabilizer for High-Efficiency Catalysis. *Polymer* **2019**, *173*, 1-10.

[25] Rapakousiou, A.; Deraedt, C.; Gu, H.; Salmon, L.; Belin, C.; Ruiz, J.; Astruc, D. Mixed-Valent Click Intertwined Polymer Units Containing Biferrocenium Chloride Side Chains Form Nanosnakes That Encapsulate Gold Nanoparticles. *J. Am. Chem. Soc.* **2014**, *136* (40), 13995–13998.

[26] Bellas, V.; Rehahn, M. Polyferrocenylsilane-Based Polymer Systems. *Angew. Chem. Int. Ed.* **2007**, *46* (27), 5082–5104.

[27] Hempenius, M. A.; Cirmi, C.; Savio, F. L.; Song, J.; Vancso, G. J. Poly(Ferrocenylsilane) Gels and Hydrogels with Redox-Controlled Actuation. *Macromol. Rapid Commun.* **2010**, *31* (9–10), 772–783.

[28] Whittell, G. R.; Hager, M. D.; Schubert, U. S.; Manners, I. Functional Soft Materials from Metallopolymers and Metallosupramolecular Polymers. *Nat. Mater.* **2011**, *10* (3), 176–188.

[29] Wang, H.; Wang, X.; Winnik, M. A.; Manners, I. Redox-Mediated Synthesis and Encapsulation of Inorganic Nanoparticles in Shell-Cross-Linked Cylindrical Polyferrocenylsilane Block Copolymer Micelles. *J. Am. Chem. Soc.* **2008**, *130* (39), 12921–12930.

[30] Wang, X.-S.; Wang, H.; Coombs, N.; Winnik, M. A.; Manners, I. Redox-Induced Synthesis and Encapsulation of Metal Nanoparticles in Shell-Cross-Linked Organometallic Nanotubes. *J. Am. Chem. Soc.* **2005**, *127* (25), 8924–8925.

[31] Qiu, H.; Du, V. A.; Winnik, M. A.; Manners, I. Branched Cylindrical Micelles via Crystallization-Driven Self-Assembly. *J. Am. Chem. Soc.* **2013**, *135* (47), 17739–17742.

[32] Song, J.; Tan, Y. N.; Jańczewski, D.; Hempenius, M. A.; Xu, J. W.; Tan, H. R.; Vancso, G. J. Poly(Ferrocenylsilane) Electrolytes as a Gold Nanoparticle Foundry: "Two-in-One" Redox Synthesis and Electrosteric Stabilization, and Sensing Applications. *Nanoscale* **2017**, *9* (48), 19255–19262.

[33] Marcelo, G.; Fernández-García, M. Direct Preparation of PNIPAM Coating Gold Nanoparticles by Catechol Redox and Surface Adhesion Chemistry. *RSC Adv.* **2014**, *4* (23), 11740–11749.
[34] Watson, K. J.; Zhu, J.; Nguyen, S. T.; Mirkin, C. A. Redox-Active Polymer-Nanoparticle Hybrid Materials. *Pure and Applied Chemistry* **2000**, *72* (1–2), 67–72.
[35] Crooks, R. M.; Zhao, M.; Sun, L.; Chechik, V.; Yeung, L. K. Dendrimer-Encapsulated Metal Nanoparticles: Synthesis, Characterization, and Applications to Catalysis. *Acc. Chem. Res.* **2001**, *34* (3), 181–190.
[36] Hempenius, M. A.; Brito, F. F.; Vancso, G. J. Synthesis and Characterization of Anionic and Cationic Poly(Ferrocenylsilane) Polyelectrolytes. *Macromolecules* **2003**, *36* (17), 6683–6688.
[37] Sui, X.; Feng, X.; Di Luca, A.; van Blitterswijk, C. A.; Moroni, L.; Hempenius, M. A.; Vancso, G. J. Poly(N-Isopropylacrylamide)–Poly(Ferrocenylsilane) Dual-Responsive Hydrogels: Synthesis, Characterization and Antimicrobial Applications. *Polym. Chem.* **2013**, *4* (2), 337–342.
[38] Loh, N. D.; Sen, S.; Bosman, M.; Tan, S. F.; Zhong, J.; Nijhuis, C. A.; Král, P.; Matsudaira, P.; Mirsaidov, U. Multistep Nucleation of Nanocrystals in Aqueous Solution. *Nat. Chem.* **2017**, *9* (1), 77–82.
[39] Marin, M. L.; McGilvray, K. L.; Scaiano, J. C. Photochemical Strategies for the Synthesis of Gold Nanoparticles from Au(III) and Au(I) Using Photoinduced Free Radical Generation. *J. Am. Chem. Soc.* **2008**, *130* (49), 16572–16584.
[40] McGilvray, K. L.; Decan, M. R.; Wang, D.; Scaiano, J. C. Facile Photochemical Synthesis of Unprotected Aqueous Gold Nanoparticles. *J. Am. Chem. Soc.* **2006**, *128* (50), 15980–15981.
[41] Ohara, Y.; Akazawa, K.; Shibata, K.; Hirota, T.; Kodama, Y.; Amemiya, T.; Wang, J.; Yamaguchi, T. Seed-Mediated Gold Nanoparticle Synthesis via Photochemical Reaction of Benzoquinone. *Colloids and Surfaces A: Physicochemical and Engineering Aspects* **2020**, *586*, 124209.
[42] Scaiano, J. C.; Billone, P.; Gonzalez, C. M.; Marett, L.; Marin, M. L.; McGilvray, K. L.; Yuan, N. Photochemical Routes to Silver and Gold Nanoparticles. *Pure and Applied Chemistry* **2009**, *81* (4), 635–647.
[43] Zhang, K.; Feng, X.; Ye, C.; Hempenius, M. A.; Vancso, G. J. Hydrogels with a Memory: Dual-Responsive, Organometallic Poly(Ionic Liquid)s with Hysteretic Volume-Phase Transition. *J. Am. Chem. Soc.* **2017**, *139* (29), 10029–10035.
[44] Fairbanks, B. D.; Schwartz, M. P.; Bowman, C. N.; Anseth, K. S. PhotoinitiatedPolymerization of PEG-Diacrylate with Lithium Phenyl-2,4,6-Trimethylbenzoylphosphinate: Polymerization Rate and Cytocompatibility. *Biomaterials* **2009**, *30*, 6702–6707.

6.5 Supporting Information

Uv-vis spectra:

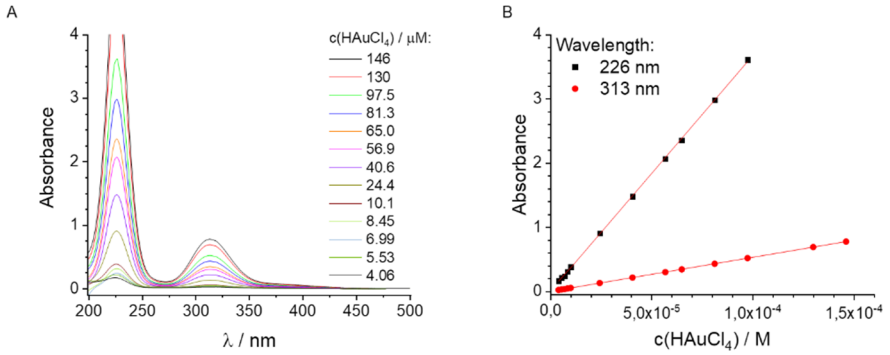

Figure S6.1 Calibration series of UV-Vis measurements with different concentrations of $HAuCl_4$ at pH = 1.1 (**A**). Linear fits of peak absorbance values at the two peaks characteristic of the $AuCl_4^-$ anion at acidic pH (**B**).

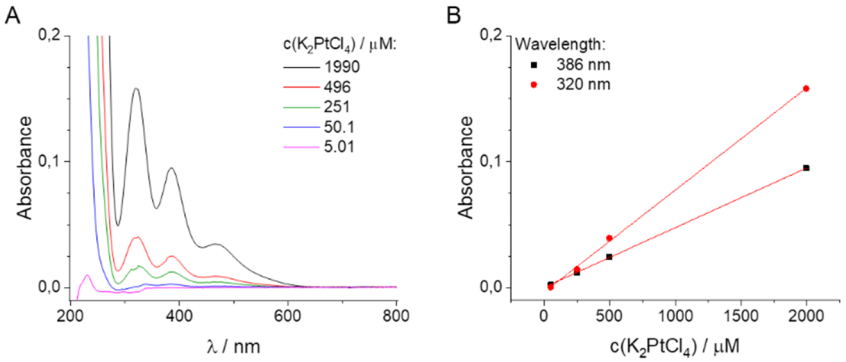

Figure S6.2 Calibration series of UV-Vis measurements with different concentrations of K_2PtCl_4 (**A**). Linear fits of peak absorbance values at the two peaks characteristic of the $PtCl_4^{2-}$ anion (**B**).

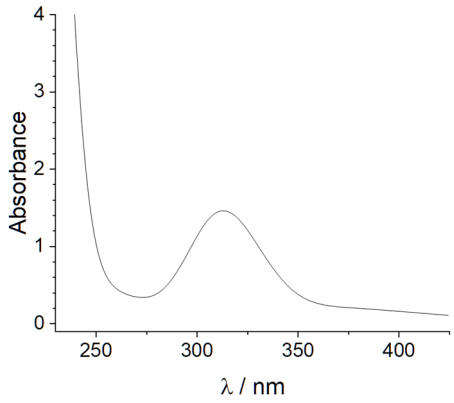

Figure S6.3 UV-Vis spectrum of $HAuCl_4$ electrolyte (c_0=1.21 mM, same as the 15.5x sample in Figure 6.3 of the main text) after immersion of PFS-free PNIPAM hydrogel into the solution. The sample was left in the dark for 3 days. Final concentration of $AuCl_4^-$ was measured to be 1.10 mM (8.9 % change vs 56.8 % measured in presence of PFS).

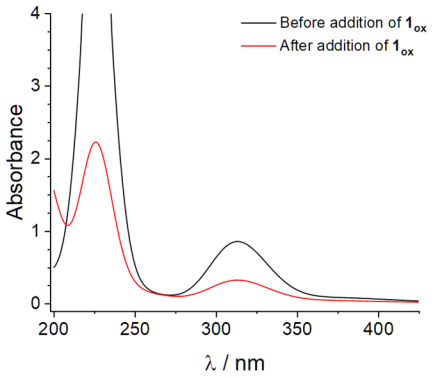

Figure S6.4 UV-Vis spectra of $HAuCl_4$ solutions before and after the addition of pre-oxidized PNIPAM/PFS hydrogel.

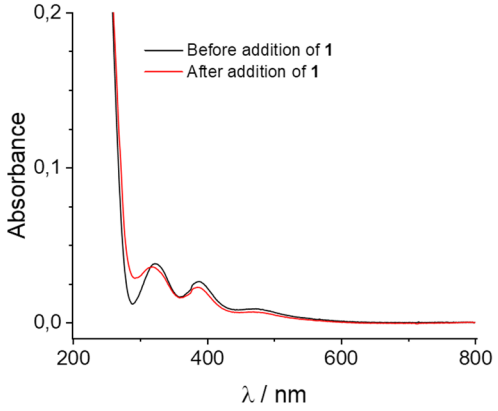

Figure S6.5 Results of Pt nanoparticle synthesis experiments with a hydrogel sample of **1** immersed in a solution containing 15.4x stoichiometric amount of K_2PtCl_4.

XPS

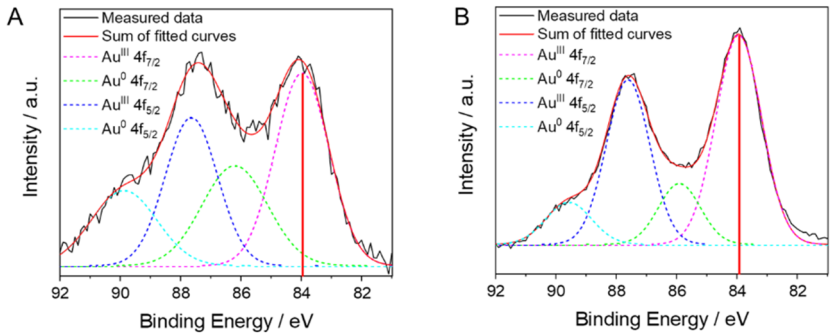

Figure S6.6 XPS results on dried hydrogel samples of **1** after immersion in 15.5x stoichiometric ratio $HAuCl_4$ solution after 24 h (A) and 72 h (B) immersion of the hydrogel. The oxidation state of gold atoms is similar measured with XPS and UV-Vis in both samples (A: 58.6 % Au^0 with XPS, 66.2 % with UV-Vis; B: 73.3 % vs 79.0 %).

Chapter 7

Outlook: New Applications Based on the Au-Thiolate Interaction

In this outlook section, we first introduce a new sulfur-containing derivative of PFS. We then show applications in printing patterns, to obtain gold nanoparticle assembly, and fabricate self-healing nanocomposite gels. As this is an outlook Chapter, the latter two applications need more in-depth studies.

Parts of this Chapter have been published as: Marco Cirelli, Jinmeng Hao, T.C. Bor, Joost Duvigneau, Niels Benson, R. Akkerman, Mark A. Hempenius and G. Julius Vancso, Printing "smart" Inks of Redox-Responsive Organometallic Polymers on Microelectrode Arrays for Molecular Sensing. *ACS Applied Materials & Interfaces* **2019**, *11*, 37060-37068.

Self-assembled monolayers (SAMs) of thiolates on flat gold surfaces have been extensively studied in the past 35 years owing to their application potential in molecular electronics,[1] electrochemistry,[2] and biochemistry.[3] In particular, in earlier work on SAMs, *n*-alkanethiolates were the main class of thiolates used on gold surfaces due to their excellent bonding affinity between sulfur and gold by the formation of a gold–sulfur bond[4] and the undemanding conditions required for their attachment to gold substrates and gold nanoparticles (AuNPs). The use of thiols in AuNP preparation enables the synthesis of very small gold particles, or clusters.[5]

Including thiols into polymers, especially responsive polymers, has taken SAM applications to another level. The thiols in polymers can work as highly reactive anchor for gold surfaces and for various cross-linking agents, forming stable three-dimensional networks. For example, Keerati et al.[6] prepared thiol-terminated thermo-responsive polymers which were further used to modify AuNPs by Au–S bonds. The modified AuNPs possessed thermo-responsive behavior with color change from red to blue-purple without precipitation when the solution was heated above the lower critical solution temperature (LCST).

Poly(ferrocenylsilane)s, PFSs, represent one of the most developed classes of metallopolymers. These polymers possess a main chain consisting of alternating ferrocene units and substituted silicon atoms.[7–9] In PFSs the silane units have been employed for substitution chemistry, yielding a broad range of functional macromolecules. The variations of the side group structure allow one to tune the physical and chemical properties of PFSs, while the ferrocene units are responsible for the redox activity. Various sulfur-containing PFS macromolecules have been prepared and reported previously. For example, end-capping of living PFS chains with ethylene sulfide provided access to thiol end-functionalized PFSs.[10]

In this outlook Chapter, a PFS random copolymer possessing a tailored amount of reactive halopropyl side groups is described that was obtained via platinum catalyzed ring opening polymerization of silicon-bridged ferrocenophanes. Then, disulfide moieties were attached to the haloalkyl groups by nucleophilic substitution to afford disulfide-functionalized PFSs with a well-controlled composition capable to covalently graft to gold surfaces (polymer structure is shown in Figure 7.1).

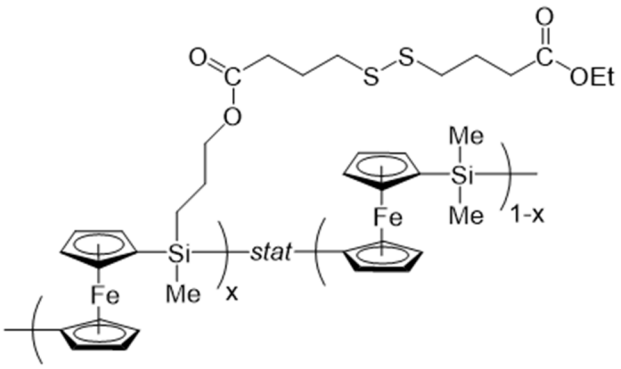

Figure 7.1 Structure of the disulfide functionalized poly(ferrocenylsilane) copolymer.

Based on the Au-thiolate interaction, the potential applications of the thiolated PFS including printing redox-responsive PFS on microelectrode arrays for molecular sensing, self-assembly of AuNPs, and the fabrication of self-healing nanocomposite hydrogels are proposed and discussed.

7.1 Printing "Smart" Inks of Redox-Responsive Organometallic Polymers on Microelectrode Arrays for Molecular Sensing

Microelectrode arrays (MEAs) allow one to perform multiplexed parallel analysis of complex mixtures of redox-active analytes with selective and specific sensing of the individual constituents in the microelectrode cells that make up the array.[11] For a successful implementation of such devices one could consider selective printing of specific sensing molecular inks into the individual microelectrode cells (MEs) that can exhibit a different composition from "pixel" to "pixel" within the array.[12] The recognition inks should adhere to the ME surface and provide analyte selective signals. Printing using multiple reservoirs would be needed to render each electrochemical microcell working as a specific sensing element. Toward achieving this objective, we describe in this Chapter the first necessary steps including (a) the development of a novel redox-responsive molecular ink and (b) the construction of single ME sensing "pixels" using one printing reservoir and a single nozzle. The

redox-responsive polymers feature a poly(ferrocenylsilane) (PFS) backbone and side groups with disulfide units that allow an efficient and stable bonding to Au substrates, relying on sulfur-gold chemistry using a "grafting-to" approach. These molecules can then be employed for area selective molecular sensing following deposition by high precision inkjet printing.

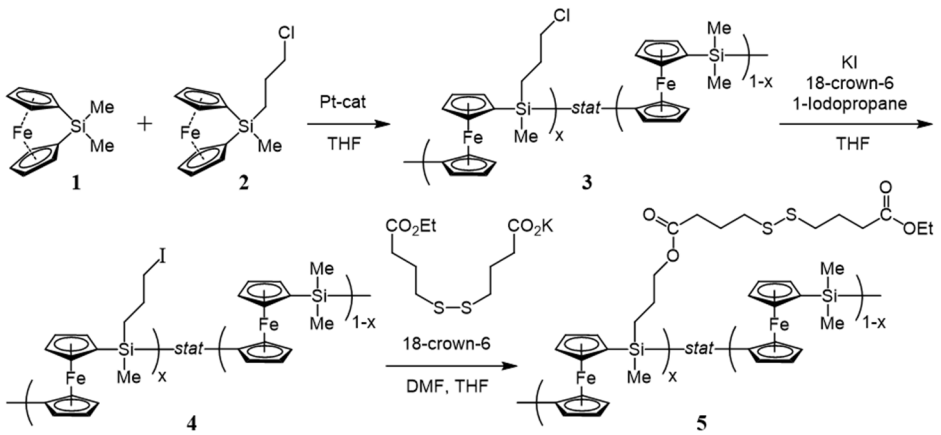

Figure 7.2 Synthesis of disulfide-functionalized PFS **5**.

This tholated PFS-based random copolymer was designed to possess a tailored number of disulfide moieties to ensure a stable covalent attachment of the polymer to the gold surface. Disulfide modified poly(ferrocenylsilane) random copolymers were prepared in three steps, starting with the transition metal-catalyzed ring opening polymerization (ROP) of [1]dimethylsilaferrocenophane **1** and [1](3-chloropropyl)methylsilaferrocenophane **2** to afford PFS **3** (Figure 7.2). The chloropropyl moieties introduced by copolymerization of **1** with ferrocenophane **2** enable further derivatization of the formed PFS chains by nucleophilic substitution, in this work by their conversion into more reactive iodopropyl groups, yielding PFS **4**. Reaction of PFS **4** with the potassium salt of 4,4-dithiobutyric acid monoethyl ester led to disulfide-functionalized PFS **5**. As transition metal catalyzed random copolymerization of ferrocenphanes has been demonstrated before, we anticipated that the presence of 5 mol% ferrocenphanes **2** in the monomer mixture would lead to incorporation of a corresponding amount of disulfide groups along the PFS chains.

Toluene-based inks with 2.5 wt% PFS **5** was used for printing, as it provides good rheological properties (with shear viscosity of 1.8 mPa·s), ideal printability (i.e.,

stable, no satellite drops, repeatable droplet formation), accurate deposition, and a long-time storage stability (i.e., the physical and chemical ink properties were stable for more than 6 months). In addition, since it has the lowest concentration of PFS **5** required to obtain a printable ink, it also allows for the deposition of the lowest amount of PFS **5** per drop, eventually enhancing control over the deposited layer thickness. In fact, as shown in Figure 7.3a from the high-speed image collection, the ink developed a stable jet with drop volumes of about 10 pL and a velocity of 5 m s^{-1} by using the simple actuator waveform as depicted in Figure 7.3b. No satellite droplets formed during printing, and a good accuracy and precision with a misalignment of <0.26° were obtained, as shown in Figure 7.3c.

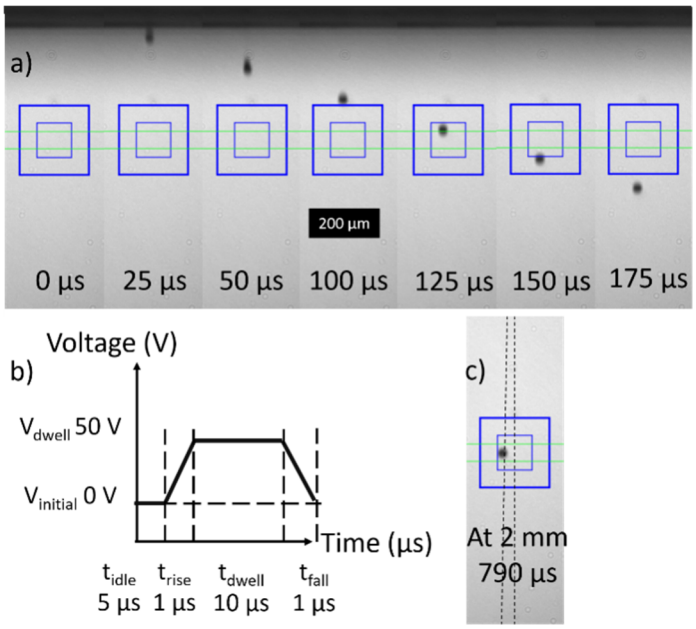

Figure 7.3 a) Series of high-speed photographic images of ink A as it is ejected from the nozzle at times between 0 to 175 µs after the start of the piezo actuation. Characteristics of the drop: speed 5 m/s and volume 10 pL. **b**) The piezoelectric actuator waveform used for a stable drop-on-demand inkjet printing of ink A. **c**) High-speed photographic image recorded at a distance of 2 mm from the nozzle which corresponds to the distance between the print-head and the MEA substrate during the deposition of the ink, revealing a misalignment of 0.26°.

EDX analysis confirmed the presence of Fe and Si in equal atomic percentages after deposition of PFS **5** ink on the MEs, as is shown in the inset of the SEM images in Figure 7.4a and 7.4c. The presence of sulfur was not observed with EDX analysis since its concentration was below the sensitivity of the instrument. Conclusive confirmation of the successful ME surface modification was obtained by cyclic voltammetry (CV) measurements on the PFS **5** decorated MEs. As shown in Figure 7.4b and 7.4d, the characteristic oxidation and reduction peaks of the ferrocene moieties of PFS (between −100 and 400 mV versus Pt electrode) are clearly present for the modified electrodes, while no current was observed for the non-modified MEs. The double-wave voltammogram, typical of PFS, indicates p-π d- π electron overlap due to electronic delocalization between neighboring ferrocene units in the polymer via the Si bridge.[13,14]

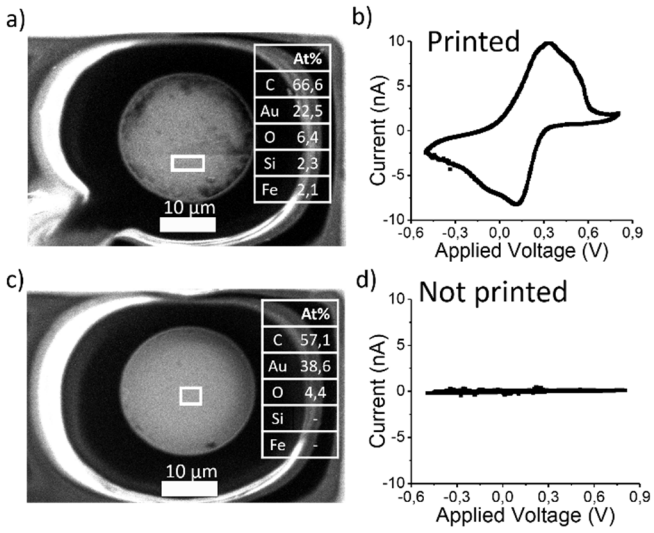

Figure 7.4 Surface characterization of the MEs via SEM-EDX: (**a**) and (**c**) SEM images of PFS **5** modified and bare gold electrodes of the MEA, respectively. The insets show the elemental composition of the areas in the rectangular white boxes. (**b**) and **d**) CVs of a PFS **5** modified and bare electrode of the MEA, respectively. Scan rate 50 mV s^{-1}, in 100 mM $NaClO_4$, Pt(wire)-RE/CE, and potential range between −500 and 800 mV vs. Pt.

To confirm the stability of deposited PFS **5** films on the ME, successive CV measurements were conducted. For comparison, repeated CV measurements were performed for deposited films of iodine-functionalized PFS (PFS **4**). Figure 7.5 shows the CVs for PFS **5** (a) and PFS **4** (b) layers on gold electrodes. From Figure 7.5 it is clear that for PFS **5** films the oxidation and reduction peaks remained unchanged and are reproducible for more than 10 potential cycles, indicating that no PFS chains desorb from the substrate. On the other hand, as shown in Figure 7.5b, the oxidation and reduction currents for PFS **4** films decreased after each CV, indicating the gradual desorption of the iodopropyl-functionalized PFS **4** from the Au-ME. Hence, the introduction of a disulfide functionality along the PFS backbone is a necessity to significantly enhance the printed layer stability on gold electrodes.

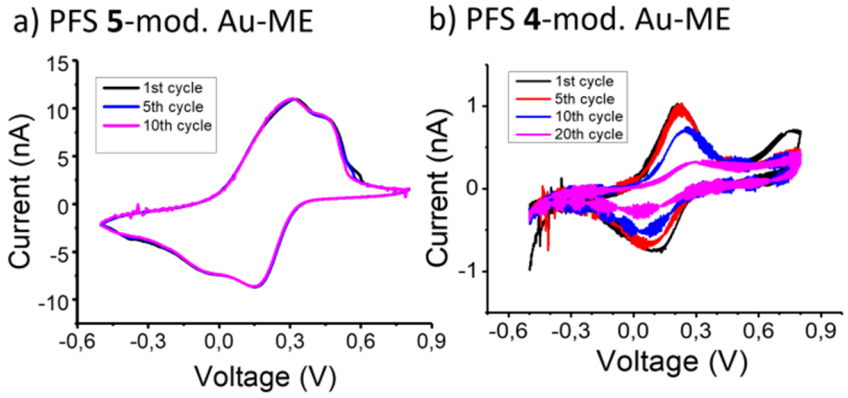

Figure 7.5 Evaluation of the electrochemical stability of printed surface-tethered PFS **5** layers printed on gold electrodes of the MEA by repeated CV measurements. Scan rate 50 mV s^{-1}, in 100 mM $NaClO_4$, Pt(wire)-RE/CE, and potential range between −500 and 800 mV vs. Pt.

Finally, the potential of these devices to act as an electrochemical sensor array was demonstrated with a model analyte, ascorbic acid, by using cyclic voltammetry and amperometric measurements. Good sensitivity and stable responses to ascorbic acid were achieved. We note that the polymer, developed and described in this Chapter, was used for detailed printing studies by Marco Cirelli (Thesis ISBN: 978-90-365-4931-8).

7.2 Self-Assembled Gold Nanoparticles Enabled by Poly(ferrocenylsilane)s

Gold nanoparticles (AuNPs) have attracted considerable interest due to their multiple applications in nanoelectronics, optics, nanomedicine, and catalysis depending on their size, shape and capping agent.[15] Well-defined clusters of NPs provide additional versatility and levels of control in the design of NP-based functional materials, which have drawn attraction in recent years because of the opportunity to access collective properties that are different from those of individual NPs.[16–19] Self-assembly enables the organization of NPs into nanostructures with increasingly complex architectures, which exhibit new collective optical,[19] magnetic,[20] or electronic properties[16] due to the coupling of properties of individual NPs. For instance, when an individual AuNP assembles with adjacent NPs, the near field of one particle interacts with the adjacent NPs in close proximity, resulting in the oscillating electrons in the NPs to be coupled together and forming a new coupled plasmon resonance. The self-assembly of AuNPs can be realized by numerous interactions including van der Waals attraction, Coulombic and magnetic forces, steric repulsion, capillary forces etc.[21,22,23] Thiolated PFS (see Figure 7.1) may be good candidate for simultaneous AuNP synthesis and assembly, owing to the suitably matching redox potentials of ferrocenes and Au^{III} precursors and the presence of disulfide groups as anchors for assembling.

Here we use a biphasic (toluene/water) procedure for the synthesis and self-assembly of AuNPs (Figure 7.6) that involves only two components, namely $HAuCl_4$ dissolved in water and PFS **5** in toluene. The biphasic reaction of PFS **5** with $HAuCl_4$ occurs slowly at the interface at room temperature with the aqueous solution changing from light yellow to purple. Transmission electron microscopy (TEM) images show an average individual spherical AuNP core size of 25 nm and assembled AuNP cluster size of 200 nm (Figure 7.7). The reaction stoichiometry corresponds to the reduction of Au^{III} to Au^0, whereas the Fe oxidation state in the ferrocene units increases from II to III. Meanwhile, PFS **5** works as macromolecular crosslinker by the formation of coordination bonds between disulfide side groups and the AuNP surface. However, the aggregated clusters did not show spherical shapes due to the rather rigid chain structure of PFS. As shown in UV-Vis spectra (Figure 7.8), the size

of the AuNP aggregates can be systematically adjusted by changing the concentration of PFS **5**.

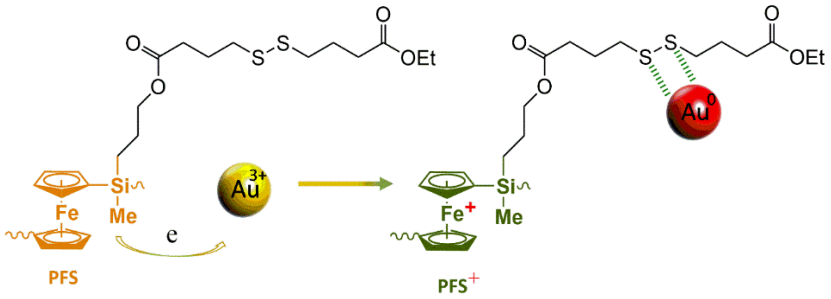

Figure 7.6 Formation and assembly of AuNPs upon reaction of PFS **5** with $HAuCl_4$.

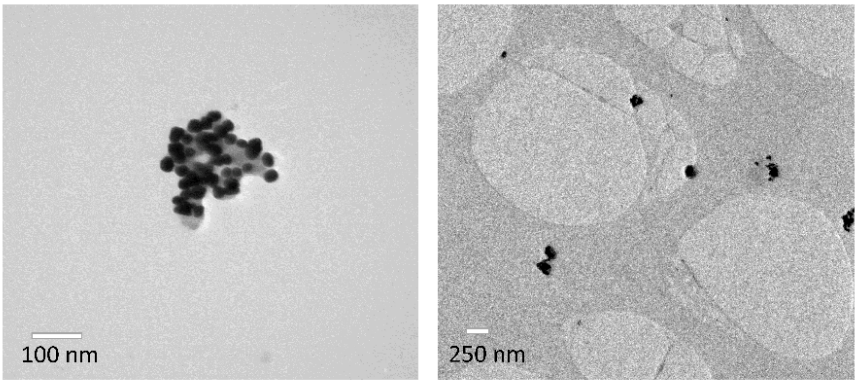

Figure 7.7 TEM images of assembled AuNPs with 120 μM PFS **5**.

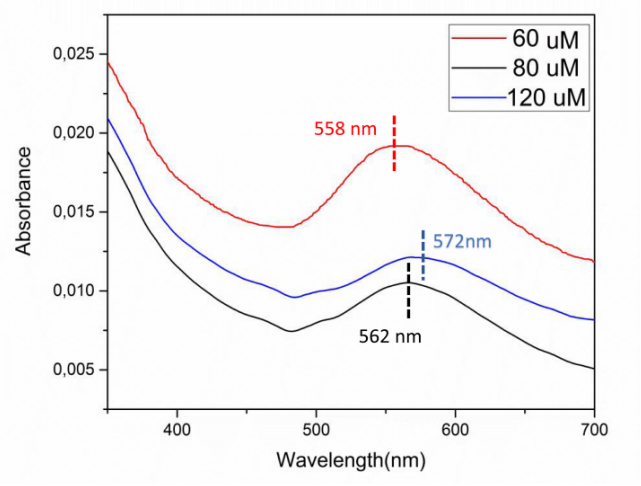

Figure 7.8 UV-Vis absorption spectra of AuNPs synthesized and assembled with PFS **5** of different concentrations.

We note that AuNP aggregate, stabilized by PFS shells and their redox driven assembly can be used as optical sensors.[24]

7.3 Self-Healing Nanocomposite Gels Based on Au-Thiolate Interaction

Interest in synthetic self-healing hydrogels has developed rapidly because of their ability to repair structural damage and recover their original functions. For fast defect healing, incorporation of healing agents or strong and dynamic interactions between polymer chains and crosslinkinkers as healing motifs is required. Most reported self-healing hydrogels are crosslinked with sacrificial bonds like hydrogen bonds and van der Waals forces, which lead to weak mechanical performance.[24–26] Recently, coordination interactions with tunable thermodynamics and high kinetic constant values have been widely used as effective healing motifs for self-healing materials.[28,29] Based on the dynamic Au-thiolate interaction, thiolated PFS (PFS **5**) can be used to crosslink AuNPs for tough and self-healing gels.[30] In addition, other metals like silver can also be used to construct functional self-healing nanocomposite gels.[30]

Here, gels synthesized with pre-prepared AuNPs and PFS **5** are shown in Figure 7.9. The AuNPs act as crosslinkers by forming Au-disulfide coordination bonds, enabling the formation of a gel network. The gels can possibly be healed by means of heating after damage, due to the general principle that elevated temperatures are an effective way to induce dynamic bonding of ligands to surfaces, by on/off switching the ligands from the surface.[30] Due to the plasmonic heating effects of AuNPs, the gels can possibly display rapid self-healing characteristics under light irradiation.[18,32,34]

Figure 7.9 Image of the nanocomposite gel.

We note that this is only a preliminary observation and detailed studies are needed to prove the utility of the gels for efficient self-healing applications.

7.4 Experimental Section

Printing "Smart" Inks of Redox-Responsive Organometallic Polymers on Microelectrode Arrays for Molecular Sensing

Materials: [1]Dimethylsilaferrocenophane 1 and ([1]3-chloropropyl)methylsilaferrocenophane 2 were synthesized according to published procedures.[36] 4,4′-Dithiodibutyric acid (DTDB, 95%), iodoethane (99%), 1-iodopropane (99%), hydrogen hexachloroplatinate(IV) hydrate ($H_2PtCl_6 \cdot 6H_2O$, 99.9+%), dicyclohexano-18-crown-6 (98%), potassium iodide (KI, 99+%), sodium chloride (NaCl), sodium sulphate (Na_2SO_4, anhydrous, 99%), chloroform-d ($CDCl_3$, 99.8 atom % D), toluene-d8 (99.6 atom % D) were obtained from Sigma-Aldrich Chemie GmbH (Steinheim, Germany) and used as received. For the electrochemistry experiments, sodium perchlorate ($NaClO_4$, ACS Reagent, >98.0%) and L-ascorbic acid (ACS Reagent, 99+%) were obtained from Sigma-Aldrich Chemie GmbH

(Steinheim, Germany) and used as received. Toluene, dimethylformamide (DMF), dimethyl sulfoxide (DMSO), tetrahydrofuran (THF), ethanol (EtOH) and methanol (MeOH), all of AR grade, were obtained from Biosolve Chimie SARL (Dieuze, France) and Milli-Q grade water (Millipore Corporation) was used in all the experiments.

Synthesis of 4,4′-Dithiodibutyric Acid Monoethyl Ester: 4,4′-Dithiodibutyric acid (DTDB) was alkylated following a published procedure.[35] A suspension of powdered potassium hydroxide 85% (1.33 g, 20 mmol) in DMSO (13 mL) was stirred vigorously for 30 min at room temperature. A solution of DTDB (2.384 g, 9.5 mmol) was added in DMSO (10 mL), and the mixture was stirred for 15 min. After cooling in an ice–water bath, a solution of iodoethane (2.23 g, 14.3 mmol) in DMSO (20 mL) was added by using a dropping funnel. Stirring was continued for 2 h at room temperature, followed by the addition of ice–water (150 mL). The pH value of the mixture was adjusted to pH 3–4 with dilute hydrochloric acid. The resulting solution was extracted three times with ethyl acetate (3 × 15 mL), and the organic layer was washed three times with saturated aqueous sodium chloride (3 × 15 mL). The solution was dried over anhydrous sodium sulfate and concentrated under reduced pressure. Purification was performed by column chromatography using *n*-hexane/acetone (1:1 vol:vol) as eluent to obtain 1.27 g (4.77 mmol) of product. Yield: 50.2%.

*Synthesis of Chloropropyl-Functionalized PFS **3**:* In a glovebox filled with prepurified N_2, [1]dimethylsilaferrocenophane 1 (1.40 g, 5.78×10^{-3} mol) and [1](3-chloropropyl)methylsilaferrocenophane 2 (93 mg, 3.05×10^{-4} mol, 5 mol %) were dissolved in dry THF (20 mL) in a 50 mL one-necked round-bottom flask. A small grain of hexachloroplatinic acid (5 mg) was added under stirring according to a well-established procedure.[36,37] Stirring was continued for 36 h. The solution was then diluted by adding THF (10 mL), and the polymer was precipitated in MeOH (200 mL). This mixture was stirred for 1 h to coagulate the polymer. After the polymer was isolated, it was precipitated again in MeOH, dried in a flow of N_2, and further dried under vacuum. Yield: 1.40 g.

*Synthesis of Iodopropyl-Functionalized PFS **4**:* PFS **3** (1.30 g) was dissolved in THF (40 mL) and dicyclohexano-18-crown-6 (1.0 g, 2.7 mmol), KI (1.0 g, 6.0 mmol), and 1-iodopropane (3 mL, 31 mmol) were added. The reaction mixture was stirred at

40 °C for 2 weeks. Following a week, some iodopropane (2 mL) was added. The polymer was precipitated twice in MeOH (200 mL), dried in a flow of N_2, and further dried under vacuum. Yield: 1.35 g.

*Synthesis of Disulfide-Functionalized PFS **5**:* 4,4-Dithiodibutyric acid monoethyl ester (0.352 g, 1.32 mmol), dicyclohexano-18-crown-6 (0.50 g, 1.34 mmol), and K_2CO_3 (0.174 g, 1.26 mmol) were dissolved in DMF (10 mL) in a 25 mL round-bottom flask under N_2. After stirring for 2 h, the solution was taken up in a syringe and added to a solution of PFS **4** (1.129 g) in THF (20 mL), which was also kept under a nitrogen atmosphere. The flask containing the 4,4-dithiodibutyric acid monoethyl ester was rinsed twice with DMF (2 mL), which was also transferred by syringe to the PFS solution. The reaction mixture was stirred for 1 week at 20 °C and then added dropwise to methanol (200 mL) to precipitate the polymer. The polymer was precipitated again from THF (20 mL) into MeOH (200 mL), dried in a flow of N_2, and further dried under vacuum (6 mbar, 24 h, followed by 1×10^{-3} mbar, 24 h). Yield: 1.13 g.

Characterization: ^{1}H and ^{13}C NMR spectra were obtained on a Bruker Avance III 400 MHz instrument at 400.1 and 100.6 MHz, respectively. The microelectrode array, MEA, biochips used in this experiment were MEA 60-200Au (Qwane Biosciences SA, Switzerland) characterized by 60 plain gold electrodes, each with 40 µm diameter, a center-to-center spacing of 200 µm, with an insulator layer of SU-8 with a thickness of 0.7 µm, and an impedance of 700–900 kΩ positioned on a transparent 10 mm x 10 mm glass chip. SEM images and EDX were taken with a high-resolution scanning electron microscopy instrument (FESEM, JEOL, JSM-6400F, the Netherlands) at 5 and 20 keV of accelerating voltage, equipped with an energy dispersive X-Ray analyzer. Cyclic voltammetry (CV) measurements were performed with an Autolab PGSTAT 10.

Self-Assembled Gold Nanoparticles Enabled by Disulfide-functionalized Poly(ferrocenylsilane)s

Materials: Gold(III) chloride trihydrate (99.9% purity) was purchased from Sigma Aldrich. The PFS **5** used here possessed 100% disulfide side groups.

Synthesis of assembled AuNPs: The AuNPs were synthesized in a toluene/water biphasic mixture without stirring. Briefly, a freshly prepared $HAuCl_4$ solution was made by adding $HAuCl_4 \cdot 3H_2O$ (0.003 mmol) to 3 mL of water. In the same flask, PFS **5** (0.0006, 0.00048, 0.0003 mmol) dissolved in 5 mL of toluene was added into the solution at room temperature and incubated for 3 days. The color of the aqueous solution gradually changed from light yellow to purple, due to the formation and assembly of AuNPs. Meanwhile, the color of the toluene solution changed from orange-yellow to colorless.

Characterization: UV-Vis absorption spectra were recorded with a Perkin-Elmer Lambda 850 UV-vis spectrometer. Transmission Electron Microscopy (TEM) images were taken using a high-resolution transmission electron microscopy (TEM, Philips CM300ST–FEG). The TEM samples were prepared by deposition of the nanoparticle suspension (10 μL) onto a carbon-coated microscopy copper grid.

Self-Healing Nanocomposite Gels Based on Au-Thiolate Interactions

Materials: Tetraoctylammonium bromide (98%), sodium borohydride (≥98.0%), 1-dodecanethiol (98% purity) were purchased from Sigma Aldrich.

Synthesis of AuNPs: Nanoparticles were prepared using the method described by Brust et al.[38] using a *n*-dodecanethiol to gold ratio of 3:1. The AuNPs were then dispersed in THF, resulting in a 3 mg/mL solution.

Synthesis of Nanocomposite Gels: Desired amounts of PFS **5** were added to the AuNP solution and incubated at room temperature for 24 h. The gels were then swelled in THF.

References

[1] Inkpen, M. S.; Liu, Z. F; Li, H.; Campos, L. M.; Neaton, J. B.; Venkataraman, L. Non-Chemisorbed Gold–Sulfur Binding Prevails in Self-Assembled Monolayers. *Nat. Chem.* **2019**, *11*, 351–358.

[2] Eckermann, A. L.; Feld, D. J.; Shaw, J. A.; Meade, T. J. Electrochemistry of Redox-Active Self-Assembled Monolayers. *Coord. Chem. Rev.* **2010**, *254*, 1769–1802.

[3] Sun, K.; Jiang, B.; Jiang, X. Electrochemical Desorption of Self-Assembled Monolayers and Its Applications in Surface Chemistry and Cell Biology. *J. Electroanal. Chem.* **2011**, *656*, 223–230.
[4] Weisshaar, D. E.; Walczak, M. M.; Porter, M. D. Electrochemically Induced Transformations of Monolayers Formed by Self-Assembly of Mercaptoethanol at Gold. *Langmuir* **1993**, *9*, 323–329.
[5] Badia, A.; Demers, L.; Dickinson, L.; Morin, F. G.; Lennox, R. B.; Reven, L. Gold-Sulfur Interactions in Alkylthiol Self-Assembled Monolayers Formed on Gold Nanoparticles Studied by Solid-State NMR. *J. Am. Chem. Soc.* **1997**, *119*, 11104–11105.
[6] Kusolkamabot, K.; Sae-Ung, P.; Niamnont, N.; Wongravee, K.; Sukwattanasinitt, M.; Hoven, V. P. Poly(N -Isopropylacrylamide)-Stabilized Gold Nanoparticles in Combination with Tricationic Branched Phenylene-Ethynylene Fluorophore for Protein Identification. *Langmuir* **2013**, *29*, 12317–12327.
[7] Hailes, R. L. N.; Oliver, A. M.; Gwyther, J.; Whittell, G. R.; Manners, I. Polyferrocenylsilanes: Synthesis, Properties, and Applications. *Chem. Soc. Rev.* **2016**, *45*, 5358–5407.
[8] Bellas, V.; Rehahn, M. Polyferrocenylsilane-Based Polymer Systems. *Angew. Chemie - Int. Ed.* **2007**, *46*, 5082–5104.
[9] Sui, X.; Feng, X.; Di Luca, A.; Van Blitterswijk, C. A.; Moroni, L.; Hempenius, M. A.; Vancso, G. J. Poly(N-Isopropylacrylamide)-Poly(Ferrocenylsilane) Dual-Responsive Hydrogels: Synthesis, Characterization and Antimicrobial Applications. *Polym. Chem.* **2013**, *4*, 337–342.
[10] Choueiri, R. M.; Klinkova, A.; Pearce, S.; Manners, I.; Kumacheva, E. Self-Assembly and Surface Patterning of Polyferrocenylsilane-Functionalized Gold Nanoparticles. *Macromol. Rapid Commun.* **2018**, *39*.
[11] Spira, M. E.; Hai, A. Multi-Electrode Array Technologies for Neuroscience and Cardiology. *Nat. Nanotechnol.* **2013**, *8*, 83–94.
[12] Huang, X. J.; O'Mahony, A. M.; Compton, R. G. Microelectrode Arrays for Electrochemistry: Approaches to Fabrication. *Small* **2009**, *5*, 776–788.
[13] Hailes, R. L. N.; Oliver, A. M.; Gwyther, J.; Whittell, G. R.; Manners, I. Polyferrocenylsilanes: Synthesis, Properties, and Applications. *Chem. Soc. Rev.* **2016**, *45*, 5358–5407.
[14] Cantini, E.; Wang, X.; Koelsch, P.; Preece, J. A.; Ma, J.; Mendes, P. M. Electrically Responsive Surfaces: Experimental and Theoretical Investigations. *Acc. Chem. Res.* **2016**, *49*, 1223–1231.
[15] Brust, M.; Fink, J.; Bethell, D.; Schiffrin, D. J.; Kiely, C. Synthesis and Reactions of Functionalised Gold Nanoparticles. *J. Chem. Soc. Chem. Commun.* **1995**, 16, 1655–1656.
[16] Guo, S.; Wang, E. Synthesis and Electrochemical Applications of Gold Nanoparticles. *Anal. Chim. Acta* **2007**, *598*, 181–192.

[17] Nagarajan, R. Nanoparticles: Building Blocks for Nanotechnology. *ACS Symp. Ser.* **2008**, *996*, 2–14.
[18] Abadeer, N. S.; Murphy, C. J. Recent Progress in Cancer Thermal Therapy Using Gold Nanoparticles. *J. Phys. Chem. C* **2016**, *120*, 4691–4716.
[19] Daniel, M. C. M.; Astruc, D. Gold Nanoparticles: Assembly, Supramolecular Chemistry, Quantum-Size Related Properties and Applications toward Biology, Catalysis and Nanotechnology. *Chem. Rev.* **2004**, *104*, 293–346.
[20] Lin, J.; Zhou, W.; Kumbhar, A.; Wiemann, J.; Fang, J.; Carpenter, E. E.; O'Connor, C. J. Gold-Coated Iron (Fe@Au) Nanoparticles: Synthesis, Characterization, and Magnetic Field-Induced Self-Assembly. *J. Solid State Chem.* **2001**, *159*, 26–31.
[21] Liu, Z.; Lanier, O. L.; Chauhan, A. Poly (Vinyl Alcohol) Assisted Synthesis and Anti- Solvent Precipitation of Gold Nanoparticles. *Nanomaterials* **2020**, *10*, 1–16.
[22] Daniel, M. C.; Astruc, D. Gold Nanoparticles: Assembly, Supramolecular Chemistry, Quantum-Size-Related Properties, and Applications Toward Biology, Catalysis, and Nanotechnology. *Chem. Rev.* **2004**, *104*, 293–346.
[23] Sardar, R.; Funston, A. M.; Mulvaney, P.; Murray, R. W. Gold Nanoparticles: Past, Present, and Future. *Langmuir* **2009**, *25*, 13840–13851.
[24] Song, J.; Tan, Y. N.; Jańczewski, D.; Hempenius, M. A.; Xu, J. W.; Tan, H. R.; Vancso, G. J. Poly(Ferrocenylsilane) Electrolytes as a Gold Nanoparticle Foundry: "Two-in-One" Redox Synthesis and Electrosteric Stabilization, and Sensing Applications. *Nanoscale* **2017**, *9*, 19255–19262.
[25] Nakahata, M.; Takashima, Y.; Yamaguchi, H.; Harada, A. Redox-Responsive Self-Healing Materials Formed from Hostĝ Guest Polymers. *Nat. Commun.* **2011**, *2*.
[26] Yuan, T.; Qu, X.; Cui, X.; Sun, J. Self-Healing and Recyclable Hydrogels Reinforced with in Situ Formed Organic Nanofibrils Exhibit Simultaneously Enhanced Mechanical Strength and Stretchability. *ACS Appl. Mater. Interfaces* **2019**, *11*, 32346–32353.
[27] Jiang, Z.; Diggle, B.; Shackleford, I. C. G.; Connal, L. A. Tough, Self-Healing Hydrogels Capable of Ultrafast Shape Changing. *Adv. Mater.* **2019**, *1904956*, 1–10.
[28] Yuan, T.; Cui, X.; Liu, X.; Qu, X.; Sun, J. Highly Tough, Stretchable, Self-Healing, and Recyclable Hydrogels Reinforced by in Situ-Formed Polyelectrolyte Complex Nanoparticles. *Macromolecules* **2019**, *52*, 3141–3149.
[29] Shi, S.; Peng, X.; Liu, T.; Chen, Y. N.; He, C.; Wang, H. Facile Preparation of Hydrogen-Bonded Supramolecular Polyvinyl Alcohol-Glycerol Gels with Excellent Thermoplasticity and Mechanical Properties. *Polymer (Guildf).* **2017**, *111*, 168–176.
[30] Qin, H.; Zhang, T.; Li, H. N.; Cong, H. P.; Antonietti, M.; Yu, S. H. Dynamic Au-Thiolate Interaction Induced Rapid Self-Healing Nanocomposite Hydrogels with Remarkable Mechanical Behaviors. *Chem* **2017**, *3*, 691–705.

[31] Qin, H.; Zhang, T.; Li, N.; Cong, H. P.; Yu, S. H. Anisotropic and Self-Healing Hydrogels with Multi-Responsive Actuating Capability. *Nat. Commun.* **2019**, *10*, 1–11.
[32] Klotz, I. M.; Campbell, B. J. Copper-Induced Hydrolysis of the Disulfide Bond. *Arch. Biochem. Biophys.* **1962**, *96*, 92–99.
[33] Hu, M.; Chen, J.; Li, Z. Y.; Au, L.; Hartland, G. V.; Li, X.; Marquez, M.; Xia, Y. Gold Nanostructures: Engineering Their Plasmonic Properties for Biomedical Applications. *Chem. Soc. Rev.* **2006**, *35*, 1084–1094.
[34] Zhang, H.; Koens, L.; Lauga, E.; Mourran, A.; Möller, M. A Light-Driven Microgel Rotor. *Small* **2019**, *1903379*, 1903379.
[35] Avila-Zárraga, J. G.; Martínez, R. Efficient Methylation of Carboxylic Acids with Potassium Hydroxide/Methyl Sulfoxide and Iodomethane. *Synth. Commun.* **2001**, *31*, 2177–2183.
[36] Gomez-elipe, P.; Macdonald, P. M.; Manners, I. Architectural Control in the Transition-Metal- Catalyzed Ring-Opening Polymerization. *Angew. Chemie - Int. Ed.* **2000**, *2100*, 762–764.
[37] Hempenius, M. A.; Brito, F. F.; Vancso, G. J. Synthesis and Characterization of Anionic and Cationic Poly(Ferrocenylsilane) Polyelectrolytes. *Macromolecules* **2003**, *36*, 6683–6688.
[38] Brust, M.; Walker, M.; Bethell, D.; Schiffrin, D. J.; Whyman, R. Synthesis of Thiol-Derivatised Gold Nanoparticles In a two-phase Liquid–liquid System. *Chemcomm*. **2000**, 7, 801–802.

7

Summary

This Thesis describes the design, synthesis and applications of a series of gold nanoparticle-stimuli-responsive hydrogel nanocomposites. PFSs are a fascinating class of redox-active metallopolymers with a backbone consisting of alternating redox-active ferrocene and organosilane units. PFS-based redox-responsive hydrogels are used as foundry for the in-situ formation of gold nanoparticles (AuNPs) in this Thesis. Taking advantage of the combination of a thermo-responsive PNIPAM hydrogel and the photothermal effect of the AuNPs, the deformation and surface morphology changes of the hydrogel composites can be controlled by both temperature and light irradiation. By designing different anisotropic hydrogel structures, a variety of applications including wrinkling bilayers and actuators are explored in this Thesis. Regarding stoichiometry investigations, we considered the electrochemical redox process during AuNP formation and offer a model explaining the source of the electrons in addition to ferrocene.

In **Chapter 1**, a general introduction to the topics related to the research are presented.

In **Chapter 2**, a literature review covering AuNPs, stimuli-responsive hydrogels, nanocomposite hydrogels and anisotropic hydrogels is provided. The utility of stimuli-responsive hydrogels in AuNP synthesis is highlighted. The structure design and applications of nanocomposite hydrogels, especially of AuNP/hydrogel nanocomposites, are introduced.

In **Chapter 3**, a bilayer consisting of a compliant poly(acrylamide) (PAAm) bottom layer and a rigid AuNP nanocomposite poly(*N*-isopropylacrylamide) (PNIPAM) PNIPAM/PFS hydrogel film is described. PFS chains are incorporated in the PNIPAM hydrogel layer, and employed as a reducing agent for the in-situ formation of AuNPs by using the redox properties provided by the PFS segments. The bilayer is made by a stepwise process in which the rigid top layer is crosslinked with UV irradiation first, followed by crosslinking of the PAAm hydrogel layer.

Wrinkles form on the bilayer surfaces as the top layer swells up in water, which makes the compressive strain exceed a theoretically established critical value. Semi-

infinite bilayers show the formation of random wrinkle patterns on the surface due to the isotropic stress distribution. Narrow bilayer hydrogels with defined dimensions show uniaxially aligned wrinkles parallel to the edge because the stress relaxation takes place in the edge and stress is uniaxially accumulated in the perpendicular direction. Wrinkles disappear with light irradiation or by placing the bilayer in hot water, which shrinks the PNIPAM hydrogel and thus reduces the swelling strain. The random and aligned wrinkle patterns are used as tunable isotropic and anisotropic light diffusors.

In **Chapter 4**, a series of bilayer hydrogels with different surface patterns showing various dynamic pattern evolutions are described. The ingredients of the top layer and bottom layer are the same as for the bilayer described in **Chapter 3** but different degrees of crosslinking were employed. Owing to the different compressive/swelling strain of the top layer and variations in the top layer-substrate modulus ratio, wrinkles (herringbone, stripes, labyrinth), creases and folds are formed on the surfaces when the top layer swells. In order to investigate the dynamic evolution of the patterns, the compressive strain was controlled by swelling the bottom layers for different periods of time, which decompresses the top layer gradually with time increasing. The transition of stripe patterns to weave-like patterns, the change of jog angle in herringbone patterns, transitions of Y shape folds to I shape folds to flat surfaces are observed and explained by the change of the stress state in the bilayers.

In **Chapter 5,** an anisotropic AuNP/PNIPAM/PVA nanocomposite hydrogel was synthesized. Different from previous chapters, the AuNPs were formed with PVA as a reducer and stabilizer in hot water. A semi-interpenetrating polymer network (semi-IPN) hydrogel of an AuNP/PVA/PNIPAM nanocomposite was first prepared, then further physically crosslinked into a full-IPN by cyclic freeze drying of pre-stretched hydrogel followed by annealing treatments. This AuNP/hydrogel nanocomposite displays a fast and reversible anisotropic change in size with temperature or light stimuli, enabling it to be used as actuator in future applications.

In **Chapter 6,** we study the phenomenon described in **Chapter 3** and **4**, where extra-stoichiometric amounts of AuNPs are formed in the reduction process of $HAuCl_4$ to AuNPs in PFS hydrogels. In order to gain more insight into the source of the extra electrons, PFS/PNIPAM hydrogels are fully oxidized first and then are allowed to react with $HAuCl_4$. We find that the redox state of PFS barely has any impact on the amount of AuNPs formed. Combined with a change in pH, we propose

a hypothesis that water reduced the uncomplexed Au^{3+} moieties, catalyzed by Fc or Fc^{+}.

As an outlook, in **Chapter 7**, a disulfide-functionalized PFS with a well-controlled composition is presented. Based on the Au-thiolate interaction, thiolated PFS chains were used as inks for printing on microelectrode arrays, synthesizing and assembling gold nanoparticles simultaneously and fabricating self-healing nanocomposite hydrogels.

Samenvatting

Dit proefschrift beschrijft het ontwerp, de synthese en toepassingen van een serie van met goud nanodeeltjes beladen, op stimuli reagerende hydrogel nanocomposieten. Poly(ferrocenylsilanen), PFSs, vormen een fascinerende klasse van redox-actieve organometaalpolymeren met een hoofdketen bestaand uit alternerende redox-actieve ferroceen en organosilaan eenheden. Op PFS gebaseerde, redox-responsieve hydrogels worden gebruikt als "gieterij" voor de in-situ vorming van goud nanodeeltjes (AuNPs) in dit proefschrift. Door gebruik te maken van een combinatie van een thermo-responsieve PNIPAM hydrogel en het fotothermische effect van de AuNPs, konden de vervorming en veranderingen in oppervlaktemorfologie van de hydrogel composieten worden beïnvloed door zowel temperatuur als door beschijnen met licht. Door het ontwerpen van verschillende anisotrope hydrogelstructuren konden een aantal toepassingen, waaronder rimpelende dubbellagen en actuatoren worden onderzocht in dit proefschrift. Op het gebied van de stoichiometrie van de vorming van goud nanodeeltjes onderzochten we het elektrochemische redoxproces tijdens het ontstaan van deze deeltjes en stellen we een model voor dat de bron van elektronen, naast ferroceen, verklaart.

In **Hoofdstuk 1** wordt een algemene inleiding van de onderwerpen relevant voor dit proefschrift gepresenteerd.

In **Hoofdstuk 2** wordt een literatuuroverzicht over AuNPs, op stimuli reagerende hydrogels, nanocomposiet hydrogels en anisotrope hydrogels gegeven. Het nut van op stimuli reagerende hydrogels voor de synthese van AuNPs wordt met name bediscussieerd. Ontwerp en toepassingen van nanocomposiet hydrogels, in het bijzonder van AuNP/hydrogel nanocomposieten, worden geïntroduceerd.

In **Hoofdstuk 3** wordt een hydrogel dubbellaag, bestaand uit een flexibele poly(acrylamide) (PAAm) onderlaag en een rigide AuNP nanocomposiet poly(*N*-isopropylacrylamide) (PNIPAM) PNIPAM/PFS toplaag beschreven. PFS ketens worden ondergebracht in de PNIPAM hydrogel toplaag en gebruikt als reducerende component voor de in-situ vorming van AuNPs, door gebruik te maken van de redox eigenschappen van de PFS segmenten. De dubbellaag wordt gefabriceerd door

middel van een stapsgewijs proces waarin de toplaag eerst wordt gecrosslinkt door UV straling, gevolgd door crosslinken van de PAAm hydrogel laag.

Rimpels vormen zich op het oppervlak van de dubbellagen wanneer de toplaag zwelt door het opnemen van water, waardoor de compressive strain een theoretisch bepaalde kritische waarde overschrijdt. Semi-oneindige dubbellagen vertonen niet-georiënteerde rimpelpatronen aan hun oppervlak vanwege de isotrope verdeling van spanningen. Rechthoekige dubbellagen met een gedefinieerde korte en lange zijde ontwikkelen uniaxiaal uitgelijnde rimpels parallel aan de korte zijde omdat spanningsrelaxatie plaatsvindt aan de randen en de spanning zich uniaxiaal ophoopt in de loodrechte richting. Rimpels verdwijnen onder invloed van bestralen met licht, of door het plaatsen van de dubbellaag in warm water, wat de PNIPAM hydrogel doet krimpen en daarmee de door zwelling ontstane spanning vermindert. De random en de uitgelijnde rimpelpatronen worden gebruikt als instelbare isotrope en anisotrope lichtverstrooiers.

Hoofdstuk 4 beschrijft een serie dubbellaag hydrogels met verschillende oppervlaktepatronen die diverse patroonveranderingen kunnen ondergaan. De ingrediënten van de toplaag en de onderlaag zijn hetzelfde als voor de dubbellaag beschreven in **Hoofdstuk 3**. In **Hoofdstuk 4** werd echter voor zowel de toplaag als de onderlaag een serie van verschillende crosslinkdichtheden gebruikt. Door de verschillende compressive/swelling strain van de toplaag en variaties in de toplaag-onderlaag modulus verhouding worden rimpels (visgraat, strepen, labyrinth), vouwen en plooien op de oppervlakken gevormd wanneer de toplaag zwelt. Om de dynamische evolutie van de patronen te onderzoeken werd de compressive strain beïnvloed door de onderlagen gedurende een verschillende tijd te laten zwellen, waardoor de toplaag met toenemende tijd geleidelijk meer decompressie onderging. De overgang van streeppatronen naar weef-achtige patronen, de verandering van de hoek in de zig-zag lijnen van visgraat patronen, en overgangen van Y-vormige vouwen naar I-vormige vouwen naar vlakke oppervlakken werden waargenomen en verklaard door de verandering van de spanningstoestand in de dubbellagen.

In **Hoofdstuk 5** werd een anisotrope AuNP/PNIPAM/PVA nanocomposiet hydrogel gesynthetiseerd. Anders dan in eerdere hoofdstukken werden de AuNPs in warm water gevormd met PVA als reducerend agens en stabilisator. Een semi-interpenetrerend netwerk (semi-IPN) hydrogel van een AuNP/PNIPAM/PVA nanocomposiet werd eerst gemaakt en daarna verder fysisch gecrosslinkt tot een volledige IPN door cyclisch vriesdrogen van voorverstrekte hydrogel, gevolgd door

annealingsstappen. Dit AuNP/hydrogel nanocomposiet vertoont een snelle en reversibele anisotrope verandering in grootte onder invloed van temperatuur- en lichtstimuli, wat toepassing als actuator in de toekomst mogelijk maakt.

In **Hoofdstuk 6** bestuderen we het verschijnsel beschreven in **Hoofdstuk 3** en **4**, waar boven-stoichiometrische hoeveelheden AuNPs worden gevormd in het reductieproces van $HAuCl_4$ naar AuNPs in PFS hydrogels. Om meer inzicht te krijgen in de oorsprong van de extra elektronen, werden PFS/PNIPAM hydrogels eerst volledig geoxideerd en pas daarna in contact gebracht met $HAuCl_4$. Het bleek dat de redoxtoestand van PFS nauwelijks invloed had op de hoeveelheid AuNPs die werd gevormd. In combinatie met een verandering in pH stellen we een hypothese voor waarin water ongecomplexeerde Au^{3+} ionen reduceert, gekatalyseerd door Fc of Fc^+.

Als vooruitblik wordt in **Hoofdstuk 7** een disulfide-gefunctionaliseerd PFS met een specifieke samenstelling gepresenteerd. Op basis van de Au-thiolaat interactie werden disulfide-gefunctionaliseerde PFS ketens gebruikt als inkt voor printen op microelektrode arrays, voor de synthese en gelijktijdige vorming van goed-gedefinieerde clusters van goud nanodeeltjes en voor de fabricage van zelf-herstellende nanocomposiet hydrogels.

Acknowledgements

"Time flies like an arrow; fruit flies like a banana." I still remember the first day I landed in the Netherlands, full of anxiety and curiosity. Now four and a half years has passed, I'm so grateful of this precious journey. On the road towards a doctoral degree, I had so many great experiences and met so many nice and motivating people. The research work presented in this Thesis cannot be achieved without the help of you guys, to whom I would like to show my gratitude.

My deepest gratitude goes first and foremost to Professor Julius Vancso, my promoter, who led me into the world of responsive materials. Thank you for giving me the opportunity to work in your group. You are such an enthusiastic scientist, encouraging mentor and enlightening teacher. In the past four and a half years, I learned from you in every meeting. Thank you for your kindness, continuous support, encouragement, and guidance throughout my PhD study. Thank you for teaching me how to give a proper presentation, how to look at my work from a critical point of view, how to articulate things in better ways and on and on. Thank you for guiding me on the right path.

I would like to express my heartfelt gratitude to my daily supervisor, Dr. Mark Hempenius. You are always there for me when I need help. No matter it's experimental works or paper works. I see you I know how a good chemist is like. I am so lucky that I got the chance to work with you. Thank you for your patient support, constant encouragement and guidance when I am lost and discouraged. Without your mentorship and guidance, I could not have reached this point.

Grateful acknowledgements to my defense committee members, Prof. Wolfgang Knoll, Prof. Xiaofeng Sui, Prof. Emile van der Heide, and Prof. Jeroen Cornelissen. Thank you for taking the time to read my thesis and the constructive suggestions.

Clemens and Ramon, thank you for the kind help with chemical orders, lab equipment and so many kinds of documents. Frans, thank you so much for lending me all the light facilities. And Marion, thank you for your help with all type of paperwork and documents.

I would like to thank my Chinese senior Lantian. Thank you so much for helping me with all the light equipment. You are such a nice and warm person. I wish you all the best with your career in UT.

My special thank goes to Yan, Sida and Minmin. Thank you for sharing your valuable experience with me and helping with all the trifles in my work and life. I wish you all the best in your family and career.

Lidia, thank you for being my motivating workout buddy. You are almost the most self-disciplined person I have ever known. Wish you all the best in your study! Ramona thank you for being my great neighbour. Adam, thank you for always being a caring friend for so many years. I wish you always stay positive and happy. You can do more than you think. Don't be limited by self-created boundaries.

I would also like to say thank you to Marco, Tibor, Roland and Giorgos. Tibor, it was a great pleasure for me to work with you during your project. I am very thankful for your contributions to my Thesis. Roland, it is always fun to talk with you. Thank you for the relaxing chats in between work. Giorgos, hope your Chinese can be good enough to swear one day haha. Thank you for being cheerful all time. Hope to see you in China someday. I am thankful to all the past MTP and present SPC members during my stay. Thank you for the joyful time we spent together.

I am extremely thankful to all my Chinese friends. Weiqiu, Peipei, Minsi, Hao, Ruosha, Juan, Quanliang, Zhen, Zhiguo, Jie and Ye. It is a great honor for me to meet you guys, to be your friends and to share so many beautiful memories together. Thank you all. Lijie, Huan and Yunchong, thank you for all the help in work, life and all the valuable time we spent together. Lijie, I hope you can enjoy your PhD life and take it easy. Always remember you can do it! Yanfeng, we have known each other for almost 7 years now. I am so grateful that our friendship starts in China, goes on in Europe and will go on and on in the coming years. I wish you all the best in the rest of your PhD life. Chao, all the time we had here is a blast. I am so happy I got to know you. I still remember the moment that we were sitting on the curb imagining our future in five and ten years. You are such a supporting friend and for sure someday we will travel together. Mada (Min), my all-time friend, we have always been accompanying each other through all good and bad times. We had so many tears and joys together. We witnessed each other’s important moments, and I don’t know how my PhD life would be like without you. I am sure wherever we end up in the future, we will be friends for life.

Most importantly, I would like to express my deepest gratitude to my family for offering me unconditional support and trust through all these years. 爸爸郝连志，妈妈李淑霞，大哥郝金龙，大嫂张彦青，谢谢你们这么多年来对我的理解和支持，支持我见识更广阔的世界，支持我遵从自己的内心。还有大侄女郝若兰，你要健康快乐长大呀！ Lars Stegeman, thank you for always being there for me through my ups and downs. You are my haven of rest when I am tired and sad. Thank you for giving me endless support and love. I can't wait to start the next chapter of life with you.

Finally, thank "you" for reading my thesis and wish you have a great day!

郝金梦

Jinmeng Hao

Enschede, 2022

Publications

1. **Hao, J.**, Chang, L., Hempenius, M.A., Vancso, G. J.. Multi-responsive wrinkling surfaces with in-situ synthesized plasmonic nanoparticles. *Submitted*
2. Halmagyi, T.†, **Hao, J.**†, Hempenius, M.A., Vancso, G. J.. Metal nanoparticles by direct reduction of electrolytes with redox-responsive poly(ferrocenylsilane)s: where do the electrons come from? *Submitted*
3. **Hao, J.**, Hempenius, M.A., Vancso, G. J.. Dynamic evolution of surface patterns on light-responsive bilayer hydrogels. *To be submitted*
4. Liu, Y. †, **Hao, J.** †, Hempenius, M.A., Zhang, K., Vancso, G. J.. Redox responsive hydrogel actuator and electrospun fibers: towards artificial muscles. *To be submitted*
5. Cirelli, M., **Hao, J**., Bor, T. C., Duvigneau, J., Benson, N., Akkerman, R., Vancso, G. J. (2019). Printing “smart” inks of redox-responsive organometallic polymers on microelectrode arrays for molecular sensing. ACS Applied Materials & Interfaces, 11(40), 37060-37068.
6. **Hao, J**., Wei, Y., Li, X., Mu, J. (2018). Poly (arylene ether ketone) s with low dielectric constants derived from polyhedral oligomeric silsesquioxane and difluorinated aromatic ketones. Journal of Applied Polymer Science, 135(15), 46084.
7. **Hao, J.**, Wei, Y., Chen, B., Mu, J. (2017). Polymerization of polyhedral oligomeric silsequioxane (POSS) with perfluoro-monomers and a kinetic study. RSC Advances, 7(18), 10700-10706.
8. **Hao, J**., Wei, Y., Mu, J. (2016). Ultra-low dielectric constant materials with hydrophobic property derived from polyhedral oligomeric silsequioxane (POSS) and perfluoro-aromatics. RSC Advances, 6(90), 87433-87439.
9. Jiang, Q., Zhang, W., **Hao, J.**, Wei, Y., Mu, J., Jiang, Z. (2015). A unique “cage-cage” shaped hydrophobic fluoropolymer film derived from a novel double-decker structural POSS with a low dielectric constant. Journal of Materials Chemistry C, 3(44), 11729-11734.